Wave Propagation through Photonic Crystal Slabs: Imaging and Localization

---

Chuanjian Shen

2006

To my beloved wife and children.

MSC PhD thesis series 2006-08
ISSN 1570-1530

The work described in this thesis was performed within the framework of the research programme "Waves in complex media" from the "Stichting voor Fundamenteel Onderzoek der Materie (FOM)", which is financially supported by the "Nederlandse Organisatie voor Wetenschappelijk Onderzoek (NWO)".

ISBN electronic version: 90-367-2563-1
ISBN printed version: 90-367-2562-3

RIJKSUNIVERSITEIT GRONINGEN

Wave Propagation through Photonic Crystal Slabs: Imaging and Localization

Proefschrift

ter verkrijging van het doctoraat in de
Wiskunde en Natuurwetenschappen
aan de Rijksuniversiteit Groningen
op gezag van de
Rector Magnificus, dr. F. Zwarts,
in het openbaar te verdedigen op
vrijdag 19 mei 2006
om 16:15 uur

door

Chuanjian Shen

geboren op 16 februari 1975
te Shenxian, China

Promotor:	Prof. dr. H. A. De Raedt
Copromotor:	Dr. K. F. L. Michielsen
Beoordelingscommissie:	Prof. dr. J. Th. M. De Hosson Prof. dr. D. G. Stavenga Prof. dr. W. L. Vos

Contents

Chapter 1

Introduction

With the formulation of Maxwell's partial differential equations about one and a half century ago [1], the electromagnetic wave phenomena became one of the most active research subjects in physics, both theoretically and experimentally. An enormous amount of applications based on electromagnetic field theory are proposed and realized, ranging from small household instruments to large military radar systems. However, the situations for which analytical solutions of the Maxwell equations can be obtained, are rare. With the advance of computer technology and numerical methods, complex electromagnetic systems can be modeled and simulated to investigate the behavior of the electromagnetic waves.

One of the complex electromagnetic systems of interest to us is a photonic crystal, a periodic dielectric structure with lattice spacings of the order of the wavelength of the electromagnetic wave [2]. Typical for a photonic crystal is that electromagnetic waves in a certain frequency range and/or with a certain polarization cannot propagate along certain directions in the crystal. This forbidden frequency range is called a stopgap. If the propagation of the electromagnetic wave is forbidden for any crystalline direction and any polarization, for a certain frequency range, then this forbidden frequency range is called a photonic band gap [2].

Photonic crystals show many intriguing optical phenomena such as negative refraction, superprism, ultrarefractive phenomena, focusing of light and the localization of light [3–6]. This makes that electromagnetic wave propagation in photonic crystals is not always easy to understand. However, the idea of controlling light by means of photonic crystals has led to many proposals for novel devices [2, 7–12] and has motivated many researchers to investigate a plethora of ideas. In this thesis we study various aspects of the electromagnetic wave propagation in two-dimensional photonic crystals by means of numerical solution of the time-dependent Maxwell equations.

In the framework of the collaboration of our research group with the research group Complex Photonic Systems (COPS), guided by Ad Lagendijk and Willem Vos, within the FOM research programme "Waves in complex media", we were asked to contribute, by means of finite-difference time domain (FDTD) simulations, to the understanding of the near-field patterns observed in experiments on near-field optics of three-dimensional crystals with metallic tips.

Flück and co-workers studied the transfer of light, coming from a metal tip, through a three-dimensional artificial opal of polystyrene spheres (arranged in a FCC lattice), by using a near-field scanning optical microscope (NSOM) [13, 14]. The three-dimensional photonic crystal is oriented such that it presents its <111> surface to the point-like light source.

For frequencies in the second order Γ-L stopgap region and below it, the observed near-field patterns reveal that more light is detected when the light source is positioned on top of a sphere compared to when the light source is positioned in between the spheres [13, 14]. For frequencies below the second order Γ-L stopgap region, the bright spots in the near-field pattern are positioned at the centers of the spheres [13, 14]. For higher frequencies a shift of the high intensity spots from the center of a sphere to an edge of the sphere is observed with increasing frequency [13, 14]. Moreover, the size of the bright intensity spots becomes smaller for higher frequencies [13, 14].

For frequencies around the first order Γ-L stopgap, a completely different optical field distribution is seen in the near-field images [14]. More light is transmitted through the crystal when the light source is positioned between the spheres, resulting in inversed near-field images compared to the ones for frequencies around the second order Γ-L stopgap region.

Tentative explanations for these phenomena were given based on reasoning from dynamical diffraction theory for X-rays [13, 14], but the explanations were not completely satisfying [14]. Since the theoretical understanding of the near-field coupling of light into three-dimensional photonic crystals was still in its infancy, the hope was that we could shed some extra light on this problem by means of numerical simulations.

Because of computational limitations, we decided to model the experiment in two dimensions. If indeed the (stop)gaps in the photonic bandstructure diagram were responsible for the observed frequency-dependent behavior, then we could expect to observe similar effects for a slab of a two-dimensional photonic crystal. Moreover, a similar frequency dependence of transmission NSOM images of a single layer of latex spheres was reported in [15]. In the latter work the relation between the NSOM contrast patterns and the photonic bands was discussed. We modeled the photonic crystal by a three-dimensional structure with translational invariance with respect to the z-direction. In this particular case the photonic crystal consists of several layers of pillars of dielectric material arranged in a triangular lattice configuration. The light source, that is the metal tip of the NSOM, is modeled as a point source.

Although we could obtain near-field optical patterns that were varying with the frequency and position of the point source, no systematic behavior could be detected that could explain all experimental observations. In order to understand what was going on in the experiment, and in order to be sure that our computer program, which was written from scratch, was working correctly (although we already had done many tests), we decided that we first needed a better understanding of wave propagation in photonic crystals in general. Therefore we started investigating the light propagation in two-dimensional photonic crystals in a more general context. During this journey, we made various interesting observations, from the point of view of physics as well as of numerical methods. In this thesis we give a summary of this work. Maybe with the knowledge we have now about the light propagation in two-dimensional photonic crystals, an explanation of the experimental NSOM observations is within reach.

1.1 Outline

In Chapter 2, we briefly explain the fundamental concepts and the construction of an unconditionally stable numerical method to solve the time-dependent Maxwell equations numerically, an alternative to the popular Yee algorithm that is only stable under a certain condition. We first discuss the symmetry properties of the time-dependent Maxwell equations. Then we describe the spatial discretization procedure using the Yee lattice in two-dimensional. We explain the product-formula approach to perform the time integration and discuss its stability. At the end of this chapter, we describe how we can use the method to calculate the density of states and the local (radiative) density of states.

In Chapter 3 we study the propagation of electromagnetic waves in conventional dielectric materials, in homogeneous isotropic negative index materials as well as in photonic crystals. Closely following [16], we first explain for conventional dielectric materials the concepts of phase and group velocity, phase and group refractive index, the Poynting vector and the phenomenon of reflection and refraction at an interface. We then generalize these concepts for homogeneous isotropic dielectric media with simultaneously negative permeability and permittivity, also known as negative index materials. We describe the phenomenon of negative refraction of a plane wave incident onto an interface between a conventional dielectric medium and a negative index material. We also give a short historical overview of the theoretical studies performed on negative index materials and how they can be fabricated. One of the approaches to obtain the phenomenon of negative refraction due to a negative effective refractive index is to use photonic crystals. photonic crystals are not homogeneous, but they are made of periodically modulated dielectric materials. These periodic dielectric structures have lattice parameters on the order of the wavelength of the electromagnetic wave. In a photonic crystal the permittivity is always locally positive and the permeability is equal to

one.

The electromagnetic wave that propagates in the photonic crystal is a superposition of plane waves, called Bloch waves, governed by the dispersion diagram that relates the frequency and the wave vector for each electromagnetic mode. Closely following [3, 17, 18] we demonstrate that for certain frequencies two-dimensional photonic crystals can behave as if they have a negative refractive index which is not limited by the refractive index of the constituents but is determined by the photonic band structure. In some cases this effective refractive index can be negative. We describe how to use the wave vector diagram analysis method to investigate the propagation of electromagnetic waves in dielectric materials. At the end of the chapter we discuss the relevance of considering these pure two-dimensional photonic crystals in relation to experiments.

In Chapter 4, we perform a systematic investigation of negative refraction in triangular lattice photonic crystals. We study both photonic crystal structures made from dielectric cylindrical pillars organized in a triangular lattice and photonic crystal structures made from a dielectric material with circular holes drilled in a triangular lattice configuration. We demonstrate that for both photonic crystal structures negative refraction can be observed and that the negative angles of refraction obtained from the FDTD simulations are in good agreement with the angles predicted by the wave vector diagram analysis method.

For the photonic crystal structures made from a dielectric material with circular holes drilled in a triangular lattice configuration, frequencies can be found for which the effective refractive index is approximately -1. For those frequencies we perform an elaborate study of the imaging properties of a photonic crystal slab made of this material. We investigate the effects of the surface terminations of the photonic crystal slab, the source/slab distance, the slab thickness and the mirror symmetry of the slab on the image position and image quality. We also consider the position of the internal focus. We demonstrate that for some frequencies the photonic crystal slab behaves in many respects as a slab made from a homogeneous medium with an effective refractive index of approximately -1 and thus operates as a negative-index lens. As an application of the photonic crystal lens we study the image formation of two point sources placed in front of the lens and the image transfer by a cascaded stack consisting of two and three triangular-lattice photonic crystal slabs separated by a layer of air.

In Chapter 5 we investigate the imaging properties of square lattice photonic crystals. We demonstrate that neither photonic crystal slabs made from dielectric cylindrical pillars organized on a square lattice, nor photonic crystal slabs made from a dielectric material with circular holes drilled in a square lattice configuration, behave as a negative-index lens.

In Chapter 6, we present a simple and efficient procedure to compute the spontaneous emission rate from short-time FDTD simulation data of the electromagnetic field energy. As an illustration, we apply this procedure to two-dimensional photonic crystals. For comparison, we calculate the local radiative density of states employing an unconditionally stable

FDTD method, that is without solving the eigenvalue problem and integrating over the (first) Brillouin zone. We demonstrate that both methods yield the same predictions about the enhancement or suppression of the spontaneous emission rate by photonic crystals.

1.2 Conventions and terminology

As discussed before, in this thesis we only consider dielectric structures having translational invariance with respect to one direction, the z-direction. In this case the plane of incidence that is the plane defined by the wave vector of the incident electromagnetic wave and the normal to the dielectric structure, is the xy-plane. In our numerical work, the dielectric structures have a finite width in the x-direction and they cover the whole width of the simulation area in the y-direction. The normal to the dielectric structure lies along the x-axis and incident electromagnetic waves move along the x-direction. This is the convention adopted in most simulation work on photonic crystals. In our analytic work in Chapter 3 however, we rotate the dielectric structures by 90 degrees, since this is the convention adopted in [16]. Hence, the normal to the dielectric structure lies along the y-axis and the incident waves move from bottom to top.

The plane of incidence allows making a distinction between two electromagnetic modes, the transverse magnetic (TM) mode and the transverse electric (TE) mode. We adopt the convention that for the TM mode the electric field vector is perpendicular to the plane of incidence, while for the TE mode the magnetic field vector is perpendicular to the plane of incidence. We use this electromagnetic mode convention since it is also used in the book of Born and Wolf [16], one of the classic books on optics, and in the vast majority of the literature concerning photonic crystals.

Only considering dielectric structures having translational invariance with respect to the z-direction effectively reduces the numerical problem of solving the time-dependent Maxwell equations to study light propagation in these structures, to a two-dimensional problem. In this case, the time-dependent Maxwell equations can be solved for the TM and TE mode separately. In order to study the propagation of light in these dielectric structures we make use of so-called point and line sources emitting TM or TE waves. Note that the names point and line source refer to the two-dimensional character of the numerical problem and correspond in fact in three-dimensional space to a line and plane source, respectively. We always use the names point and line source in what follows. In the case of a point source the points $\mathbf{r} = (x_0, y_0, z)$, where (x_0, y_0) are the coordinates of a point in the plane of incidence, are emitting the TM or TE wave. In the case of a line source the points in a plane defined by two points $\mathbf{r}_1 = (x_1, y_1, 0)$ and $\mathbf{r}_2 = (x_2, y_2, 0)$ in the plane of incidence and the z-axis are emitting the TM or TE wave.

In general, the incident wave makes an angle with the normal to the dielectric structure. We adopt the convention that angles α between two line segments are measured in a counter-clockwise or positive direction and that $0 \leq \alpha \leq \pi/2$.

Chapter 2

Finite-difference time domain method

The Maxwell's equations can be solved numerically either in the time domain or in the frequency domain. Each method has its strong points and its disadvantages. The frequency domain method, which assumes that the time-dependence is harmonic, plays an important role in calculating the eigenstates and band structures of regular structures such as photonic crystals. On the other hand, the time domain method, which solves the time-dependent Maxwell equations directly on spatial grids, is well-suited for computing problems that involve the evolution of electromagnetic fields and for systems containing complex materials.

In 1966, Yee proposed a method to solve the time-dependent Maxwell equations using the finite-difference time domain (FDTD) technique [19]. In the FDTD technique the time-dependent Maxwell equations are solved by propagating the electromagnetic fields in the time domain and by modelling the interaction of the electromagnetic fields with the medium. Since its introduction, the original algorithm has been refined and optimized for specific problems, but the concept has essentially stayed the same. Yee's algorithm solves for *both* the electric and magnetic fields in time and space using the coupled Maxwell's curl equations, rather than solving for the electric or magnetic field alone using the wave equation. In Yee's algorithm the electric $\mathbf{E}$ and magnetic $\mathbf{H}$ field components in three-dimensional space are placed so that each $\mathbf{E}$ component is surrounded by four circulating $\mathbf{H}$ components and every $\mathbf{H}$ component is surrounded by four circulating $\mathbf{E}$ components (see Fig. 2.1). In this way the electromagnetic fields are sampled in a highly efficient manner. The coordinates of the fields are labeled according to $(i, j, k) = (i\Delta x, j\Delta y, k\Delta z)$, where Δx, Δy and Δz are the mesh sizes for each dimension in this uniform, cubic lattice. By choosing this specific arrangement, the three-dimensional space lattice is effectively an interlinked array of Faraday's Law and

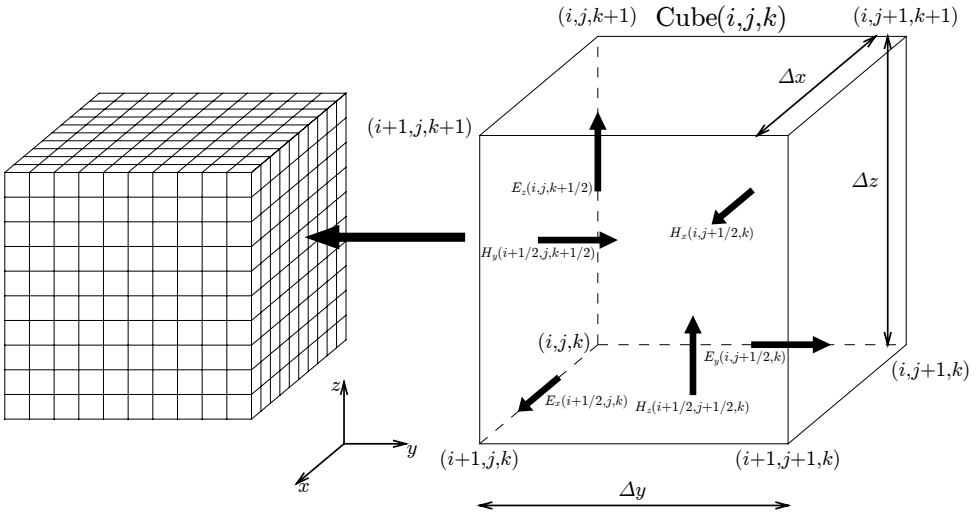

Figure 2.1: Position of the electric and magnetic field vector components in a Yee cell.

Ampere's Law contours [20] under the central-difference method.

Yee's algorithm is flexible, robust, fast, easy to implement and is widely accepted as a reliable computational tool in computational electromagnetism. Despite the great success of the Yee-based FDTD algorithms, one limitation of them is that their stability is conditional, depending on the mesh size of the spatial discretization and the time step of the time integration [20, 21]. For the basic Yee algorithms in three-dimensional, the Courant factor, defined as $S = c\Delta t/\left|\Delta \mathbf{r}\right|$, where $\left|\Delta \mathbf{r}\right| = \sqrt{(1/\Delta x)^2 + (1/\Delta y)^2 + (1/\Delta z)^2}$ and c denotes the velocity of light, must be smaller than one to guarantee the stability of the algorithm [20–22]. Therefore, a fine spatial mesh size $\Delta \mathbf{r}$ requires a fine time step Δt to maintain the desired accuracy. Such limitation prohibits application to a class of important fields such as bio-electromagnetics and VLSI design [23, 24], where the finest mesh size is necessary to resolve the spatial structure that is much smaller than the shortest wavelength of a significant spectral component occurring in the source. Another drawback of these methods is that they are not suitable to calculate spectra as they do not conserve the energy of the electromagnetic field. To overcome these limitations, a systematic approach to solve the time-dependent Maxwell equations with unconditionally stable numerical schemes was proposed and developed [25–28]. The basic idea of the methods is to employ a Lie-Trotter-Suzuki product-formula [29] to approximate the time evolution operator [30]. The time evolution operator is a matrix exponential of a skew-symmetric matrix and the approximations take the form of products of orthogonal transformations [25, 26]. The resulting numerical algorithms are unconditionally stable by construction [30].

In this chapter we briefly discuss the unconditionally stable FDTD technique that is used in the simulations of the following chapters.

2.1 Time-dependent Maxwell equations

The differential form of the time-dependent Maxwell equations in MKS (meter, kilo, second) units reads [16, 20]:

$$\frac{\partial}{\partial t}\mathbf{B}(t) = -\nabla \times \mathbf{E}(t) - \mathbf{M}(t), \tag{2.1a}$$

$$\frac{\partial}{\partial t}\mathbf{D}(t) = \nabla \times \mathbf{H}(t) - \mathbf{J}(t), \tag{2.1b}$$

$$\nabla \cdot \mathbf{D}(t) = \rho(t), \tag{2.1c}$$

$$\nabla \cdot \mathbf{B}(t) = 0, \tag{2.1d}$$

where

- $\mathbf{E}$: electric field (V m^{-1})
- $\mathbf{D}$: electric flux density (C m^{-2})
- $\mathbf{H}$: magnetic field (A m^{-1})
- $\mathbf{B}$: magnetic flux density (W m^{-2})
- $\mathbf{J}$: electric current density (A m^{-2})
- $\mathbf{M}$: magnetic current density (V m^{-2})
- ρ: free charge density (C m^{-3})

Note that $\mathbf{J}$ and $\mathbf{M}$ may contain sources $\mathbf{J}_{\text{source}}$ and $\mathbf{M}_{\text{source}}$, of $\mathbf{E}$-field and $\mathbf{H}$-field energy, respectively, as well as the electric and magnetic losses that attenuate $\mathbf{E}$-fields and $\mathbf{H}$-fields in isotropic and nondispersive materials [20]:

$$\mathbf{J} = \mathbf{J}_{\text{source}} + \sigma\mathbf{E} \quad , \quad \mathbf{M} = \mathbf{M}_{\text{source}} + \sigma^*\mathbf{H}, \tag{2.2}$$

where

- σ: electric conductivity (S m^{-1})
- σ^*: magnetic loss (Ω m^{-1})

The behavior of isotropic dielectric materials, that is insulating materials with physical properties that at each point are independent of the direction, under the influence of an electromagnetic field is described by the material equations [16]

$$\mathbf{D} = \varepsilon\mathbf{E} = \varepsilon_r\varepsilon_0\mathbf{E}, \tag{2.3a}$$

$$\mathbf{B} = \mu\mathbf{H} = \mu_r\mu_0\mathbf{H}, \tag{2.3b}$$

where

- ε: electrical permittivity (F m^{-1})
- ε_0: free-space permittivity ($= 8.854 \times 10^{-12}$ F m^{-1})
- ε_r: relative electrical permittivity (dimensionless), which is often called the dielectric constant, a characteristic quantity of a given dielectric substance.
- μ: magnetic permeability (H m^{-1})
- μ_0: free-space permeability ($= 4\pi \times 10^{-7}$ H m^{-1})
- μ_r: relative permeability (dimensionless)

Note that although only the time dependence is written explicitly, all the quantities described above additionally depend on space, for instance: $\mathbf{E}(t) = (E_x(\mathbf{r},t), E_y(\mathbf{r},t), E_z(\mathbf{r},t))^{\mathrm{T}}$and $\varepsilon = \varepsilon(\mathbf{r})$, where $\mathbf{r} = (x,y,z)^{\mathrm{T}}$ denotes the position vector of a point in space. For simplicity of notation we omit the spatial dependence unless this leads to ambiguities. In this thesis, we consider electromagnetic fields in linear, isotropic, nondispersive dielectric materials without electric charges only. Then the time-dependent Maxwell equations, Eq. (2.1), reduce to a set of first-order coupled differential equations:

$$\frac{\partial}{\partial t}\mathbf{H}(t) = \frac{1}{\mu}(-\nabla\times\mathbf{E}(t) - \sigma^*\mathbf{H}(t) - \mathbf{M}_{\mathrm{source}}(t)), \tag{2.4a}$$

$$\frac{\partial}{\partial t}\mathbf{E}(t) = \frac{1}{\varepsilon}(\nabla\times\mathbf{H}(t) - \sigma\mathbf{E}(t) - \mathbf{J}_{\mathrm{source}}(t)), \tag{2.4b}$$

$$\nabla\cdot\varepsilon\mathbf{E}(t) = 0, \tag{2.4c}$$

$$\nabla\cdot\mu\mathbf{H}(t) = 0. \tag{2.4d}$$

Some important physical symmetries of the Maxwell equations can be made explicit by introducing the fields

$$\mathbf{X}(t) \equiv \sqrt{\mu}\mathbf{H}(t) \quad \text{and} \quad \mathbf{Y}(t) \equiv \sqrt{\varepsilon}\mathbf{E}(t)\,. \tag{2.5}$$

In terms of the fields $\mathbf{X}(t)$ and $\mathbf{Y}(t)$ the time-dependent Maxwell equations (Eqs. (2.4a) and (2.4b)) read in matrix notation

$$\frac{\partial}{\partial t}\begin{pmatrix}\mathbf{X}(t)\\ \mathbf{Y}(t)\end{pmatrix} = \begin{pmatrix} -\frac{\sigma^*}{\sqrt{\mu}} & -\frac{1}{\sqrt{\mu}}\nabla\times\frac{1}{\sqrt{\varepsilon}} \\ \frac{1}{\sqrt{\varepsilon}}\nabla\times\frac{1}{\sqrt{\mu}} & -\frac{\sigma}{\sqrt{\varepsilon}}\end{pmatrix}\begin{pmatrix}\mathbf{X}(t)\\ \mathbf{Y}(t)\end{pmatrix} - \begin{pmatrix}\mathbf{M}_{\mathrm{source}}(t)/\sqrt{\mu}\\ \mathbf{J}_{\mathrm{source}}(t)/\sqrt{\varepsilon}\end{pmatrix}. \tag{2.6}$$

Writing $\Psi(t) = (\mathbf{X}(t),\ \mathbf{Y}(t))^{\mathrm{T}}$, Eq. (2.6) becomes

$$\frac{\partial}{\partial t}\Psi(t) = \mathcal{H}\Psi(t) - \mathcal{S}(t), \tag{2.7}$$

where $\mathcal{S}(t)$ represents the source term

$$\mathcal{S}(t) \equiv \begin{pmatrix}\mathbf{M}_{\mathrm{source}}(t)/\sqrt{\mu}\\ \mathbf{J}_{\mathrm{source}}(t)/\sqrt{\varepsilon}\end{pmatrix}, \tag{2.8}$$

and $\mathcal{H}$ denotes the operator

$$\mathcal{H} \equiv \begin{pmatrix} -\frac{\sigma^*}{\sqrt{\mu}} & -\frac{1}{\sqrt{\mu}}\nabla\times\frac{1}{\sqrt{\varepsilon}} \\ \frac{1}{\sqrt{\varepsilon}}\nabla\times\frac{1}{\sqrt{\mu}} & -\frac{\sigma}{\sqrt{\varepsilon}}\end{pmatrix}. \tag{2.9}$$

The operator $\mathcal{H}$ can be split into the diagonal part and the rest

$$\mathcal{H} = \mathcal{H}_{\mathrm{d}} + \mathcal{H}_{\mathrm{s}}, \tag{2.10}$$

where

$$\mathcal{H}_{\mathrm{d}} = \begin{pmatrix} -\frac{\sigma^*}{\sqrt{\mu}} & 0 \\ 0 & -\frac{\sigma}{\sqrt{\varepsilon}}\end{pmatrix}, \tag{2.11}$$

and

$$\mathcal{H}_{\mathrm{s}} = \begin{pmatrix} 0 & -\frac{1}{\sqrt{\mu}}\nabla\times\frac{1}{\sqrt{\varepsilon}} \\ \frac{1}{\sqrt{\varepsilon}}\nabla\times\frac{1}{\sqrt{\mu}} & 0\end{pmatrix}. \tag{2.12}$$

It is easy to show that $\mathcal{H}_{\mathrm{s}}$ is skew symmetric, i.e. $\mathcal{H}_{\mathrm{s}}^{\mathrm{T}} = -\mathcal{H}_{\mathrm{s}}$, with respect to the inner product $\langle\Psi(t)|\Psi'(t)\rangle \equiv \int_V \Psi^{\mathrm{T}}(t)\cdot\Psi'(t)\,d\mathbf{r}$, where V denotes the volume of the system. In addition to Eq. (2.6), the electromagnetic fields also satisfy $\nabla\cdot(\sqrt{\mu}\mathbf{X}(t)) = 0$ and $\nabla\cdot(\sqrt{\varepsilon}\mathbf{Y}(t)) = 0$ (see Eqs. (2.4c) and (2.4d)).

2.1.1 Note about units

Throughout this thesis, we use dimensionless quantities unless they are specified: We measure distances in units of the wavelength λ, frequencies in units of c/λ, time in units of λ/c,

ε in units of ε_0 and μ in units of μ_0.

2.2 Numerical method: lossless, source-free system

For simplicity and clarity, we first investigate the electromagnetic fields in a linear, isotropic, nondispersive, lossless material without electric and magnetic current sources. Then Eq. (2.7) becomes

$$\frac{\partial}{\partial t}\Psi(t) = \mathcal{H}_{\mathrm{s}}\Psi(t), \tag{2.13}$$

which is a first-order differential equation, with its formal solution given by

$$\Psi(t) = e^{t\mathcal{H}_{\mathrm{s}}}\Psi(0) \equiv \mathcal{U}(t)\Psi(0), \tag{2.14}$$

where $\Psi(0)$ is the initial state of the electromagnetic fields and the operator $\mathcal{U}$ determines their time evolution. Since $\mathcal{H}_{\mathrm{s}}$ is skew-symmetric the time operator $\mathcal{U}$ is an orthogonal transformation [22].

From the definition $\Psi(t) = \left(\sqrt{\mu(\mathbf{r})}\mathbf{H}(\mathbf{r},t), \sqrt{\varepsilon(\mathbf{r})}\mathbf{E}(\mathbf{r},t)\right)^{\mathrm{T}}$ it follows that

$$\|\Psi(t)\|^2 = \langle\Psi(t)|\Psi(t)\rangle = \int_V \left[\varepsilon(\mathbf{r})\mathbf{E}^2(\mathbf{r},t) + \mu(\mathbf{r})\mathbf{H}^2(\mathbf{r},t)\right] d\mathbf{r}, \tag{2.15}$$

relating the length (norm) of the vector $\Psi(t)$ to the energy density

$$w(\mathbf{r},t) = \varepsilon(\mathbf{r})\mathbf{E}^2(\mathbf{r},t) + \mu(\mathbf{r})\mathbf{H}^2(\mathbf{r},t), \tag{2.16}$$

of the electromagnetic fields. From Eq. (2.14) it follows that

$$\langle\Psi(t)|\Psi(t)\rangle = \langle\mathcal{U}(t)\Psi(0)|\mathcal{U}(t)\Psi(0)\rangle = \langle\Psi(0)|\Psi(0)\rangle\,,$$

where use has been made of the fact that $\mathcal{U}$ is an orthogonal transformation. In physical terms, this means that the energy density of the electromagnetic fields does not change with time.

2.2.1 Spatial discretization

The skew-symmetry of the operator $\mathcal{H}_{\mathrm{s}}$ is a very important physical property that expresses the conservation of electromagnetic-field energy. Numerical algorithms that solve the time-dependent Maxwell equations while preserving this symmetry are unconditionally stable [25, 26], meaning that the numerical solution is stable, independent of the time step that is used to integrate the time-dependent Maxwell equations. Thus, it is desirable to keep this

skew-symmetry intact while discretizing the differential operators that appear in the Maxwell equations. By adopting the Yee lattice [19] and the central-difference approximation for the spatial derivatives, the resulting time-evolution matrix H is skew-symmetric [22]. We limit our discussion to the two-dimensional model that is used in the remainder of this thesis (for one- and three-dimensional cases, see [22, 25] for details).

2.2.2 Spatial discretization in two-dimensional system

Assuming translational invariance with respect to the z-direction, Eq. (2.6) reduces to a problem in two spatial dimensions. There are then two sets of three differential equations, each set corresponding to one of two different polarizations. The electromagnetic fields for the so-called TM mode in two-dimensional are $\Psi_{\mathrm{TM}}(t) = (\mathbf{X}_x(t), \mathbf{Y}_y(t), \mathbf{Y}_z(t))^{\mathrm{T}}$, in terms of which the time-dependent Maxwell equations reads

$$\frac{\partial}{\partial t}\Psi_{\mathrm{TM}}(t) = \mathcal{H}_{\mathrm{TM}}\Psi_{\mathrm{TM}}(t) = \begin{pmatrix} 0 & 0 & -\frac{1}{\sqrt{\mu}}\frac{\partial}{\partial y}\frac{1}{\sqrt{\varepsilon}} \\ 0 & 0 & \frac{1}{\sqrt{\mu}}\frac{\partial}{\partial x}\frac{1}{\sqrt{\varepsilon}} \\ -\frac{1}{\sqrt{\varepsilon}}\frac{\partial}{\partial y}\frac{1}{\sqrt{\mu}} & \frac{1}{\sqrt{\varepsilon}}\frac{\partial}{\partial x}\frac{1}{\sqrt{\mu}} & 0 \end{pmatrix}\Psi_{\mathrm{TM}}(t). \tag{2.17}$$

Similarly, the TE mode fields are $\Psi_{\mathrm{TE}}(t) = (\mathbf{Y}_x(t),\, \mathbf{X}_y(t),\, \mathbf{X}_z(t))^{\mathrm{T}}$, for which we have the matrix equation

$$\frac{\partial}{\partial t}\Psi_{\mathrm{TE}}(t) = \mathcal{H}_{\mathrm{TE}}\Psi_{\mathrm{TE}}(t) = \begin{pmatrix} 0 & 0 & \frac{1}{\sqrt{\varepsilon}}\frac{\partial}{\partial y}\frac{1}{\sqrt{\mu}} \\ 0 & 0 & -\frac{1}{\sqrt{\varepsilon}}\frac{\partial}{\partial x}\frac{1}{\sqrt{\mu}} \\ \frac{1}{\sqrt{\mu}}\frac{\partial}{\partial y}\frac{1}{\sqrt{\varepsilon}} & -\frac{1}{\sqrt{\mu}}\frac{\partial}{\partial x}\frac{1}{\sqrt{\varepsilon}} & 0 \end{pmatrix}\Psi_{\mathrm{TE}}(t). \tag{2.18}$$

We can discretize the continuum space using the Yee-lattice as shown in Fig. 2.2. The electromagnetic fields for the TM mode are then defined as follows

$$\Psi_{\mathrm{TM}}(i,j,t) = \begin{cases} X_x(i,j,t) = \sqrt{\mu_{i,j}}H_x(i,j,t) & i \text{ even and } j \text{ odd} \\ X_y(i,j,t) = \sqrt{\mu_{i,j}}H_y(i,j,t) & i \text{ odd and } j \text{ even} \\ Y_z(i,j,t) = \sqrt{\varepsilon_{i,j}}E_z(i,j,t) & i \text{ even and } j \text{ even} \end{cases}. \tag{2.19}$$

Using the second order central-difference approximation for the spatial derivatives, Eq. (2.17)

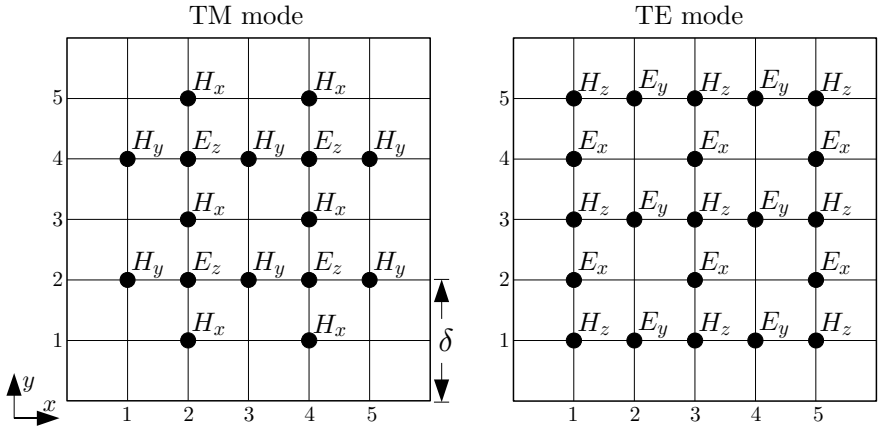

Figure 2.2: Positions of the TM and TE mode electromagnetic field components on the two-dimensional Yee grid for $N_x = 5$ and $N_y = 5$.

becomes

$$(H_{\mathrm{TM}}\Psi_{\mathrm{TM}}(t))(i+1,j) = \frac{\Psi_{\mathrm{TM}}(i+1,j-1,t)}{\delta\sqrt{\varepsilon_{i+1,j-1}\mu_{i+1,j}}} - \frac{\Psi_{\mathrm{TM}}(i+1,j+1,t)}{\delta\sqrt{\varepsilon_{i+1,j+1}\mu_{i+1,j}}}, \tag{2.20a}$$

$$(H_{\mathrm{TM}}\Psi_{\mathrm{TM}}(t))(i,j+1) = \frac{\Psi_{\mathrm{TM}}(i+1,j+1,t)}{\delta\sqrt{\varepsilon_{i+1,j+1}\mu_{i,j+1}}} - \frac{\Psi_{\mathrm{TM}}(i-1,j+1,t)}{\delta\sqrt{\varepsilon_{i-1,j+1}\mu_{i,j+1}}}, \tag{2.20b}$$

$$\begin{aligned}(H_{\mathrm{TM}}\Psi_{\mathrm{TM}}(t))(i+1,j+1) = &\frac{\Psi_{\mathrm{TM}}(i+1,j,t)}{\delta\sqrt{\varepsilon_{i+1,j+1}\mu_{i+1,j}}} - \frac{\Psi_{\mathrm{TM}}(i+1,j+2,t)}{\delta\sqrt{\varepsilon_{i+1,j+1}\mu_{i+1,j+2}}} \\ &+ \frac{\Psi_{\mathrm{TM}}(i+2,j+1,t)}{\delta\sqrt{\varepsilon_{i+1,j+1}\mu_{i+2,j+1}}} - \frac{\Psi_{\mathrm{TM}}(i,j+1,t)}{\delta\sqrt{\varepsilon_{i+1,j+1}\mu_{i,j+1}}},\end{aligned} \tag{2.20c}$$

for $i = 1, 3, \ldots, N_x$ and $j = 1, 3, \ldots, N_y$. As a result, the spatial discretized version of the Maxwell equations for the TM mode (Eq. (2.17)) can be written as

$$\frac{\partial}{\partial t}\Psi_{\mathrm{TM}}(t) = H_{\mathrm{TM}}\Psi_{\mathrm{TM}}(t) = \left[H_{\mathrm{TM}}^{(1)} + H_{\mathrm{TM}}^{(2)} + H_{\mathrm{TM}}^{(3)} + H_{\mathrm{TM}}^{(4)}\right]\Psi_{\mathrm{TM}}(t), \tag{2.21}$$

where

$$H_{\mathrm{TM}}^{(1)} = \sum_{i=1}^{N_x-2}{}' \sum_{j=1}^{N_y-2}{}' \frac{\mathbf{e}_{i,j+1}\mathbf{e}_{i+1,j+1}^{\mathrm{T}} - \mathbf{e}_{i+1,j+1}\mathbf{e}_{i,j+1}^{\mathrm{T}}}{\delta\sqrt{\varepsilon_{i+1,j+1}\mu_{i,j+1}}}, \tag{2.22a}$$

$$H_{\mathrm{TM}}^{(2)} = \sum_{i=1}^{N_x-2}{}' \sum_{j=1}^{N_y-2}{}' \frac{\mathbf{e}_{i+1,j+1}\mathbf{e}_{i+2,j+1}^{\mathrm{T}} - \mathbf{e}_{i+2,j+1}\mathbf{e}_{i+1,j+1}^{\mathrm{T}}}{\delta\sqrt{\varepsilon_{i+1,j+1}\mu_{i+2,j+1}}}, \tag{2.22b}$$

$$H_{\mathrm{TM}}^{(3)} = \sum_{i=1}^{N_x-2}{}' \sum_{j=1}^{N_y-2}{}' -\frac{\mathbf{e}_{i+1,j}\mathbf{e}_{i+1,j+1}^{\mathrm{T}} - \mathbf{e}_{i+1,j+1}\mathbf{e}_{i+1,j}^{\mathrm{T}}}{\delta\sqrt{\varepsilon_{i+1,j+1}\mu_{i+1,j}}}, \tag{2.22c}$$

$$H_{\mathrm{TM}}^{(4)} = \sum_{i=1}^{N_x-2}{}' \sum_{j=1}^{N_y-2}{}' -\frac{\mathbf{e}_{i+1,j+1}\mathbf{e}_{i+1,j+2}^{\mathrm{T}} - \mathbf{e}_{i+1,j+2}\mathbf{e}_{i+1,j+1}^{\mathrm{T}}}{\delta\sqrt{\varepsilon_{i+1,j+1}\mu_{i+1,j+2}}}. \tag{2.22d}$$

Here $\mathbf{e}_{i,j}$ denotes the i,j-th unit vector in the N_xN_y dimensional space and the prime indicates that the sum is over odd integers only. It is easy to see that $H_{\mathrm{TM}}^{(k)}, k = 1,2,3,4$ are skew-symmetric, so is H_{TM}.

We can do the same as above for the TE mode

$$\Psi_{\mathrm{TE}}(i,j,t) \quad = \quad \begin{cases} Y_x(i,j,t) = \sqrt{\varepsilon_{i,j}}E_x(i,j,t) & i \text{ odd and } j \text{ even} \\ Y_y(i,j,t) = \sqrt{\varepsilon_{i,j}}E_y(i,j,t) & i \text{ even and } j \text{ odd} \\ X_z(i,j,t) = \sqrt{\mu_{i,j}}H_z(i,j,t) & i \text{ odd and } j \text{ odd} \end{cases}. \tag{2.23}$$

The discretized version of the Maxwell equations for the TE mode (Eq. (2.18)) reads

$$\frac{\partial}{\partial t}\Psi_{\mathrm{TE}}(t) = H_{\mathrm{TE}}\Psi_{\mathrm{TE}}(t) = \left[H_{\mathrm{TE}}^{(1)} + H_{\mathrm{TE}}^{(2)} + H_{\mathrm{TE}}^{(3)} + H_{\mathrm{TE}}^{(4)}\right]\Psi_{\mathrm{TE}}(t), \tag{2.24}$$

where

$$H_{\mathrm{TE}}^{(1)} = \sum_{i=1}^{N_x-2}{}' \sum_{j=1}^{N_y-2}{}' -\frac{\mathbf{e}_{i,j}\mathbf{e}_{i+1,j}^{\mathrm{T}} - \mathbf{e}_{i+1,j}\mathbf{e}_{i,j}^{\mathrm{T}}}{\delta\sqrt{\varepsilon_{i+1,j}\mu_{i,j}}}, \tag{2.25a}$$

$$H_{\mathrm{TE}}^{(2)} = \sum_{i=1}^{N_x-2}{}' \sum_{j=1}^{N_y-2}{}' -\frac{\mathbf{e}_{i+1,j}\mathbf{e}_{i+2,j}^{\mathrm{T}} - \mathbf{e}_{i+2,j}\mathbf{e}_{i+1,j}^{\mathrm{T}}}{\delta\sqrt{\varepsilon_{i+1,j}\mu_{i+2,j}}}, \tag{2.25b}$$

$$H_{\mathrm{TE}}^{(3)} = \sum_{i=1}^{N_x-2}{}' \sum_{j=1}^{N_y-2}{}' \frac{\mathbf{e}_{i,j}\mathbf{e}_{i,j+1}^{\mathrm{T}} - \mathbf{e}_{i,j+1}\mathbf{e}_{i,j}^{\mathrm{T}}}{\delta\sqrt{\varepsilon_{i,j+1}\mu_{i,j}}}, \tag{2.25c}$$

$$H_{\mathrm{TE}}^{(4)} = \sum_{i=1}^{N_x-2}{}' \sum_{j=1}^{N_y-2}{}' \frac{\mathbf{e}_{i,j+1}\mathbf{e}_{i,j+2}^{\mathrm{T}} - \mathbf{e}_{i,j+2}\mathbf{e}_{i,j+1}^{\mathrm{T}}}{\delta\sqrt{\varepsilon_{i,j+1}\mu_{i,j+2}}}. \tag{2.25d}$$

Also in this case, $H_{\mathrm{TE}}^{(1)}, \ldots, H_{\mathrm{TE}}^{(4)}$ and H_{TE} are skew-symmetric matrices.

2.2.3 Time integration

After space discretization, the operator $\mathcal{H}_{\mathrm{s}}$ becomes a skew symmetric matrix H. Then the discretized version of Eq. (2.14) becomes

$$\Psi(t+\tau) = e^{\tau H}\Psi(t) = U(\tau)\Psi(t), \tag{2.26}$$

where $U(\tau)$ is formally defined by the matrix-valued Taylor series

$$U(\tau) = e^{\tau H} = \sum_{n=0}^{\infty} \frac{(\tau H)^n}{n!}. \tag{2.27}$$

The cases where $U(\tau)$ can be calculated explicitly are rare and of little relevance for realistic problems. Thus, the general strategy is to develop some approximation scheme to perform the operation Eq. (2.26). A systematic approach to construct orthogonal approximations to matrix exponentials in general is to make use of the Lie-Trotter-Suzuki formula [27–29, 31–34]

$$e^{tH} = e^{t(H_1+\cdots+H_p)} = \lim_{m\to\infty} (\prod_{i=1}^{p} e^{tH_i/m})^m. \tag{2.28}$$

The first-order approximation to $U(\tau)$ with small τ is

$$U_1(\tau) = e^{\tau H_1} e^{\tau H_2} \cdots e^{\tau H_p}. \tag{2.29}$$

If all the H_i are real and skew-symmetric, $U_1(\tau)$ is orthogonal and the numerical scheme based on Eq. (2.29) will be unconditional stable [27]. For orthogonal matrices $U(\tau)$ and $U_1(\tau)$ it can be shown that [30]

$$||U(\tau) - U_1(\tau)|| \leq \frac{\tau^2}{2} \sum_{i<j} |||[H_i, H_j]|||, \tag{2.30}$$

where $[H_i, H_j] = H_i H_j - H_j H_i$ is in general not zero. The product-formula approach provides simple, systematic procedures to improve the accuracy of the approximation to $U(\tau)$ without changing its fundamental symmetries [30, 32–34]. Among them the second order approximation

$$U_2(\tau) = U_1(-\tau/2)^{\mathrm{T}} U_1(\tau/2), \tag{2.31}$$

with $O(\tau^2)$ accuracy

$$||U(t = m\tau) - [U_2(\tau)]^m|| \leq c_2 \tau^2 t, \tag{2.32}$$

where c_2 is a positive constant and the 4-th order approximation

$$U_4(\tau) = U_2(a\tau)U_2(a\tau)U_2((1-4a)\tau)U_2(a\tau)U_2(a\tau), \tag{2.33}$$

with $O(\tau^4)$ accuracy

$$||U(t = m\tau) - [U_4(\tau)]^m|| \leq c_4\tau^4 t, \tag{2.34}$$

where c_4 is a positive constant and $a = 1/(4 - 4^{1/3})$ are particularly useful [27]. In practice, the crucial step of this approach is to split the matrix H into H_i's whose exponential can be calculated efficiently. Now we would like to show that the spatial discretized matrices $H_{\rm TM}^{(i)}$'s and $H_{\rm TM}^{(i)}$'s in Section 2.2.2 satisfy this criterion.

Starting from Eq. (2.22a), we can rewrite the matrix $H_{\rm TM}^{(1)}$ as

$$H_{\rm TM}^{(1)} = \sum_{i=1}^{N_x-2}{}' \sum_{j=1}^{N_y-2}{}' H_1(i,j), \tag{2.35}$$

where

$$H_1(i,j) = \frac{\mathbf{e}_{i,j+1}\mathbf{e}_{i+1,j+1}^{\rm T} - \mathbf{e}_{i+1,j+1}\mathbf{e}_{i,j+1}^{\rm T}}{\delta\sqrt{\varepsilon_{i+1,j+1}\mu_{i,j+1}}}. \tag{2.36}$$

An important property of the matrices $H_1(i,j)$ is that they commute. Here we give a simple proof. Using the fact that the vectors $\mathbf{e}_{i,j}$ are orthonormal, we find

$$\begin{aligned} H_1(i,j)H_1(i',j') = \beta(i,j)\beta(i',j') \big[&\delta_{i+1,i'}\delta_{j+1,j'+1}\mathbf{e}_{i,j+1}\mathbf{e}_{i'+1,j'+1}^{\rm T} \\ &- \delta_{i+1,i'+1}\delta_{j+1,j'+1}\mathbf{e}_{i,j+1}\mathbf{e}_{i',j'+1}^{\rm T} \\ &- \delta_{i,i'}\delta_{j+1,j'+1}\mathbf{e}_{i+1,j+1}\mathbf{e}_{i'+1,j'+1}^{\rm T} \\ &+ \delta_{i,i'+1}\delta_{j+1,j'+1}\mathbf{e}_{i+1,j+1}\mathbf{e}_{i',j'+1}^{\rm T}\big], \end{aligned} \tag{2.37}$$

where $\delta_{i,j}$ is the Kronecker delta function and

$$\beta(i,j) = \frac{1}{\delta\sqrt{\varepsilon_{i+1,j+1}\mu_{i,j+1}}}. \tag{2.38}$$

Noting that i, j, i', j' in Eq. (2.37) are all odd numbers, Eq. (2.37) becomes

$$H_1(i,j)H_1(i',j') = \begin{cases} -\beta^2(i,j)(\mathbf{e}_{i,j+1}\mathbf{e}_{i,j+1}^{\rm T} + \mathbf{e}_{i+1,j+1}\mathbf{e}_{i+1,j+1}^{\rm T}) & \text{for } i = i', j = j' \\ 0 & \text{for } i \neq i' \text{ or } j \neq j' \end{cases}, \tag{2.39}$$

from which it is clear that $H_1(i,j)$ and $H_1(i',j')$ commute, that is

$$H_1(i,j)H_1(i',j') = H_1(i',j')H_1(i,j). \tag{2.40}$$

The point of all this is that because of this property, the matrix exponential $e^{\tau H_{\mathrm{TM}}^{(1)}}$ decomposes into

$$e^{\tau H_{\mathrm{TM}}^{(1)}} = \prod_{i=1}^{N_x-2}{}' \prod_{i=1}^{N_y-2}{}' \exp\left(\tau\beta(i,j)(\mathbf{e}_{i,j+1}\mathbf{e}_{i+1,j+1}^{\mathrm{T}} - \mathbf{e}_{i+1,j+1}\mathbf{e}_{i,j+1}^{\mathrm{T}})\right). \tag{2.41}$$

The matrix exponential of the right hand side of Eq. (2.41) reduces to the calculation of $(N_x-1)(N_y-1)/4$ matrix exponentials of the kind

$$\exp\left[\beta\begin{pmatrix} 0 & 1 \\ -1 & 0 \end{pmatrix}\right] = \begin{pmatrix} \cos\beta & \sin\beta \\ -\sin\beta & \cos\beta \end{pmatrix}, \tag{2.42}$$

which can be computed easily. For $H_{\mathrm{TM}}^{(2)}, H_{\mathrm{TM}}^{(3)}, H_{\mathrm{TM}}^{(4)}$, the procedure is the same and therefore we can compute

$$U_1(\tau) = \exp(\tau H_{\mathrm{TM}}^{(1)})\exp(\tau H_{\mathrm{TM}}^{(2)})\exp(\tau H_{\mathrm{TM}}^{(3)})\exp(\tau H_{\mathrm{TM}}^{(4)}), \tag{2.43}$$

efficiently. Following Eqs. (2.31) and (2.33) it is not difficult to further compute $U_2(\tau)$ and $U_4(\tau)$. For the TE mode computation, the procedure is exactly the same.

2.3 Lossy system with sources

In the previous section, we explained in detail how to solve the time-dependent Maxwell equations in a lossless material without current sources. However, lossy materials are not only important if we think about applications, but they also play an important role in simulations. Even in a simulation of an idealized experiment in which we only consider lossless materials, we need to include artificial losses. An example is the introduction of absorbing boundaries to avoid the side effects of otherwise reflected waves. Current sources on the other hand can serve as a natural way to investigate the characteristics of the material in all kinds of experiments. It is not difficult to incorporate lossy materials and current sources into the numerical schemes we discussed above. Instead of solving Eq. (2.13) we have to go back to the more general case described by Eq. (2.7). The characteristics of the lossy material are represented in $\mathcal{H}_{\mathrm{d}}$ (see Eq. (2.11)) and the sources are represented in the source term $\mathcal{S}$ (see Eq. (2.12)). The spatial discretized matrix H_{d} for the operator $\mathcal{H}_{\mathrm{d}}$ and the spatial discretized matrix S for the operator $\mathcal{S}$ can be obtained in the same way as we used to discretize $\mathcal{H}_{\mathrm{s}}$ in

Section 2.2.2. Expressed on the lattice, Eq. (2.7) reads

$$\frac{\partial}{\partial t}\Psi(t) = H\Psi(t) - S(t) = (H_{\mathrm{s}} + H_{\mathrm{d}})\Psi(t) - S(t). \tag{2.44}$$

The formal solution of Eq. (2.44) is given by

$$\Psi(t) = e^{tH}\Psi(0) - \int_0^t e^{(t-u)H} S(u)du. \tag{2.45}$$

Time-marching methods solve Eq. (2.45) by advancing the fields $\Psi(t)$ in small steps using a small time-step τ. From Eq. (2.45), it follows directly that

$$\Psi(t+\tau) = e^{\tau H}\Psi(t) - \int_0^\tau e^{uH} S(t+\tau-u)du. \tag{2.46}$$

The convolution part in Eq. (2.46) can be easily removed by invoking the standard n-point Gauss-Legendre quadrature formulas [35]

$$\int_0^\tau e^{uH} S(t+\tau-u)du = \frac{\tau}{2}\sum_{i=1}^{n} w_i e^{(1+x_i)H/2} S(t+(1-x_i)\tau/2) + O(\tau^{2n+1}), \tag{2.47}$$

where x_i is the i-th zero of the Legendre polynomial $P_n(x)$ and the weights are given by $w_i = 2/(1-x_i^2)[P_n'(x_i)]^2$. In most applications, the time and spatial dependence of the source term can be separated, that is $S(t) = f(t)S_0$, where $f(t)$ is a scalar function and S_0 is a matrix that may depend on spatial coordinates only. Then Eq. (2.47) reduces to a much simpler expression:

$$\int_0^\tau e^{uH} S(t+\tau-u)du = \frac{\tau}{2}\sum_{i=1}^{n} f(t+(1-x_i)\tau/2) w_i e^{(1+x_i)H/2} S_0. \tag{2.48}$$

As there are only n (which is small) extra calculations of the matrix exponential in this expression, the work to compute this expression is negligible to the work required to perform the time stepping itself. Generally, $n = 3$ is sufficient as the time-step τ is normally quite small. For $n = 3$ we have $x_1 = 0$, $x_2 = \sqrt{3/5}$, $x_3 = -\sqrt{3/5}$ and $w_1 = 8/9$, $w_2, w_3 = 5/9$.

The first term in Eq. (2.46) can be computed by the matrix decomposition approach, for example by using the second-order approximation

$$e^{\tau H}\Psi(t) = e^{\tau(H_{\mathrm{s}}+H_{\mathrm{d}})}\Psi(t) = e^{\tau H_{\mathrm{d}}/2} e^{\tau H_{\mathrm{s}}} e^{\tau H_{\mathrm{d}}/2}\Psi(t). \tag{2.49}$$

Obviously, as H_{s} consists of a sum of commuting matrices, the matrix exponential $\exp(\tau H_{\mathrm{s}})$ can be computed using the method discussed in Section 2.2. As the matrix H_{d} is diagonal, the matrix exponential $\exp(\tau H_{\mathrm{d}}/2)$ just consists of the exponentials of its diagonal elements.

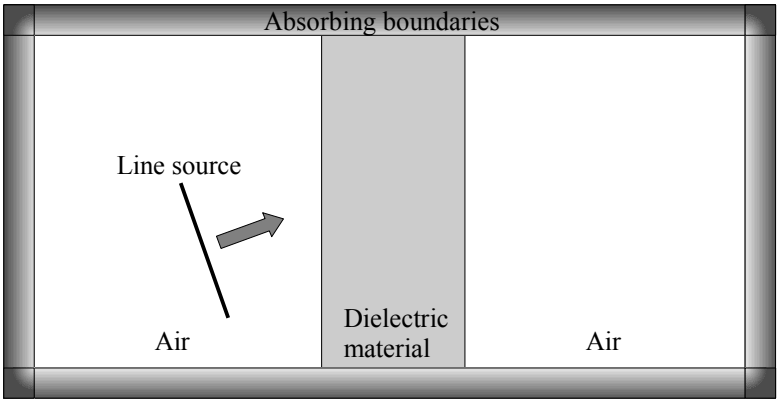

Figure 2.3: Schematic picture of the two-dimensional simulation area.

For a detailed account of the technical aspects of the implementation, see [22].

For the two-dimensional case, we use the z-component of $\mathbf{J}_{\mathrm{source}}$ in the TM mode computations and the z-component of $\mathbf{M}_{\mathrm{source}}$ for the TE mode calculations. The materials of the four boundaries of the simulation area are absorbing with σ and σ^* non-zero. To reduce the reflections from the absorbing boundaries, we use the matching condition $\sigma/\sqrt{\varepsilon} = \sigma^*/\sqrt{\mu}$, and let $\sigma/\sqrt{\varepsilon} = \sigma^*/\sqrt{\mu}$ gradually increase from zero at the interior interface to its maximum value at the outer interface (see Fig. 2.3).

2.4 Density of states and local density of states

The calculation of the distribution of eigenvalues of very large matrices, that is the density of states (DOS) is a common problem in physics. For many-body systems, this distribution determines the thermodynamic properties of the system [36]. In the description of light-matter interaction, the DOS enters the expression for the light absorption and emission. In this subsection, $D = N_x N_y$ denotes the number of mesh points on the two-dimensional Yee lattice. Then, the dimension of the matrix H is $D \times D$. The most direct method to compute the DOS, i.e. all the eigenvalues, is to diagonalize the matrix H. This approach has at least one obvious limitation: The amount of memory required by state-of-the-art algorithms to diagonalize H grows as D^2 [37, 38]. The scaling behavior with D limits the application of this approach to matrices of dimension $D = \mathcal{O}(10^4)$, which is too small for many problems of interest.

For practical purposes, we need methods that scale linearly with D. To the best of our knowledge, the first of such algorithms was given by Alben *et al.* [39], who applied it to electron

motion in disordered alloy models. In this approach the DOS is obtained by solving the time-dependent Schrödinger equation of a particle moving on a lattice, followed by a Fourier transform of the single-particle Green's function [39]. Later, it was shown that the eigenvalue spectrum of a particle moving in continuum space can be computed in the same manner [40]. Fast algorithms of this kind proved useful to study various aspects of localization of waves [41–43] and other one-particle problems [44–49]. DOS calculations for matrices of dimension $10^7 \times 10^7$ have been reported [50]. A common feature of these fast algorithms is that they solve the wave equation for a sample of randomly chosen initial states. The efficiency of this approach as a whole relies on the hypothesis (suggested by the central limit theorem) that satisfactory accuracy can be achieved by using a small sample of initial states. A mathematical justification of this method has been given in [51].

The distribution of eigenvalues or DOS of the matrix H is defined as

$$\mathcal{D}(\omega) = \sum_{n=1}^{D} \delta(\omega - \lambda_n) = \frac{1}{2\pi} \int_{-\infty}^{\infty} e^{it\omega}\, \mathbf{Tr}(e^{tH})\, dt, \tag{2.50}$$

where n runs over all the eigenvalues λ_n of H. The crux of all fast $\mathcal{O}(D)$ methods is that the trace in Eq. (2.50) can be estimated by sampling over random vectors and that the accuracy of the estimate *increases* with the dimension D [51].

In this thesis, we focus on the local radiative density of states (LRDOS), local referring to a point on the Yee lattice [52]. The LRDOS is defined as

$$N_{rad}(\omega, \mathbf{r}) = \varepsilon(\mathbf{r})^{-1} N(\omega, \mathbf{r}), \tag{2.51}$$

where

$$N(\omega, \mathbf{r}) = \sum_{n=1}^{D} \delta(\omega - \lambda_n) |\phi_n(\mathbf{r})|^2 = \int_{-\infty}^{\infty} e^{i\omega t}\, \langle \mathbf{r} | e^{tH} \mathbf{r} \rangle\, dt, \tag{2.52}$$

denotes the local density of states (LDOS). In Eq. (2.52) $\phi_n(\mathbf{r})$ denotes the eigenstate corresponding to the eigenvalue λ_n. Eq. (2.52) also suggests how we can compute the LRDOS without solving the eigenvalue problem for H: Simply set the electromagnetic field at the point $\mathbf{r}$ to one, set all other fields to zero, solve the Maxwell equations and store the values of $f(t) = \varepsilon(\mathbf{r})^{-1} \langle \mathbf{r} | e^{tH} \mathbf{r} \rangle$. The (fast) Fourier transform of $f(t)$ then yields the LRDOS.

Chapter 3

Light propagation in dielectric materials

The time-dependent Maxwell equations are frequently used as a mathematical framework to describe the propagation of light in dielectric materials. In this chapter we closely follow [16] to describe light propagation in conventional dielectric materials. Then concepts are generalized to describe light propagation in homogeneous isotropic negative index materials and in photonic crystals.

3.1 Conventional lossless dielectric materials

3.1.1 Velocity of light and refraction index

From Maxwell's equations (see Eq. (2.4)) it follows that if the medium is homogeneous, in addition to be isotropic, and if there are no electric and magnetic currents, the equations for the electric field vector $\mathbf{E}$ and the magnetic field vector $\mathbf{H}$ are given by

$$\nabla^2\mathbf{E} - \varepsilon\mu\frac{\partial^2\mathbf{E}}{\partial t^2} = 0, \tag{3.1a}$$

$$\nabla^2\mathbf{H} - \varepsilon\mu\frac{\partial^2\mathbf{H}}{\partial t^2} = 0. \tag{3.1b}$$

Eqs. (3.1a) and (3.1b) are standard equations of wave motion and suggest the existence of electromagnetic waves propagating with a velocity

$$v = 1/\sqrt{\varepsilon\mu} = c/\sqrt{\varepsilon_r\mu_r}, \tag{3.2}$$

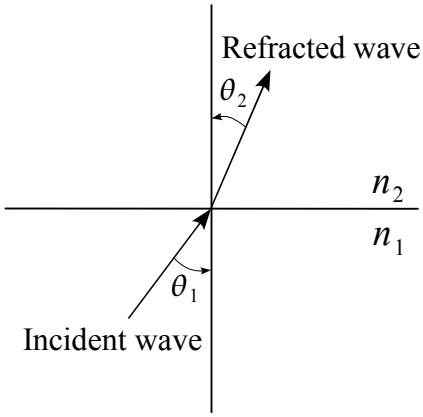

Figure 3.1: Illustration of the refraction of a plane wave. The angles θ_1 and θ_2 are measured in a counterclockwise or positive direction.

where $c = 1/\sqrt{\varepsilon_0 \mu_0}$ denotes the velocity of light in vacuum ($\approx 3 \times 10^8$m/s). Since usually $\varepsilon_r > 1$ and $\mu_r \approx 1$ for transparent substances, the velocity v is smaller than the velocity of light in vacuum. The velocity v is usually determined only relative to c by making use of the law of refraction or Snell's law (for a derivation see [16] and Section 3.1.5)

$$\frac{\sin\theta_1}{\sin\theta_2} = \frac{v_1}{v_2} = n_{12}, \tag{3.3}$$

where θ_1 and θ_2 are the angles made by the electromagnetic wave with the normal of the interface between the media 1 and 2, in the first and second medium, respectively (see Fig. 3.1) and n_{12} denotes the refractive index for refraction from the first into the second medium. The absolute refractive index n of a medium, that is the refractive index for refraction from vacuum into that medium is defined as

$$n = \frac{c}{v}. \tag{3.4}$$

Hence,

$$n_{12} = \frac{n_2}{n_1} = \frac{v_1}{v_2}, \tag{3.5}$$

where n_1 and n_2 are the absolute refractive indices of medium 1 and 2, respectively. From Eqs. (3.2) and (3.4) follows the Maxwell formula

$$n = \sqrt{\varepsilon_r \mu_r}. \tag{3.6}$$

For non-magnetic materials $\mu_r \approx 1$. In general ε_r depends on the frequency ω of the electromagnetic field. In this way the atomic structure and the dynamics of matter can be taken into

account. For the numerical simulations presented in this and the following chapters, however, we assume that ε_r does not depend on frequency. Materials with real and positive material parameters ε_r and μ_r are often called conventional lossless dielectric materials.

3.1.2 Phase, group front and group velocity

The velocity of a wave is an important concept for practical applications (for example, signal transmission). For wave packets two velocities are of importance, the phase and the group velocity. The realization of materials showing negative refraction of light created a dispute about the sign of the phase and group velocity [53–55]. Much of the confusion was caused by inconsistent definitions of the group velocity. A clear formulation of wave propagation, with definitions for the phase and group velocity, in multidimensional space for isotropic and lossless media is given in [56]. In [56] errors made in classical works on optics are pointed out regarding the group velocity in three dimensions. Therefore, we follow [56] for the definition of the phase and group velocity in multidimensional space.

From Eq. (3.1) it follows that in a homogeneous isotropic medium, each Cartesian component $\mathbf{V}(\mathbf{r}, t)$ of the field vectors $\mathbf{E}$ and $\mathbf{H}$ satisfies the homogeneous wave equation [16]

$$\nabla^2 \mathbf{V} - \frac{1}{v^2} \frac{\partial^2 \mathbf{V}}{\partial t^2} = 0, \tag{3.7}$$

where $\mathbf{r}$ denotes the position vector of a point in space. We consider as a solution of Eq. (3.7) a time harmonic wave propagating in the direction of the wave vector $\mathbf{k} = k\mathbf{u}$ ($\mathbf{u}$ is a unit vector)

$$\mathbf{E}(\mathbf{r}, t) = E_0(\mathbf{r}) e^{-i(\omega t - \mathbf{k}\cdot\mathbf{r} + \Phi)} = E_0(\mathbf{r}) e^{-i\Phi} e^{-i(\omega t - \mathbf{k}\cdot\mathbf{r})}, \tag{3.8a}$$

$$\mathbf{H}(\mathbf{r}, t) = H_0(\mathbf{r}) e^{-i(\omega t - \mathbf{k}\cdot\mathbf{r} + \Phi)} = H_0(\mathbf{r}) e^{-i\Phi} e^{-i(\omega t - \mathbf{k}\cdot\mathbf{r})}, \tag{3.8b}$$

where ω is called the angular frequency, Φ is a constant phase factor, and $E_0(\mathbf{r})$ and $H_0(\mathbf{r})$ are positive real scalar functions. Very often the amplitudes of the wave functions are considered to be complex, with their phase equal to the constant part Φ of the argument of the wave function. The waves have a frequency

$$f = \frac{\omega}{2\pi}, \tag{3.9}$$

and a wavelength

$$\lambda = \frac{v}{f} = v \frac{2\pi}{\omega}. \tag{3.10}$$

The length k of the wave vector $\mathbf{k}$, which is by definition positive, is given by

$$k = \frac{2\pi}{\lambda} = \frac{\omega}{v} = \frac{|n|\omega}{c} = \omega\sqrt{\varepsilon\mu}. \tag{3.11}$$

In optics k is often called the wave number. The surfaces $\mathbf{k}\cdot\mathbf{r} = const$, that are surfaces of constant phase, are called wave fronts. In multidimensional space the phase velocity, that is the smallest speed at which the wave front propagates in the direction of the wave vector $\mathbf{k}$, is defined as [56]

$$\mathbf{v}_p = \frac{\omega}{k}\frac{\mathbf{k}}{k}. \tag{3.12}$$

The magnitude of the phase velocity is

$$v_p = \frac{\omega}{k}. \tag{3.13}$$

Usually, a wave is a superposition of waves of slightly different frequencies and wave numbers. In such a case we call the wave a wave group or wave packet. To study the propagation of a wave packet we consider for the sake of simplicity and without loss of generality, two monochromatic plane waves of the same amplitude and slightly different frequencies and wave numbers

$$\mathbf{E}(\mathbf{r},t) = E_0 e^{-i(\omega t - \mathbf{k}\cdot\mathbf{r})} + E_0 e^{-i((\omega+\delta\omega)t - (\mathbf{k}+\delta\mathbf{k})\cdot\mathbf{r})}. \tag{3.14}$$

Eq. (3.14) can be rewritten as follows

$$\mathbf{E}(\mathbf{r},t) = 2E_0 \cos\left[\frac{1}{2}(t\delta\omega - \mathbf{r}\cdot\delta\mathbf{k})\right] e^{-i(\bar{\omega}t - \bar{\mathbf{k}}\cdot\mathbf{r})}, \tag{3.15}$$

where $\bar{\omega} = \omega + \delta\omega/2$ and $\bar{\mathbf{k}} = \mathbf{k} + \delta\mathbf{k}/2$ are the mean frequency and mean wave vector, respectively.

The cosine term in Eq. (3.15) describes the variation with time and position of the amplitude of the wave packet. The surfaces $\delta\mathbf{k}\cdot\mathbf{r} - t\delta\omega = const$ are constant-amplitude surfaces or group fronts. The group-front velocity [56]

$$\mathbf{v}_{gf} = \frac{\delta\omega}{\delta k}\frac{\delta\mathbf{k}}{\delta k} = \frac{\delta\mathbf{k}}{\delta k}\left[\left(\frac{\delta k_x}{\delta\omega}\right)^2 + \left(\frac{\delta k_y}{\delta\omega}\right)^2 + \left(\frac{\delta k_z}{\delta\omega}\right)^2\right]^{-1/2}, \tag{3.16}$$

describes the propagation orthogonal to the group front and is the smallest speed at which the group front travels. The group-front velocity is generally not parallel to the phase velocity and has sometimes incorrectly been identified as the group velocity [56]. The definition of the group velocity is [56]

$$\mathbf{v}_g = \nabla_k\omega. \tag{3.17}$$

In a normal dispersive, nondissipative and isotropic medium, the group velocity can be ex-

pressed as [56]

$$\mathbf{v}_g = \frac{\partial\omega}{\partial k}\frac{\mathbf{k}}{k}. \tag{3.18}$$

The magnitude of the group velocity is

$$v_g = \frac{\partial\omega}{\partial k}. \tag{3.19}$$

For linear wave propagation in a homogeneous, nondissipative media, it can be proven that the group velocity and energy velocity are equal (see for example [57, 58] and references therein). The group velocity thus identifies the direction and the speed of energy propagation. This is not true in general, since in regions of anomalous dispersion the magnitude of the group velocity may become greater than the speed of light or may become negative [59–63].

3.1.3 Phase and group refractive index

Sometimes the refractive index n is also called the phase refractive index n_p, because it is related to the phase velocity v_p. In terms of the frequency ω of the wave and the wave vector k we have

$$v_p = \frac{c}{|n_p|} = \frac{c}{|n|} = \frac{\omega}{k}. \tag{3.20}$$

The refractive index is thus always defined with respect to the phase velocity. In analogy to the phase refractive index also a group refractive index or group index n_g can be defined

$$n_g = \frac{c}{v_g} = c\frac{\partial k}{\partial\omega}, \tag{3.21}$$

where use has been made of Eq. (3.19). If the medium is nondispersive, the phase and group velocity and hence the refractive and group index are the same. However, in general this is not the case. In a homogeneous isotropic dielectric medium the relation between the group index n_g and the refractive index n is given by

$$n_g = c\frac{\partial k}{\partial\omega} = \frac{\partial}{\partial t}(\omega|n|) = |n| + \omega\frac{\partial|n|}{\partial\omega}. \tag{3.22}$$

3.1.4 Poynting vector

For a plane electromagnetic wave with wave vector $\mathbf{k}$ and angular frequency ω, the Maxwell's and material equations reduce to

$$\mathbf{k}\times\mathbf{E} = \omega\mu\mathbf{H}, \tag{3.23a}$$

$$\mathbf{k}\times\mathbf{H} = -\omega\varepsilon\mathbf{E}. \tag{3.23b}$$

Projection on $\mathbf{k}$ gives

$$\mathbf{k} \cdot \mathbf{E} = 0, \tag{3.24a}$$

$$\mathbf{k} \cdot \mathbf{H} = 0. \tag{3.24b}$$

Hence the electric and magnetic field vectors lie in planes which are normal to the direction of propagation. Since for the materials discussed in this section ε and μ are simultaneously positive, $\mathbf{E}$, $\mathbf{H}$ and $\mathbf{k}$ form a right-handed set of vectors. The energy flux associated with the electromagnetic wave is denoted by the Poynting vector

$$\mathbf{S} = \mathbf{E} \times \mathbf{H}. \tag{3.25}$$

From Eq. (3.25) if follows that also $\mathbf{S}$, $\mathbf{E}$ and $\mathbf{H}$ form a right-handed set of vectors. Hence, $\mathbf{S}$ and $\mathbf{k}$ are parallel, that are positive multiples of the same unit vector $\mathbf{u}$ and thus

$$\mathbf{S} \cdot \mathbf{k} > 0. \tag{3.26}$$

As seen in Section 3.1.2, if the medium is not strongly dispersive the group velocity identifies the direction of energy propagation, and thus

$$\mathbf{S} \cdot \mathbf{v}_g > 0. \tag{3.27}$$

From Eqs. (3.26) and (3.27) it follows that for homogeneous isotropic dielectric media with simultaneously positive ε and μ

$$\mathbf{v}_g \cdot \mathbf{k} > 0. \tag{3.28}$$

The group velocity is called positive, that is having the same sign as the wave vector.

If we now assume that the unit vector $\mathbf{u}$ is defined through the Poynting vector $\mathbf{S}$, we can write

$$\mathbf{S} = S\mathbf{u}, \tag{3.29}$$

with $S > 0$ by definition. Since also $\mathbf{k}$ is a positive multiple of $\mathbf{u}$ we can write

$$\mathbf{k} = \beta k \mathbf{u} = \beta \frac{|n|\omega}{c} \mathbf{u}, \tag{3.30}$$

with $\beta = +1$. Defining $n = \beta|n|$ as the refractive index of the medium, it follows that homogeneous isotropic dielectric media with simultaneously positive permeability and permittivity have a positive refractive index. Rewriting the group velocity as

$$\mathbf{v}_g = \beta \frac{\partial \omega}{\partial k} \mathbf{u}, \tag{3.31}$$

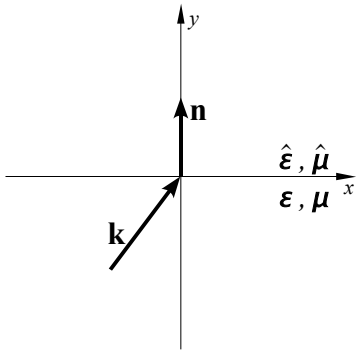

Figure 3.2: Incident plane wave with wave vector $\mathbf{k}$ hits the plane interface $y = 0$ between two different media characterized by ε, μ and $\hat{\varepsilon}$, $\hat{\mu}$, respectively. $\mathbf{n}$ denotes a unit normal vector.

and making use of Eq. (3.27) leads to the condition that

$$\beta \frac{\partial \omega}{\partial k} > 0. \tag{3.32}$$

Hence, for media that are not strongly dispersive, β and $\frac{\partial \omega}{\partial k}$ always have the same sign. Rewriting the phase velocity as

$$\mathbf{v}_p = \beta \frac{\omega}{k} \mathbf{u}, \tag{3.33}$$

it can be concluded that

$$\mathbf{v}_p \cdot \mathbf{k} > 0. \tag{3.34}$$

Hence, in homogeneous isotropic dielectric media with simultaneously positive ε and μ both the group velocity and the phase velocity are positive, that is having the same sign as the wave vector, or equivalently being parallel to the wave vector.

3.1.5 Reflection and refraction at an interface

When a plane wave falls on to an interface between two homogeneous isotropic media of different optical properties, it is split into two waves: a transmitted (refracted) wave proceeding into the second medium and a reflected wave propagating back into the first medium [16]. We assume that the reflected and refracted waves are also plane waves and derive expressions for their directions of propagation and their amplitudes.

We consider a plane wave with wave vector $\mathbf{k}$ and frequency ω that is incident from a homogeneous isotropic medium with optical properties ε and μ. At the boundary with a second homogeneous isotropic medium with optical properties $\hat{\varepsilon}$ and $\hat{\mu}$ the wave is split. The reflected

and refracted plane waves have wave vectors and frequencies $\tilde{\mathbf{k}}$, $\tilde{\omega}$ and $\hat{\mathbf{k}}$, $\hat{\omega}$, respectively. We define $\mathbf{n}$ as a unit normal directed from medium ε, μ into medium $\hat{\varepsilon}$, $\hat{\mu}$. At the boundary between the two media the time variation of all fields must be the same. Hence, at a point $\mathbf{r}(x, y, z)$ on the boundary we have

$$\omega t - \mathbf{k} \cdot \mathbf{r} = \tilde{\omega} t - \tilde{\mathbf{k}} \cdot \mathbf{r} = \hat{\omega} t - \hat{\mathbf{k}} \cdot \mathbf{r}. \tag{3.35}$$

If we take the boundary as the plane $y = 0$, Eq. (3.35) results in

$$\omega t - (k_x x + k_z z) = \tilde{\omega} t - (\tilde{k}_x x + \tilde{k}_z z) = \hat{\omega} t - (\hat{k}_x x + \hat{k}_z z). \tag{3.36}$$

Since Eq. (3.36) must hold for all t and all x and z on the boundary, we have

$$\omega = \tilde{\omega} = \hat{\omega}, \quad k_x = \tilde{k}_x = \hat{k}_x, \quad k_z = \tilde{k}_z = \hat{k}_z. \tag{3.37}$$

Eq. (3.37) shows that both the reflected and refracted wave lie in the plane of incidence, that is the plane specified by the incident wave vector $\mathbf{k}$ and the normal $\mathbf{n}$. Taking the plane of incidence as the xy-plane gives $k_z = \tilde{k}_z = \hat{k}_z = 0$. A schematic picture is shown in Fig. 3.2. From Eq. (3.37) it follows that the tangential component of the incident wave vector is conserved upon reflection and refraction.

The energy flow associated with the incident electromagnetic wave is denoted by the Poynting vector

$$\mathbf{S} = \mathbf{E} \times \mathbf{H} = \frac{1}{\omega\mu}(\mathbf{E} \times (\mathbf{k} \times \mathbf{E})) = \frac{E^2}{\omega\mu}\mathbf{k}. \tag{3.38}$$

From Eq. (3.38) it can be seen that for a medium with $\mu > 0$, $\mathbf{S} \cdot \mathbf{k} > 0$, a result already derived in Section 3.1.4 for materials with simultaneously positive ε and μ. Note that since

$$k_x^2 + k_y^2 = k^2 = \varepsilon\mu\omega^2, \tag{3.39}$$

ε and μ always have the same sign for homogeneous isotropic dielectric media. Also for the reflected wave $\tilde{\mathbf{S}}$ and $\tilde{\mathbf{k}}$ are parallel, that is $\tilde{\mathbf{S}} \cdot \tilde{\mathbf{k}} > 0$. If also the second medium has $\hat{\mu} > 0$, then $\hat{\mathbf{S}} \cdot \hat{\mathbf{k}} > 0$.

If the incident wave hits the boundary, the energy flux of the reflected and refracted wave is such that the energy flows away from the interface. The incident, reflected and refracted waves thus propagate as indicated in Fig. 3.3. If we define the angles $0 < \theta, \tilde{\theta}, \hat{\theta} \leq \pi/2$ as

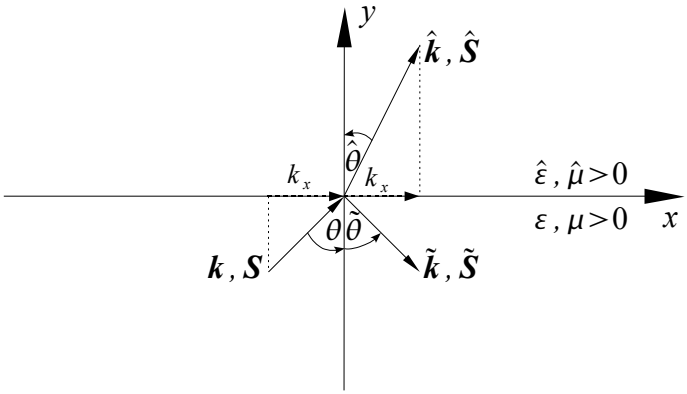

Figure 3.3: Reflection and refraction of a plane wave at an interface between two homogeneous isotropic media of different optical properties, characterized by $\varepsilon, \mu > 0$ and $\hat{\varepsilon}, \hat{\mu} > 0$, respectively. $\mathbf{k}$ and $\mathbf{S}$ are the wave vector and Poynting vector of the incident wave, $\tilde{\mathbf{k}}$ and $\tilde{\mathbf{S}}$ are the wave vector and Poynting vector of the reflected wave and $\hat{\mathbf{k}}$ and $\hat{\mathbf{S}}$ are the wave vector and Poynting vector of the refracted wave. θ, $\tilde{\theta}$ and $\hat{\theta}$ correspond to the angle of incidence, the angle of reflection and the angle of refraction, respectively. The angles are measured in a counterclockwise or positive direction.

indicated in Fig. 3.3 we have

$$k_x = k\cos(\frac{\pi}{2} - \theta) = k\sin\theta, \tag{3.40a}$$

$$k_y = k\sin(\frac{\pi}{2} - \theta) = k\cos\theta, \tag{3.40b}$$

$$\tilde{k}_x = \tilde{k}\cos(\frac{3\pi}{2} + \tilde{\theta}) = \tilde{k}\sin\tilde{\theta}, \tag{3.40c}$$

$$\tilde{k}_y = \tilde{k}\sin(\frac{3\pi}{2} + \tilde{\theta}) = -\tilde{k}\cos\tilde{\theta}, \tag{3.40d}$$

$$\hat{k}_x = \hat{k}\cos(\frac{\pi}{2} - \hat{\theta}) = \hat{k}\sin\hat{\theta}, \tag{3.40e}$$

$$\hat{k}_y = \hat{k}\sin(\frac{\pi}{2} - \hat{\theta}) = \hat{k}\cos\hat{\theta}. \tag{3.40f}$$

From Eqs. (3.37) and (3.40) it follows that

$$\theta = \tilde{\theta}, \tag{3.41}$$

and

$$\frac{\sin\theta}{\sin\hat{\theta}} = \frac{\hat{k}}{k} = \frac{|\hat{n}|}{|n|}, \tag{3.42}$$

where use has been made of $\tilde{k} = k = |n|\omega/c$. Relation (3.41), together with the statement that the reflected wave vector is in the plane of incidence, constitute the law of reflection [16].

Relation (3.42), together with the statement that the refracted wave vector is in the plane of incidence, constitute the law of refraction or Snell's law [16].

We now consider the amplitudes of the reflected and refracted waves. The electric and magnetic field vectors obey the Maxwell equations and material equations. Across the boundary of the two homogeneous isotropic dielectric media the tangential component of $\mathbf{E}$ and $\mathbf{H}$ should be continuous [16]. Hence we must have

$$\mathbf{n} \times (\mathbf{E} + \tilde{\mathbf{E}}) = \mathbf{n} \times \hat{\mathbf{E}}, \tag{3.43a}$$
$$\mathbf{n} \times (\mathbf{H} + \tilde{\mathbf{H}}) = \mathbf{n} \times \hat{\mathbf{H}}, \tag{3.43b}$$

and thus

$$E_x + \tilde{E}_x = \hat{E}_x, \tag{3.44a}$$
$$E_z + \tilde{E}_z = \hat{E}_z, \tag{3.44b}$$
$$H_x + \tilde{H}_x = \hat{H}_x, \tag{3.44c}$$
$$H_z + \tilde{H}_z = \hat{H}_z. \tag{3.44d}$$

Also the normal components of $\mathbf{D}$ and $\mathbf{B}$ should be continuous across the boundary [16]

$$(\mathbf{D} + \tilde{\mathbf{D}}) \cdot \mathbf{n} = \hat{\mathbf{D}} \cdot \mathbf{n}, \tag{3.45a}$$
$$(\mathbf{B} + \tilde{\mathbf{B}}) \cdot \mathbf{n} = \hat{\mathbf{B}} \cdot \mathbf{n}, \tag{3.45b}$$

and by making use of Eq. (2.3)

$$\varepsilon(E_y + \tilde{E}_y) = \hat{\varepsilon}\hat{E}_y, \tag{3.46a}$$
$$\mu(H_y + \tilde{H}_y) = \hat{\mu}\hat{H}_y. \tag{3.46b}$$

From Eqs. (3.23b), (3.44a), (3.44d) and the fact that $k_z = \tilde{k}_z = \hat{k}_z = 0$ it follows that

$$\frac{\hat{H}_z}{H_z} = \frac{\hat{\varepsilon}(k_y - \tilde{k}_y)}{\varepsilon\hat{k}_y - \hat{\varepsilon}\tilde{k}_y}. \tag{3.47}$$

For the case $\varepsilon, \mu > 0$ and $\hat{\varepsilon}, \hat{\mu} > 0$, $\tilde{k}_y = -k_y = -|n|\omega/c \cos\theta$ and $\hat{k}_y = |n|\omega/c \cos\hat{\theta}$ (see Eq. (3.40)). Hence, for the special case of a conventional homogeneous dielectric medium with $\mu = \hat{\mu} = 1$, $n = \sqrt{\varepsilon}$ and $\hat{n} = \sqrt{\hat{\varepsilon}}$, we have [16]

$$\frac{\hat{H}_z}{H_z} = \frac{2|\hat{n}| \cos\theta}{|n| \cos\hat{\theta} + |\hat{n}| \cos\theta}. \tag{3.48}$$

Using Eqs. (3.37), (3.23b), (3.24b), (3.44b), (3.44c) and the fact that $k_z = \tilde{k}_z = \hat{k}_z = 0$ we

obtain

$$\frac{\hat{H}_x}{H_x} = \frac{\hat{\varepsilon}\tilde{k}_y}{k_y}\frac{(k_x^2 - k_y\tilde{k}_y)(k_y - \tilde{k}_y)}{\hat{\varepsilon}\hat{k}_y(\tilde{k}_y^2 + k_x^2) - \varepsilon\hat{k}^2\tilde{k}_y}, \tag{3.49}$$

where $\hat{k}^2 = \hat{k}_x^2 + \hat{k}_y^2 = \omega^2\hat{\varepsilon}\hat{\mu}$. Using the relations in Eq. (3.40) for materials with $\mu = \hat{\mu} = 1$, $n = \sqrt{\varepsilon}$ and $\hat{n} = \sqrt{\hat{\varepsilon}}$, we find [16]

$$\frac{\hat{H}_x}{H_x} = \frac{2|\hat{n}|\cos\hat{\theta}}{|n|\cos\hat{\theta} + |\hat{n}|\cos\theta}. \tag{3.50}$$

The expression for $\hat{H}_y/H_y$ follows from Eq. (3.24b),

$$\frac{\hat{H}_y}{H_y} = \frac{\hat{k}_x}{\hat{k}_y}\frac{k_y}{k_x}\frac{\hat{H}_x}{H_x}. \tag{3.51}$$

Using the relations in Eq. (3.40) for the case $\varepsilon, \mu > 0$ and $\hat{\varepsilon}, \hat{\mu} > 0$, Eq. (3.51) can be rewritten as

$$\frac{\hat{H}_y}{H_y} = \frac{\sin\hat{\theta}\cos\theta}{\sin\theta\cos\hat{\theta}}\frac{\hat{H}_x}{H_x}. \tag{3.52}$$

The relative amplitudes for the reflected waves can be found by making use of Eqs. (3.44c), (3.44d) and (3.46b),

$$\frac{\tilde{H}_z}{H_z} = \frac{\hat{H}_z}{H_z} - 1, \tag{3.53a}$$

$$\frac{\tilde{H}_x}{H_x} = \frac{\hat{H}_x}{H_x} - 1, \tag{3.53b}$$

$$\frac{\tilde{H}_y}{H_y} = \frac{\hat{\mu}}{\mu}\frac{\hat{H}_y}{H_y} - 1. \tag{3.53c}$$

The relative amplitudes for the $\mathbf{E}$ fields can be found from the ones of the $\mathbf{H}$ fields by interchanging the role of ε and μ and $\hat{\varepsilon}$ and $\hat{\mu}$.

3.1.6 Total internal reflection

In the optical frequency regime, the range of refractive indices of materials is limited typically between 1 and 4. From Snell's law it can be seen that if light crosses an interface into a medium with a higher index of refraction, the light bends towards the normal, as illustrated in Fig. 3.4a. If light travels across an interface from a material with higher refractive index to a material with lower refractive index, then it will bend away from the normal, as can be seen from Fig. 3.4b. For both cases $n < \hat{n}$ and $n > \hat{n}$, the refracted beam and the incident beam are positioned at opposite sides of the normal. The case $n > \hat{n}$ is somewhat special.

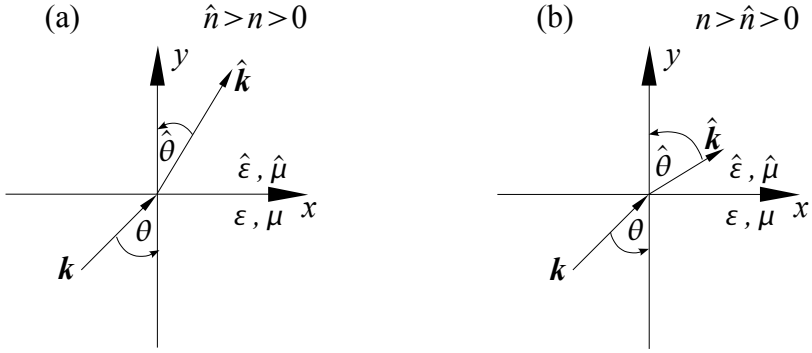

Figure 3.4: Illustration of the refraction of light at the interface between two homogeneous isotropic media with refractive indices $n > 0$ and $\hat{n} > 0$. $\mathbf{k}$ is the incident wave vector and $\hat{\mathbf{k}}$ is the refracted wave vector. θ corresponds to the angle of incidence and $\hat{\theta}$ to the refracted angle. The angles are measured in a counterclockwise or positive direction.

At some angle, known as the critical angle θ_c, light traveling from medium 1 with refractive index n to medium 2 with refractive index $\hat{n}$ will be refracted at $90°$, that is refraction along the interface. This can be seen as follows. From the relations

$$k_x^2 + k_y^2 = \omega^2 \varepsilon \mu, \tag{3.54}$$

and

$$\hat{k}_x^2 + \hat{k}_y^2 = \omega^2 \hat{\varepsilon} \hat{\mu}, \tag{3.55}$$

it follows that

$$\hat{k}_y^2 = \left(\frac{\hat{\varepsilon}\hat{\mu}}{\varepsilon\mu} - 1 \right) k_x^2 + \frac{\hat{\varepsilon}\hat{\mu}}{\varepsilon\mu} k_y^2, \tag{3.56}$$

where use has been made of the fact that the tangential component of the incident wave vector is conserved upon refraction, that is $\hat{k}_x = k_x$. If a wave should propagate in medium 2, then $\hat{k}_y$ should be real and thus

$$\left(\frac{\hat{\varepsilon}\hat{\mu}}{\varepsilon\mu} - 1 \right) k_x^2 + \frac{\hat{\varepsilon}\hat{\mu}}{\varepsilon\mu} k_y^2 > 0. \tag{3.57}$$

Note that if $\hat{\varepsilon}\hat{\mu} > \varepsilon\mu$ (or $\hat{n} > n$), then condition (3.57) is always fulfilled. Substituting the expressions for k_x and k_y from Eq. (3.40) into Eq. (3.57) gives

$$\sin^2 \theta < \frac{\hat{\varepsilon}\hat{\mu}}{\varepsilon\mu}. \tag{3.58}$$

Thus, if the angle of incidence is larger than $\theta_c = \arcsin(\hat{n}/n)$, the incident light beam will not pass through the second medium at all. All the light is totally reflected off the interface,

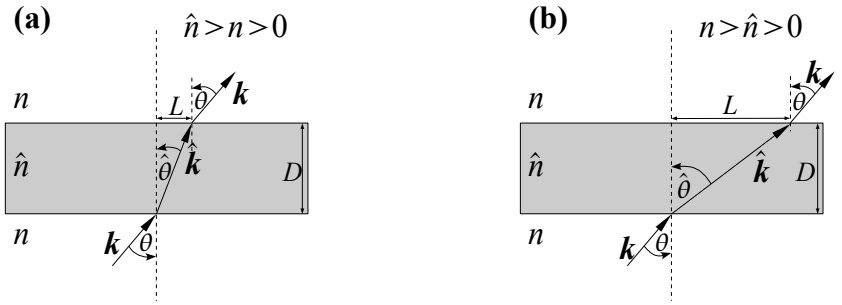

Figure 3.5: Illustration of the propagation of light through a slab of material of thickness D with refractive index $\hat{n}$. The refractive index of the surrounding homogeneous isotropic dielectric medium is denoted by n. L denotes the displacement of the light beam. The angles are measured in a counterclockwise or positive direction.

a phenomenon that is known as total internal reflection. Note that there is always a reflected beam, also for the case $n < \hat{n}$.

3.1.7 Propagation through a slab

Experimentally, the refractive index of a material can be determined from the apparent displacement L of an electromagnetic wave when it travels through a slab of thickness D of this material

$$\hat{n} = \frac{n \sin\theta}{\sin(\arctan(L/D))}, \tag{3.59}$$

as illustrated in Fig. 3.5a,b for the cases $n < \hat{n}$ and $n > \hat{n}$, respectively. As can be seen from Fig. 3.5, the shift L is always much larger for the case $n > \hat{n}$ than for the case $n < \hat{n}$.

3.1.8 FDTD simulation of refraction in a homogeneous isotropic slab

Using our finite-difference time domain (FDTD) simulation code described in Chapter 2, we simulate the refraction of a light beam in a slab of a homogeneous, isotropic dielectric material with refractive index $\hat{n}$. We assume that the surrounding medium is vacuum ($n = 1$). We simulate two illustrative cases, one for $\hat{n} = 2$ and one for $\hat{n} = 0.8$. We consider a slab of dimension $12\lambda \times 40\lambda$ and optical parameters $\hat{\varepsilon} = 4, \hat{\mu} = 1$ ($\hat{n} = 2$) and $\hat{\varepsilon} = 0.64, \hat{\mu} = 1$ ($\hat{n} = 0.8$), respectively. The total simulation area has dimensions $L_x = 44\lambda$ and $L_y = 40\lambda$. The boundaries of the box are absorbing. We discretize the space in a square grid with lattice spacing $\delta = 0.02\lambda$. This results in a total number of 440000 lattice points. We use a time step $\delta t = 0.002\lambda/c$. For these values of the parameters δ and δt the simulation results are very accurate.

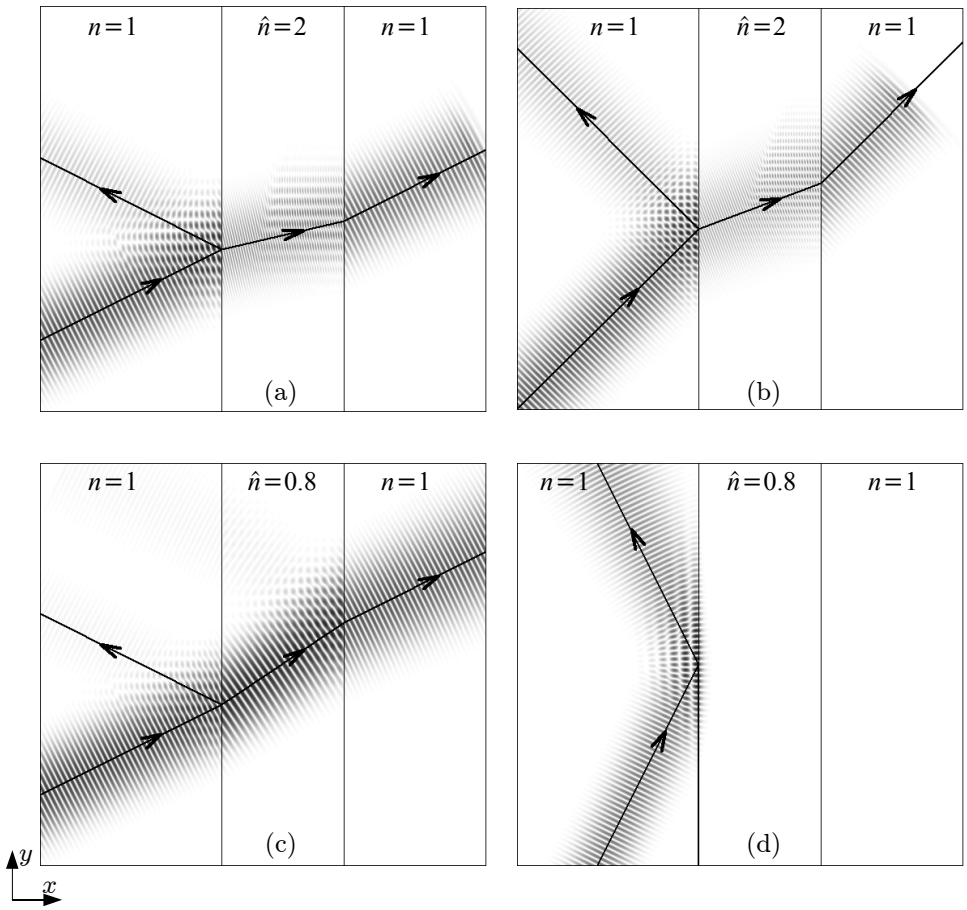

Figure 3.6: FDTD simulation results for the propagation of an electromagnetic wave (TM mode) through a slab. The snapshots are taken at $t = 50\lambda/c$. The arrows indicate the direction of propagation according to Snell's law and the law of reflection. (a): $\hat{n} = 2$, $\theta = 26.57°$; (b): $\hat{n} = 2$, $\theta = 45°$; (c): $\hat{n} = 0.8$, $\theta = 26.57°$; (d): $\hat{n} = 0.8$, $\theta = 63.43°$. For the other simulation parameters we refer to the text.

In front of the slab, we put a line source, modeled by

$$\mathbf{J}(\mathbf{r}, t) = \mathbf{O}\, J(\mathbf{r}) e^{-C_0|\mathbf{r}-\mathbf{r}_0|^2/W^2} \sin(\Omega t), \tag{3.60}$$

where $\mathbf{O}$ defines the direction of the electric (TM mode) or magnetic (TE mode) current and Ω the angular frequency of the line source, $J(\mathbf{r})$ defines the spatial distribution of the intensity and angle of incidence θ, C_0 is a constant, $\mathbf{r}_0$ is the center of the line source and W is the half length of the line source. At $t = 0$, the source starts gradually emitting a TM wave or a TE wave.

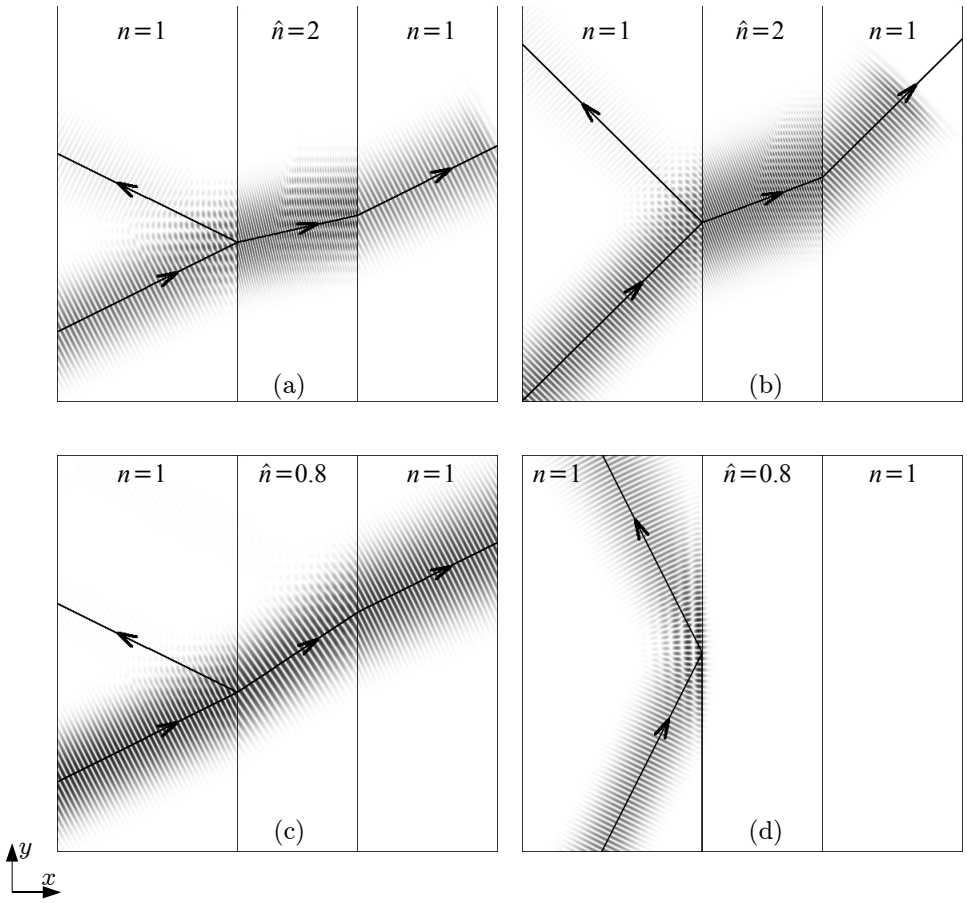

Figure 3.7: Same as Fig. 3.6 but for a TE wave.

Fig. 3.6 shows the simulation results for a TM wave. The parameters for the line source are $C_0 = 5, W = 8\lambda, \mathbf{r}_0 = (10\lambda, 10\lambda), \Omega = 2\pi c/\lambda$. The snapshots show E_z^2 and are taken at $t = 50\lambda/c$. Figs. 3.6a,b depict the results for $\hat{n} = 2, \theta = 26.57°$ and $\hat{n} = 2, \theta = 45°$, respectively. For both examples the propagation of the refracted and reflected wave exactly follows Snell's law and the law of reflection, as indicated by the arrows. Figs. 3.6c,d show simulation results for $\hat{n} = 0.8$. In this case, the incident light will be totally reflected off the interface if the angle of incidence is larger than $\theta_c = 53.13°$. This effect is illustrated in Fig. 3.6d, where $\theta = 63.43°$. If $\theta < \theta_c$, a reflected and a refracted beam exist, just as in the case $n < \hat{n}$. An example is shown in Fig. 3.6c, where $\theta = 26.57°$. From Fig. 3.6c,d it can be concluded that also for the case $\hat{n} < n$, the simulated light propagation exactly follows Snell's law and the law of reflection.

In Fig. 3.7 we show simulation results for a line source emitting a TE wave. The simulation parameters are taken to be exactly the same as the ones used in the simulations to produce the results depicted in Fig. 3.6. As seen from Fig. 3.7, also the propagation of the TE wave exactly follows Snell's law and the law of reflection.

In summary, the simulation results presented in Fig. 3.6 and Fig. 3.7 demonstrate that our FDTD simulation code correctly simulates the propagation of light, generated by a line source, through a homogeneous isotropic slab of material with $\hat{\varepsilon}, \hat{\mu} > 0$.

3.2 Dielectrics with negative permeability and permittivity

3.2.1 Refractive index, phase and group velocity

If $\varepsilon < 0$ and $\mu < 0$, then it follows from Eq. (3.23) that $\mathbf{E}, \mathbf{H}$ and $\mathbf{k}$ form a left-handed set of vectors. According to Eq. (3.25), the Poynting vector $\mathbf{S}$ always forms a right-handed set with the vectors $\mathbf{E}$ and $\mathbf{H}$. Accordingly, $\mathbf{S}$ and $\mathbf{k}$ are antiparallel, that is $\mathbf{S}$ and $\mathbf{k}$ can be written as $\mathbf{S} = S\mathbf{u}$ and $\mathbf{k} = \beta k\mathbf{u}$ with $\beta = -1$, respectively. Hence, $\mathbf{S} \cdot \mathbf{k} < 0$. Since in weakly dispersive media $\mathbf{S} \cdot \mathbf{v}_g > 0$, the sign of $\mathbf{v}_g \cdot \mathbf{k}$ is equivalent to the sign of $\mathbf{S} \cdot \mathbf{k}$, which in this case is negative. The group velocity is called negative, that is having the opposite sign as the wave vector. From Eq. (3.32) it follows that $\partial\omega/\partial k < 0$ and hence $n_g < 0$. Using Eqs. (3.29) and (3.30) with $\beta = -1$ it can be seen that the sign of the refractive index n is the sign of $\mathbf{S}\cdot\mathbf{k}$, and thus also of $\mathbf{v}_g \cdot \mathbf{k}$. Thus, homogeneous isotropic dielectric media with simultaneously negative permeability and permittivity have a negative refractive index. Note that independent of the sign of β, or equivalently independent of the sign of n, $\mathbf{v}_p \cdot \mathbf{k} > 0$, as can be seen from Eqs. (3.30) and (3.34). Therefore, in homogeneous isotropic dielectric media with a negative refractive index, the group velocity is negative (that is having the opposite sign as the wave vector) while the phase velocity is positive (that is having the same sign as the wave vector). A summary of the above findings and a comparison to the ones for the case $\varepsilon > 0, \mu > 0$ is given in Table 3.1.

The consequences of the fact that for media with $\varepsilon < 0$ and $\mu < 0$, the wave vector and the Poynting vector are antiparallel are a reversed Doppler effect [64], a reversed Vavilov-Cerenkov effect [64], negative refraction [64], imaging by a flat lens, the replacement of the radiation pressure characteristic of ordinary substances by a radiation tension or attraction [64], and open cavity formation [3, 17].

In the literature on materials that show negative refraction, there sometimes is confusion about the definition of the refractive index related to the observed negative refraction. Therefore we briefly explain the relation of the phase and group refractive indices n_p and n_g to negative refraction.

Table 3.1: Phase and group velocities and their associated phase and group refractive indices for homogeneous isotropic dielectric materials.

$\varepsilon > 0, \mu > 0$	$\varepsilon < 0, \mu < 0$
$\mathbf{S} \cdot \mathbf{k} > 0$	$\mathbf{S} \cdot \mathbf{k} < 0$
$\mathbf{S} \cdot \mathbf{v}_g > 0$	$\mathbf{S} \cdot \mathbf{v}_g > 0$
$\mathbf{v}_g \cdot \mathbf{k} > 0$	$\mathbf{v}_g \cdot \mathbf{k} < 0$
$n_p = n > 0$	$n_p = n < 0$
$n_g > 0$	$n_g < 0$
$\mathbf{v}_p \cdot \mathbf{k} > 0$	$\mathbf{v}_p \cdot \mathbf{k} > 0$

Negative refraction of a wave propagating from one medium to another is said to be observed when the wave in the second medium appears at the same side of the normal to the interface as in the first medium. As described above, in a homogeneous isotropic dielectric medium with normal dispersion, negative refraction occurs when the (phase) refractive index is negative. It was also shown that $n_g < 0$ when $n_p < 0$. However, note that because in this case the group velocity corresponds to the energy velocity, which is less than c, $|n_g|$ has to be larger than one.

Negative refraction can for example also be observed in anisotropic dispersive media. For anisotropic dispersion cases, $\mathbf{v}_g$ and $\mathbf{k}$ are not along the same direction. In that case the sign of n_g is chosen to manifest the sign of refraction at the interface and therefore n_g has the sign of $(\mathbf{v}_g \cdot \mathbf{k})_x$, where x denotes the direction along the interface and $\mathbf{k}$ the incident wave vector [65]. It can be seen that $(\mathbf{v}_g \cdot \mathbf{k})_x < 0$, while $(\mathbf{v}_g \cdot \mathbf{k}) > 0$ and thus $n_p > 0$. All possible combinations of signs for the phase and group refractive indices are possible [65].

In the case of normal dispersion $n_p = n$ can be used in Snell's law to determine the propagation angle of the wave [65], also if $n < 0$ (see Section 3.2.3). However, n_g cannot be used in Snell's formula to obtain the propagation direction of the wave [65]. If negatively appearing refraction is observed, it should be carefully checked whether it is caused by a negative refractive index of an isotropic dielectric medium or that it is due to anisotropy of the medium (see for example [66]).

3.2.2 History and terminology

The first theoretical study of wave propagation in materials for which ε and μ are simultaneously negative has often been attributed to Veselago, who published his work in 1967 [64] (Translation from the original Russian version in Usp. Fiz. .Nauk. 92, 517 (1967). This year was mislabeled in the translation as 1964). Because for media with $\varepsilon < 0$ and $\mu < 0$ the vectors $\mathbf{E}, \mathbf{H}$ and $\mathbf{k}$ form a left-handed set of vectors, Veselago referred to these materials

as left-handed materials. The conventional lossless dielectric media with $\varepsilon > 0$, $\mu > 0$, he named right-handed materials. Unfortunately, these names are not well-chosen. The left or right handedness also refers to the molecular structure of chiral materials that are often studied in electromagnetics research [67]. Therefore several other names are used in the literature. We only mention the most common ones.

Since for a plane wave in a homogeneous isotropic medium with $\varepsilon < 0$ and $\mu < 0$, the Poynting vector and wave vector are antiparallel (see Section 3.2.1). Lindell *et al.* [68, 69] suggested the name backward-wave media. They were however not the first to use this name. Already at the end of the fifties and the beginning of the sixties backward waves were known to exist in some periodic structures with applications to microwave amplifiers, oscillators and antennas [70–73]. Backward-waves have also been generated in continuous structures like a sheet of plasma [74]. However, as mentioned on the website of Moroz [61], Lamb and Schuster in 1904 may even have been the first to study the possibility of a negative group velocity, that is having the opposite sign to the wave vector, and thus to study the existence of backward-waves. Lamb studied mechanical systems, free from dissipation, in which the group velocity can become negative [62]. In his paper, Lamb mentioned that Schuster proposed to him the possibility of a negative group velocity and that Schuster pointed out that the optical formulae relating to anomalous dispersion indicate a negative group velocity for certain portions of the spectrum lying within the regions of special absorption. Also Pocklington mentioned in 1905 waves propagating toward the source of disturbance in a mechanical system [75]. Another name to media with $\varepsilon < 0$ and $\mu < 0$ was given by Ziolkowski *et al.* [76, 77], who denoted these media as double negative materials. On the other hand, media with both positive permittivity and permeability they denoted as double positive media. Since homogeneous isotropic dielectric media with $\varepsilon < 0$ and $\mu < 0$ have a negative refractive index (see Section 3.2.1), these materials are also often called negative index materials (see for example [78–80]). Materials with a positive refractive index are then called positive index materials.

Renewed interest to the negative index materials after Veselago's proposal in 1967 is usually attributed to Pendry who in 2000 pointed out that negative refraction makes a perfect lens [81]. Recently, a lot of experimental efforts are put in finding materials that have a negative refractive index. In this respect it is also worthwhile to mention the work by Silin on the possibility of creating plane-parallel lenses, which appeared in 1978 [82]. With his paper, Silin wanted to draw attention to the possibility of creating new type of optical elements using media with unusual dispersion laws and to stimulate the search for media with unusual dispersion laws. Silin also refers to the theoretical and experimental investigation of the law of refraction for media with negative dispersion by Mandelshtam in the late forties [83, 84]. In 1972, Silin also published an article on artificial dielectrics [85]. Artificial dielectrics have complicated dispersion characteristics. They are encountered in media in the form of periodic structures of metal or dielectric bundles and they were widely used in superhigh-frequency

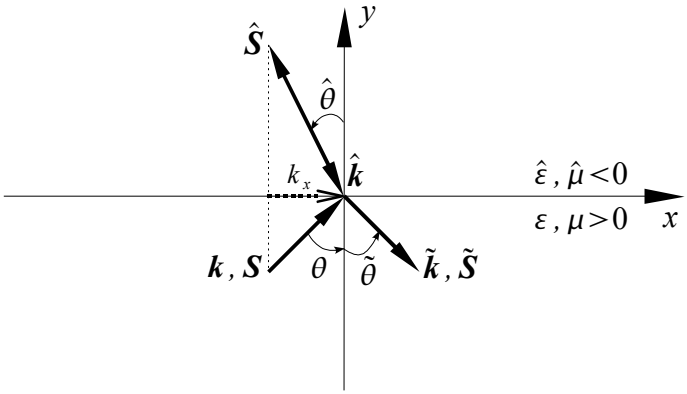

Figure 3.8: Reflection and refraction of a plane wave at an interface between two different media characterized by $\varepsilon, \mu > 0$ and $\hat{\varepsilon}, \hat{\mu} < 0$, respectively. $\mathbf{k}$ and $\mathbf{S}$ are the wave vector and Poynting vector of the incident wave, $\tilde{\mathbf{k}}$ and $\tilde{\mathbf{S}}$ are the wave vector and Poynting vector of the reflected wave and $\hat{\mathbf{k}}$ and $\hat{\mathbf{S}}$ are the wave vector and Poynting vector of the refracted wave. θ, $\tilde{\theta}$ and $\hat{\theta}$ correspond to the angle of incidence, the angle of reflection and the angle of refraction, respectively. The angles are measured in a counterclockwise or positive direction.

engineering [82]. In the late seventies no suitable isotropic media with negative refraction were known in the optical range [82]. The current revival of interest in the properties of wave propagation in a medium with negative refractive index appears thus almost thirty years after the work of Silin [85], who already explained optical properties in artificial dielectrics in terms of equifrequency surfaces, as mentioned on the website of Moroz [61].

3.2.3 Reflection and refraction at an interface between a positive and a negative index material

We follow the same procedure as described in Section 3.1.5 to study the propagation of a plane wave with wave vector $\mathbf{k}$ and frequency ω falling on to an interface between a homogeneous isotropic medium with optical properties $\varepsilon > 0, \mu > 0$ and a homogeneous isotropic medium with optical properties $\hat{\varepsilon} < 0, \hat{\mu} < 0$. At the boundary the wave is split. The reflected and refracted plane waves have wave vectors and frequencies $\tilde{\mathbf{k}}, \tilde{\omega}$ and $\hat{\mathbf{k}}, \hat{\omega}$, respectively. As discussed in Section 3.1.5, the tangential component of the incident wave vector is conserved upon reflection and refraction. This is independent from the sign of $\hat{\varepsilon}$ and $\hat{\mu}$, whether they are both positive or negative. From Eq. (3.38) it follows that if $\varepsilon > 0, \mu > 0$ and $\hat{\varepsilon} < 0, \hat{\mu} < 0$, then $\mathbf{S} \cdot \mathbf{k} > 0, \tilde{\mathbf{S}} \cdot \tilde{\mathbf{k}} > 0$ and $\hat{\mathbf{S}} \cdot \hat{\mathbf{k}} < 0$. Note that because $\hat{\mathbf{S}} \cdot \hat{\mathbf{k}} < 0$ also $\hat{n} < 0$ (see Table 3.1). Since, if the incident wave hits the boundary, the energy flux of the reflected and refracted wave is such that the energy flows away from the interface, the incident, reflected and refracted waves propagate as indicated in Fig. 3.8. As can be seen from Fig. 3.8, the refracted and the incident beam are positioned at the same side of the normal to the interface

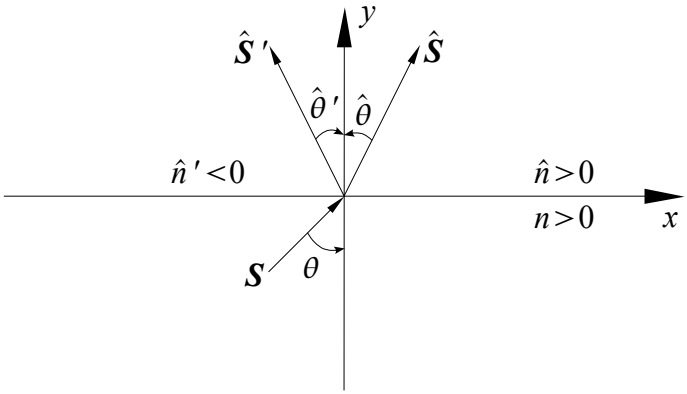

Figure 3.9: Schematic picture of the refraction of a plane wave for the case $\hat{n} > 0$ and $\hat{n}' < 0$, as it often appears in the literature (see for example[64]) $\hat{\theta}$ and $\hat{\theta}'$ denote the angles of refraction for the case $\hat{n} > 0$ and $\hat{n}' < 0$, respectively. The angles are measured in a counterclockwise or positive direction and hence Note that $\hat{\theta}' < 0$.

if $n > 0$ and $\hat{n} < 0$.

If we define the angles $0 \leq \theta, \tilde{\theta}, \hat{\theta} \leq \pi/2$ as indicated in Fig. 3.8, we have

$$k_x = k\cos(\frac{\pi}{2} - \theta) = k\sin\theta, \tag{3.61a}$$

$$k_y = k\sin(\frac{\pi}{2} - \theta) = k\cos\theta, \tag{3.61b}$$

$$\tilde{k}_x = \tilde{k}\cos(\frac{3\pi}{2} + \tilde{\theta}) = \tilde{k}\sin\tilde{\theta}, \tag{3.61c}$$

$$\tilde{k}_y = \tilde{k}\sin(\frac{3\pi}{2} + \tilde{\theta}) = -\tilde{k}\cos\tilde{\theta}, \tag{3.61d}$$

$$\hat{k}_x = \hat{k}\cos(\frac{3\pi}{2} + \hat{\theta}) = \hat{k}\sin\hat{\theta}, \tag{3.61e}$$

$$\hat{k}_y = \hat{k}\sin(\frac{3\pi}{2} + \hat{\theta}) = -\hat{k}\cos\hat{\theta}. \tag{3.61f}$$

From Eqs. (3.37) and (3.61) it follows that

$$\tilde{\theta} = \theta \tag{3.62}$$

and

$$\frac{\sin\theta}{\sin\hat{\theta}} = \frac{\hat{k}}{k} = \frac{|\hat{n}|}{|n|} = \frac{\hat{n}}{\hat{\beta}}\frac{\beta}{n}, \tag{3.63}$$

where use have been made of

$$\tilde{k} = k = \frac{|n|\omega}{c}, \quad \text{and} \quad \hat{k} = \frac{|\hat{n}|\omega}{c}. \tag{3.64}$$

Note that in Eq. (3.63) $n > 0, \beta = +1$ and $\hat{n} < 0, \hat{\beta} = -1$. The ratios in Eq. (3.63) should be positive, since a ratio of two vector lengths is involved and vector lengths are by definition positive. However, in the literature it is often mentioned that Snell's law

$$\frac{\sin\theta}{\sin\hat{\theta}} = \frac{\hat{n}}{n}, \tag{3.65}$$

can still be used if the observed refracted beam lies on the same side of the normal to the interface as the incident beam does and that in that case a negative refractive index is found for the medium ($\hat{n} < 0$ while $n > 0$). In that case, however it is assumed that the angle of refraction is equal to minus the refraction angle for the case of normal refraction, as indicated in Fig. 3.9 (see also [64]). As a result $\hat{\theta} < 0, 0 < |\hat{\theta}| \leq \pi/2$ and Eq. (3.63) can be rewritten as

$$\frac{\sin\theta}{\sin\hat{\theta}} = -\frac{\hat{k}}{k} = -\frac{|\hat{n}|}{|n|} = -\frac{\hat{n}}{\hat{\beta}}\frac{\beta}{n} = \frac{\hat{n}}{n}, \tag{3.66}$$

with $\hat{n} < 0$ and $n > 0$.

The amplitudes of the reflected and refracted waves can be found using the expressions (3.50), (3.52), (3.48) and (3.53) derived in Section 3.1.5. For the case that $\hat{\varepsilon} = -\varepsilon$ and $\hat{\mu} = -\mu$, there is no reflection at the interface. The angle of refraction is equal to the angle of incidence and the refracted beam is positioned at the same side of the normal to the interface as the incident beam is. Note that if $|\hat{n}| < |n|$, the phenomenon of total internal reflection (see Section 3.1.6) can still be observed. This phenomenon occurs independent of the sign of $\hat{n}$.

3.2.4 Subwavelength imaging

One of the interesting properties of negative index materials is their ability to focus light. Conventional lenses are convex. They have a converging effect on light rays. The resolution of a conventional (convex) lens is always limited by the wavelength of the light. A light beam cannot be focused to a spot with a diameter smaller than half of the wavelength of the light. In 1967, Veselago has shown theoretically that a convex lens made of a negative index material would be diverging light and that a concave lens made of negative index material would be converging light [64]. This behavior is thus opposite to the behavior observed for convex and concave lenses made of positive index materials. Veselago also noted that a flat plate of thickness D made of negative index material with $\hat{n} = -1$ and situated in vacuum can focus radiation from a point source P positioned at a distance $L < D$ from one side of the plate to a point P' located at a distance $D - L$ from the other side of the plate (see Fig. 3.10) [64]. As can be seen from Fig. 3.10, also an image inside the slab is formed. However, as Veselago has remarked, the flat plate, unlike a conventional lens, will not focus at a point a beam of rays coming from infinity [64].

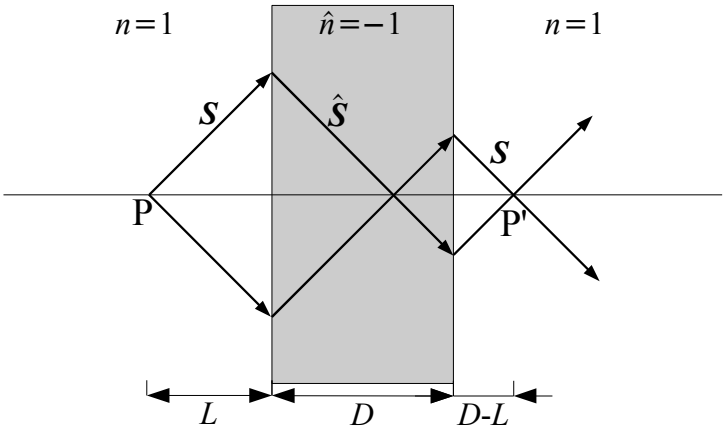

Figure 3.10: Imaging by a flat slab of thickness D of negative index material with $\hat{n} = -1$ and surrounded by vacuum. A point source P is positioned at a distance L from the left surface of the slab. A "perfect" image of the source can be observed in the point P', located at a distance $D - L$ from the right surface of the slab.

In 1978, Silin showed that plane-parallel lenses can be constructed on the basis of media with negative dispersion [82]. He demonstrated that it is possible to choose an isotropic medium such that monochromatic aberrations can be eliminated for such lenses [82]. In 2000, Pendry further pointed out that flat slabs of negative index material with $\hat{n} = -1$ and surrounded by vacuum make perfect lenses or superlenses, since both propagating and evanescent waves contribute to the resolution of the image [81]. These lenses are thus predicted to have subwavelength resolution. Because Pendry also demonstrated by means of simulations that such a lens operating at the frequency of visible light can be physically realized in the form of a thin slab of silver, a lot of research has been performed on negative index materials and superlenses since 2000. However, limitations of the superlensing effect have also been subject of debate [86–92]. In 2001, Ziolkowski *et al.* have shown analytically that the perfect lens effect exists only for a negative index material with $\varepsilon = \mu = -1$ that is both lossless and nondispersive [76]. The perfect lens effect was shown not to exist for any realistic dispersive, lossy negative index material. The simulation results of Loschialpo *et al.* [93, 94] do not support a perfect lens, as postulated by Pendry [81], either.

3.2.5 Physical realization of negative index materials

The search for media with a negative refractive index has led to the fabrication of the so-called metamaterials [78, 95, 96]. Metamaterials are artificial materials that consist of a collection of repeated objects whose size and spacing are much smaller than the electromagnetic wavelength of interest. As such the inhomogeneous composite can be described by a homogeneous material with effective material properties ε_{eff} and μ_{eff} [78, 95, 96]. The

properties of the complex material can thus be summarized by an effective permittivity and permeability, which is a great simplification.

Negative permittivities can be obtained in cut-wire media [97, 98]. In 1999, a variety of structures was proposed that could form magnetic metamaterials [99]. Those structures, split-ring resonators, consisting of loops or tubes of conductor with a gap inserted, can lead to a negative permeability. Soon after the introduction of the split-ring resonator media by Pendry in 1999 [99], composite wire and split ring resonator structures were fabricated for which a negative $\varepsilon_{\mathrm{eff}}$ and μ_{eff} was predicted for a frequency region in the microwave regime [100, 101]. The first experiment, showing negative refraction in a prism of metamaterial designed to have a negative effective refractive index n_{eff} in the microwave frequency regime, was performed in 2001 by Shelby *et al.* [102].

Because the physical realization of materials with a negative refractive index remained questioned [53, 103], in 2003 Houck *et al.* produced new experimental evidence showing that transmission through a metamaterial wedge sample, similar to the one in the first demonstration, is in accordance to Snell's law with a negative refractive index [104]. In addition, the experiment gave preliminary evidence for the focusing properties of a flat slab of negative index material. In the same year, results of Snell's law experiment on a negative index metamaterial wedge were reported [105]. In contrast to the two previous experiments, in which two-dimensional composite wire and split ring resonator structures were used, in this experiment a one-dimensional negative index material structure was used. Also this experiment supported the observation reported by Shelby *et al.* [102]. Recently, measurements on flat slabs of composite wire and split ring resonator negative index materials have been presented that show focusing inside and outside the metamaterial [80]. Additionally, a linear dependence of the focal length on the frequency was demonstrated [80]. However, focusing with subwavelength resolution using such a composite wire split ring resonator lens remained experimentally elusive [80]. Although, results have been reported that a planar negative index transmission-line-lens can form images that overcome the diffraction limit [106]. Recently, Pendry proposed chiral materials as an alternative to produce negative index materials [107].

A second approach to construct negative index metamaterials is based on the concept of transmission line structures, which are common in electrical engineering applications. This approach has been described by Eleftheriades *et al.* in 2002 [108]. The transmission-line structures consist of two-dimensional transmission-line (TL) grids loaded with series capacitors (C) and shunt inductors (L) [108]. Using this L-C loaded TL approach, negative refraction [108] and focusing was demonstrated at microwave frequencies [108, 109]. Radiating versions of these media have been used to experimentally demonstrate backward-wave radiation in free space, a characteristic analogue to reversed Cherenkov radiation [110]. The focusing reported in [108, 109] was obtained by lenses utilizing a single interface between a left-handed medium and a homogeneous dielectric. Imaging beyond the diffraction limit

could not clearly be observed with these lenses. Subsequently, planar slabs (having two interfaces) of L-C loaded TL left-handed media were shown theoretically to enhance the amplitudes of evanescent waves [111, 112] and to focus propagation waves with subwavelength resolution [112]. In a later study, these theoretical findings were confirmed experimentally [106].

A third approach to obtain the phenomena of negative refraction and imaging by a planar surface is to use photonic crystals. In contrast to the metamaterials described above, photonic crystals are periodic structures typically composed of insulators. Therefore they can exhibit low losses, even at the higher (optical) frequencies, a property that can be important in applications. In photonic crystals, the size and spacing of the scattering elements are on the order of the electromagnetic wavelength of interest. Therefore a photonic crystal cannot be regarded as a homogeneous medium and its properties cannot be described by an effective permittivity and permeability. Nevertheless, in 2000 Notomi has shown theoretically that photonic crystals near the band gap frequency behave as if they have an effective refractive index [3]. For some frequency regions this effective refractive index can be negative [3]. As a result in these frequency regions, photonic crystals can exhibit the same phenomena as observed in negative index materials, including negative refraction and imaging by a planar surface [3, 17]. In 2003, negative refraction was experimentally observed in a two-dimensional photonic crystal operating in the microwave regime [113–115]. Also subwavelength imaging has been demonstrated in 2003 [114, 115]. More experimental evidence of negative refraction [116–118] and subwavelength imaging [118–124] in photonic crystals followed rapidly. Note that the experimentally observed negative refraction and subwavelength imaging is not always due to a negative effective refractive index, but due to anisotropy. This is the case for the negative refraction observed in [113–115, 123]. Moreover, all this theoretical and experimental evidence for negative refraction and subwavelength imaging is for two-dimensional photonic crystals. Although these two-dimensional crystals are very important for the investigation of negative refraction and flat lenses with subwavelength resolution, the realization of such lenses in three dimensions is of significant importance for many applications. Luo *et al.* [125] and Ao *et al.* [126] proposed and theoretically investigated such lenses, made of three-dimensional photonic crystals with BCC lattice symmetry. In 2005, Lu *et al.* [127] have experimentally demonstrated for the first time subwavelength resolution imaging at microwave frequencies by a three-dimensional photonic crystal flat lens. The photonic crystal is a BCC structure similar to the one proposed by Luo *et al.* [125].

In [66], Ye questions whether the current evidence for negative index materials and the related negative refraction is sufficient or conclusive, without criticizing the experimental evidence and theoretical analysis. Ye's conclusion is that the current experimental evidence is not sufficient to conclude that negative index materials have been fabricated and that a detailed exploration has to be carried out with regard to all aspects of negative refraction [66].

As discussed above, metamaterials and photonic crystals have shown negative refraction and subwavelength imaging at microwave and infrared frequencies. As discussed by Pendry [81], silver is a candidate for optical superlensing. Recently, Zhang *et al.* have demonstrated optical imaging with a silver superlens [128]. They showed sub-diffraction limited imaging with a resolution of one-sixth of the illumination wavelength (ultraviolet light at a 365 nm wavelength). This achievement is a result of their profound theoretical and experimental studies of the regeneration of evanescent waves by a silver film [129–131].

3.3 Photonic crystals

3.3.1 Realization

Photonic crystals are made of periodically modulated dielectric materials with a periodicity of the order of the wavelength of the electromagnetic wave. The resultant photonic dispersion exhibits a band nature analogous to the electronic band structure in a solid. When passing through photonic crystals, the propagation of electromagnetic waves can be significantly affected by the photonic crystals in the same way as the electrons are controlled by the crystals. Since their discovery in 1987 [4, 132], photonic crystals received a rapidly growing attention. The idea of controlling the light by means of photonic crystals has lead to many proposals for novel devices [2, 7–12].

Considerable efforts have been made to find photonic crystals that can completely block propagation of electromagnetic waves in all directions and for all polarizations within a certain frequency range, known as the photonic band gap. In the last two decades several three-dimensional photonic crystal architectures have been proposed and/or produced for this purpose. Among them are the criss-crossing pore structures (inverse diamond lattice of overlapping air spheres in a high dielectric background) [4, 133], slanted-pore structures [134], the woodpile structures [135, 136], inverse opal structures [137, 138], circular spiral structures [139], structures from woven dielectric fibers [140], square spiral structures [141–143], self-assemblies of metal nanospheres [144, 145], and bicontinuous and multicontinuous cubic microstructures [146–151]. The nanofabrication technology needed for their realization at optical and near infrared frequencies include angle etching [152–154], colloidal precipitation [155, 156], photopolymerization [157–159], layer-by-layer [135, 160–165], and microassembly [166, 167] methods. An overview of the methods employed to obtain one-, two-, and three-dimensional photonic crystals mainly functioning in the optical range, is for example given in [12].

3.3.2 Negative effective refractive index

Photonic crystals are not only of interest for applications related to their photonic band gap or to the possibility to localize modes around defects in the photonic crystal lattice. They also show other intriguing optical phenomena, such as superprism, negative refraction or ultrarefractive phenomena [3, 5, 6, 17, 168, 169]. The dielectric properties of photonic crystals, which are composite systems of constituents with different optical properties, are inhomogeneous. However, Notomi has shown that near the photonic band gap frequency, photonic crystals behave as if they have a certain effective refractive index which is not limited by the refractive index of the constituents but is determined by the photonic band structure [3, 17]. The effective refractive index can be smaller than one and can also be negative without absorption [3, 17]. As a result photonic crystals can be used to realize artificial dielectric materials having a negative refractive index.

The occurrence of negative refraction due to a negative index in two-dimensional photonic crystals consisting of dielectric rods arranged in a triangular lattice has been demonstrated by various numerical simulations [3, 17, 65, 79, 170] and has also been experimentally verified in the microwave regime [116]. The latter experiment has been criticized by Ye [66] since the authors did not verify the isotropy before applying Snell's law. Moreover, the simulation results presented in Fig. 3 of [116], that are said to be in good agreement with the experimental results, show that inside the prism the light beam is not propagating along a straight line as expected for an (effective) isotropic medium. Experimental and theoretical evidence for focusing in a two-dimensional photonic crystal consisting of a triangular lattice of alumina rods in air is given in [120, 121, 124]. Focusing in a two-dimensional photonic crystal consisting of a triangular lattice of air holes drilled in a dielectric slab has also been numerically demonstrated and analyzed in detail [171–175] and observed experimentally for wavelengths in the infrared [119] and microwave [118] regime. However, the simulation results in [171] do not show focusing of the light inside the photonic crystal slab, as required for a negative index lens. Apart from negative refraction and imaging by a flat lens, another phenomenon relying on the concept of a negative refractive index has been simulated using photonic crystals with triangular lattice symmetry, namely open cavity formation [176–178].

It has also been shown theoretically that several photonic configurations consisting of air holes or dielectric rods in a square lattice can exhibit similar optical phenomena as the ones predicted for negative index materials, including negative refraction and imaging by a planar interface [179] and backward Cerenkov radiation [180], although the refraction index is anisotropic and positive. However, the latter type of imaging has been subject of debate. Li and Lin concluded that in this case the imaging properties are dominantly governed by the self-collimation effect and complex near-field scattering effects and not by the all-angle negative-refraction [181]. On the other hand it was shown by He *et al.* [182] that the negative refraction gives an important contribution to the focusing properties. They found that the

self-collimation effect occurs for small angles of incidence whereas the negative refraction effect occurs for relatively large angles of incidence [182]. As well in [181] as in [182] it was demonstrated that in the photonic crystals with square lattice symmetry no flat slab lensing, as described in Section 3.2.4 occurs. Namely, the slab-image distance dependency on the slab thickness is not observed [181, 182]. Furthermore, no focusing of the light inside the photonic crystal slab was found [181]. Based on an extensive simulation study Ye and co-workers concluded that the imaging properties are due to guided or collimated wave transmission caused by the presence of a partial band gap and not by negative refraction [66, 183–187].

The focusing of light with two-dimensional photonic crystals consisting of rods arranged in a square lattice has been demonstrated experimentally operating in the microwave regime [113–115]. However, Kuo and Ye found that the focusing reported in [115] is due to anisotropic scattering of the array of rods [66, 188]. Also the experiment of Cubukcu *et al.* [114] has been criticized [66] since the medium is not isotropic and then Snell's law cannot be applied. Moreover, recently it has been shown that the so-called images of two point sources in [114], that are separated by a distance of $\lambda/3$, are due to the anisotropic scattering in the photonic crystal slab and due to the concentration of light in two of the rods at the exit interface [189]. The intensity distribution in a detection plane, placed close to the exit surface of the photonic crystal slab, depends on the light distribution concentrated in the cylinders at the exit surface [189]. As a result, "imaging" disappears if the distance between the sources is varied and if the sources are placed further away from the photonic crystal slab [189]. In both cases a larger number of cylinders light up at the exit plane and no images can be observed in the detection plane.

Recently, three-dimensional subwavelength imaging by a photonic-crystal flat lens using negative refraction at microwave frequencies has been demonstrated experimentally [127], a few years after the theoretical proposal of such lenses in [125, 126]. The photonic crystal used in the experiment is a BCC structure, similar as the one proposed by Luo *et al.* [125]. Within a certain frequency, negative refraction due to a negative effective refraction index, can be observed in this three-dimensional photonic crystal. In the experiment, imaging of a point source is demonstrated in both amplitude and phase [125]. Further validation of the subwavelength imaging is given by the imaging of two pinhole sources with subwavelength spacing as two resolvable spots.

3.3.3 Bloch waves

In the rest of this and the following chapters, we consider two-dimensional photonic crystals. The photonic crystal structure consists of a two-dimensional lattice of either dielectric cylinders with permittivity ε embedded in air or air holes embedded in a dielectric medium with permittivity ε. The dielectric materials are assumed to be non-magnetic and therefore

$\mu = 1$. We only consider square and triangular lattices. We denote the primitive vector of the direct lattice by $\mathbf{a}_1$ and $\mathbf{a}_2$ and the primitive vector of the reciprocal lattice by $\mathbf{b}_1$ and $\mathbf{b}_2$ (see Appendix A).

Since the permittivity is a periodic function following the same periodicity as the photonic crystal lattice,

$$\varepsilon(\mathbf{r} + \mathbf{R}) = \varepsilon(\mathbf{r}), \tag{3.67}$$

for all $\mathbf{R}$ in the Bravais lattice, we can write

$$\varepsilon(\mathbf{r}) = \sum_{\mathbf{K}} \tilde{\varepsilon}(\mathbf{K}) e^{i\mathbf{K}\cdot\mathbf{r}}, \tag{3.68}$$

where $\tilde{\varepsilon}(\mathbf{K})$ are the Fourier coefficients of the function $\varepsilon(\mathbf{r})$ and $\mathbf{K}$ are the reciprocal lattice vectors.

Using the notation

$$\mathbf{K} = l\mathbf{b}_1 + m\mathbf{b}_2 \equiv \mathbf{K}_{l,m}, \tag{3.69}$$

Eq. (3.68) can be rewritten as

$$\varepsilon(\mathbf{r}) = \sum_{l,m} \tilde{\varepsilon}(\mathbf{K}_{l,m}) e^{i\mathbf{K}_{l,m}\cdot\mathbf{r}}. \tag{3.70}$$

For later use, we define

$$\varepsilon(\mathbf{r})^{-1} = \sum_{l,m} \hat{\varepsilon}(\mathbf{K}_{l,m}) e^{i\mathbf{K}_{l,m}\cdot\mathbf{r}}, \tag{3.71}$$

since the inverse of a periodic function is periodic itself. Here $\hat{\varepsilon}(\mathbf{K}_{l,m})$ denote the Fourier coefficients of the function $\varepsilon(\mathbf{r})^{-1}$.

The electromagnetic wave that propagates in a photonic crystal is a Bloch wave. A Bloch wave can be written as

$$\mathbf{V}(\mathbf{r}, t) = e^{-i(\omega_{n,\mathbf{k}} - \mathbf{k}\cdot\mathbf{r})} \mathbf{u}_{n,\mathbf{k}}(\mathbf{r}), \tag{3.72}$$

where $\mathbf{k}$ is the wave vector of the Bloch wave, $\omega_{n,\mathbf{k}}$ denotes the frequency in band n corresponding to $\mathbf{k}$ (see below for an explanation of the band index n) and $\mathbf{u}_{n,\mathbf{k}}(\mathbf{r})$ is a periodic function having the same periodicity as the photonic crystal lattice:

$$\mathbf{u}_{n,\mathbf{k}}(\mathbf{r} + \mathbf{R}) = \mathbf{u}_{n,\mathbf{k}}(\mathbf{r}), \tag{3.73}$$

for all $\mathbf{R}$ in the Bravais lattice. From Eq. (3.72) and Eq. (3.73) it follows that

$$\mathbf{V}(\mathbf{r} + \mathbf{R}, t) = e^{i\mathbf{K}\cdot\mathbf{R}} \mathbf{V}(\mathbf{r}, t). \tag{3.74}$$

Since a periodic function can always be expanded as a Fourier series, we can write

$$\mathbf{u}_{n,\mathbf{k}}(\mathbf{r}) = \sum_{l,m} \tilde{\mathbf{u}}_{n,\mathbf{k}}(\mathbf{K}_{l,m}) e^{i\mathbf{K}_{l,m}\cdot\mathbf{r}}, \tag{3.75}$$

where $\tilde{\mathbf{u}}_{n,\mathbf{k}}(\mathbf{K}_{l,m})$ are the Fourier coefficients of $\mathbf{u}_{n,\mathbf{k}}(\mathbf{r})$. Substituting Eq. (3.75) in the Bloch theorem, Eq. (3.72), gives

$$\mathbf{V}(\mathbf{r},t) = \sum_{l,m} \tilde{\mathbf{u}}_{n,\mathbf{k}}(\mathbf{K}_{l,m}) e^{-i(\omega_{n,\mathbf{k}}t - \mathbf{k}_{l,m}\cdot\mathbf{r})}, \tag{3.76}$$

where we used the notation

$$\mathbf{k}_{l,m} \equiv \mathbf{k} + \mathbf{K}_{l,m}. \tag{3.77}$$

Expression (3.76) holds for the field vector $\mathbf{E}$ and $\mathbf{H}$. Hence, we can write

$$\mathbf{E}(\mathbf{r},t) = \sum_{l,m} \tilde{\mathbf{E}}_{n,\mathbf{k}}(\mathbf{K}_{l,m}) e^{-i(\omega_{n,\mathbf{k}}t - \mathbf{k}_{l,m}\cdot\mathbf{r})}, \tag{3.78a}$$

$$\mathbf{H}(\mathbf{r},t) = \sum_{l,m} \tilde{\mathbf{H}}_{n,\mathbf{k}}(\mathbf{K}_{l,m}) e^{-i(\omega_{n,\mathbf{k}}t - \mathbf{k}_{l,m}\cdot\mathbf{r})}. \tag{3.78b}$$

3.3.4 Photonic band structure diagram

Substituting Eq. (3.78) with $\mu = 1$ and $\mathbf{M}(t) = 0$ in Eq. (2.4a) gives

$$\sum_{l,m} [\mathbf{k}_{l,m} \times \tilde{\mathbf{E}}_{n,\mathbf{k}}(\mathbf{K}_{l,m}) - \omega_{n,\mathbf{k}} \tilde{\mathbf{H}}_{n,\mathbf{k}}(\mathbf{K}_{l,m})] e^{-i(\omega_{n,\mathbf{k}}t - \mathbf{k}_{l,m}\cdot\mathbf{r})} = 0. \tag{3.79}$$

Since the plane waves satisfying the boundary condition

$$\mathbf{V}(\mathbf{r} + \mathbf{R}, t) = \mathbf{V}(\mathbf{r}, t), \tag{3.80}$$

with $\mathbf{R}$ a general Bravais lattice vector, are an orthogonal set, the coefficient of each separate term in Eq. (3.79) must vanish, and therefore for all allowed wave vectors $\mathbf{k}_{l,m}$

$$\tilde{\mathbf{H}}_{n,\mathbf{k}}(\mathbf{K}_{l,m}) = \frac{1}{\omega_{n,\mathbf{k}}} \mathbf{k}_{l,m} \times \tilde{\mathbf{E}}_{n,\mathbf{k}}(\mathbf{K}_{l,m}). \tag{3.81}$$

Substituting Eq. (3.71) and Eq. (3.78) with $\mathbf{J}(t) = 0$ in Eq. (2.4b) gives another relation between the Fourier coefficients of the fields

$$\tilde{\mathbf{E}}_{n,\mathbf{k}}(\mathbf{K}_{l,m}) = -\frac{1}{\omega} \sum_{l',m'} \hat{\varepsilon}(\mathbf{K}_{l-l',m-m'}) \mathbf{k}_{l',m'} \times \tilde{\mathbf{H}}_{n,\mathbf{k}}(\mathbf{K}_{l',m'}). \tag{3.82}$$

As seen in Chapter 2, in two-dimensional the time-dependent Maxwell equations separate into two sets of equations, one set for the TM polarization and one set for the TE polarization. For the TM mode we have

$$\tilde{\mathbf{H}}_{\mathbf{k},n} = (\tilde{H}^x_{\mathbf{k},n}, \tilde{H}^y_{\mathbf{k},n}0), \quad \tilde{\mathbf{E}}_{\mathbf{k},n} = (0, 0, \tilde{E}^z_{\mathbf{k},n}). \tag{3.83}$$

Since in two-dimensional

$$\mathbf{k}_{l,m} = (k^x_{l,m}, k^y_{l,m}, 0), \tag{3.84}$$

we also have

$$\mathbf{k}_{l,m} \cdot \tilde{\mathbf{E}}_{\mathbf{k},n} = 0. \tag{3.85}$$

Substituting Eq. (3.81) in Eq. (3.82) and making use of Eq. (3.83) and Eq. (3.85) leads to

$$\omega^2_{n,\mathbf{k}} \tilde{E}^z_{\mathbf{k},n}(\mathbf{K}_{l,m}) = \sum_{l',m'} \hat{\varepsilon}(\mathbf{K}_{l-l',m-m'}) \left|\mathbf{k}_{l',m'}\right|^2 \tilde{E}^z_{\mathbf{k},n}(\mathbf{K}_{l',m'}). \tag{3.86}$$

The (infinitely many) different solutions to Eq. (3.86) for a given $\mathbf{k}$ are labeled with the band index n. For $|l|, |m| \leq N$, with N an arbitrarily large integer, Eq. (3.86) is the standard eigenvalue expansion used in the plane wave expansion method to compute the photonic band structure diagram of TM polarized waves in two-dimensional photonic crystals [2, 18, 190]. The wave vector $\mathbf{k}$ can be chosen to be in the first Brillouin zone, but this is not required. A wave vector $\mathbf{k}$ that does not lie in the first Brillouin zone can be written as $\mathbf{k} = \mathbf{k}' - \mathbf{K}$ where $\mathbf{k}'$ lies in the first Brillouin zone (see Appendix A). If we draw the dispersion curve for all possible $\mathbf{k}$ vectors, then we use a representation known as the extended-zone scheme [191]. If we specify all the frequencies by a wave vector $\mathbf{k}$ in the first Brillouin zone, then we must fold all the bands displayed in the extended zone scheme in the first Brillouin zone by translation through reciprocal lattice vectors. This representation is known as the reduced zone scheme [191]. The representation in the reduced scheme can be periodically extended throughout all the $\mathbf{k}$-space. This representation is called the repeated zone scheme [191].

For the TE mode, for which we have

$$\tilde{\mathbf{H}}_{\mathbf{k},n} = (0, 0, \tilde{H}^z_{\mathbf{k},n}), \quad \tilde{\mathbf{E}}_{\mathbf{k},n} = (\tilde{E}^x_{\mathbf{k},n}, \tilde{E}^y_{\mathbf{k},n}, 0), \tag{3.87}$$

the photonic band structure diagram can be calculated as follows. Substituting Eq. (3.82) in Eq. (3.81) and making use of Eq. (3.87) and of

$$\mathbf{k}_{l,m} \cdot \mathbf{H}_{\mathbf{k},n} = 0, \tag{3.88}$$

yields

$$\omega_{n,\mathbf{k}}^2 \tilde{H}_{\mathbf{k},n}^z(\mathbf{K}_{l,m}) = \sum_{l',m'} \hat{\varepsilon}(\mathbf{K}_{l-l',m-m'}) \tilde{H}_{\mathbf{k},n}^z(\mathbf{K}_{l',m'})(\mathbf{k}_{l,m} \cdot \mathbf{k}_{l',m'}). \tag{3.89}$$

As for the TM case, Eq. (3.89) with $|l|, |m| \leq N$ allows to compute the photonic band structure diagram of TE polarized waves in two-dimensional photonic crystals.

From the photonic band structure diagram, the equifrequency surfaces (EFSs), that are surfaces of equal frequency in k space, can be obtained for the various photonic bands. Note that although in two dimensions we rather have equifrequency contours instead of EFS, in what follows we always use the term EFS. Since the photonic band structure diagram can be displayed in the reduced, repeated and extended zone scheme, also the EFSs can be displayed in these three schemes.

3.3.5 Wave vector diagram

In conventional geometrical optics, light propagation in dielectric materials is described by the phase refractive index and Snell's law (see Section 3.1). Light propagation in periodic structures, of which photonic crystals are an example, is different from that in conventional materials. The refraction phenomenon relies on the conservation of the wave vector and due to the periodical nature of these structures the wave vector $\mathbf{k}$ is not conserved. The direction of light propagation inside a photonic crystal is determined by the EFSs [3, 17, 192]. Notomi [3, 17] has theoretically analyzed the light propagation phenomenon in periodic structures and photonic crystals with the help of the band structure theory and numerical simulations. A more recent detailed systematic study of refraction phenomena occurring in two-dimensional photonic crystals based on the wave vector diagram formalism can be found in [18]. In this section we closely follow [3, 17, 18] to explain the wave vector diagram analysis.

We first consider a very simple example of wave vector diagram analysis shown in Fig. 3.11a, which graphically describes a light incident problem from air to a dielectric material. The wave vector diagram contains the EFSs that apply for the frequency of operation. For any isotropic homogeneous material, the EFS is a circle with radius $k = |\mathbf{k}| = |n|\omega/c$, $\mathbf{k}$ being the wave vector, $|n|$ the refractive index of the medium, ω the working frequency, and c the velocity of light in vacuum. For conventional isotropic homogeneous dielectric materials the phase refractive index is always larger than one. Hence, the circle for the dielectric material in Fig. 3.11a is larger than the one for air which has a refractive index equal to one. The incoming wave vector $\mathbf{k}$ is drawn on the reciprocal lattice such that it starts at the origin of the reciprocal lattice and such that it points in the direction of the incident wave. The length of $\mathbf{k}$ is determined by the EFS contour in air.

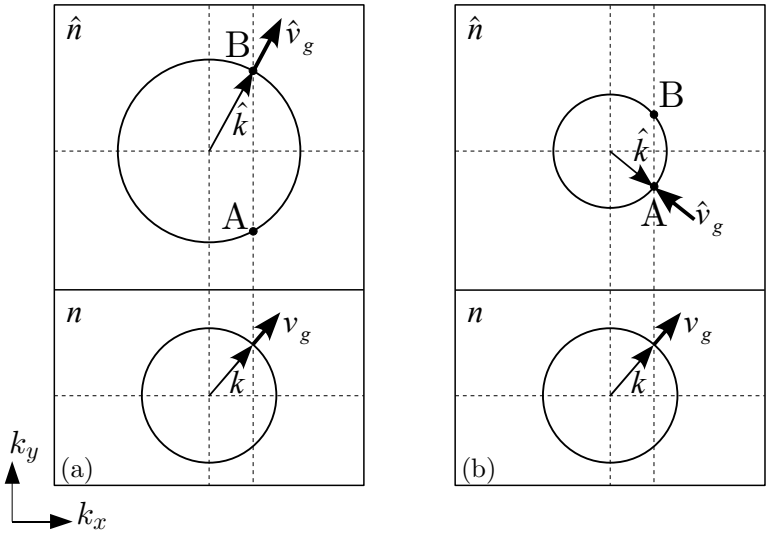

Figure 3.11: Wave vector diagram for a light incident problem from air ($n = 1$) to a homogeneous isotropic dielectric material with refractive index $\hat{n} > 1$ (a) and from air ($n = 1$) to a photonic crystal with $\hat{n} < 0$ (b). $\mathbf{k}$ and $\hat{\mathbf{k}}$ denote the incident and refracted wave vector, respectively; $\mathbf{v}_g$ and $\hat{\mathbf{v}}_g$ denote the corresponding group velocity vectors.

The tangential components of the wave vector $\mathbf{k}$ are always conserved at an interface between two isotropic materials. The $\mathbf{k}_{\|}$ conservation condition, indicated by the dotted line in Fig. 3.11a, determines the allowed refracted wave vectors $\hat{\mathbf{k}}$. There are two choices for $\hat{\mathbf{k}}$ (to point either towards A or towards B). The propagation direction is determined by the group velocity $\hat{\mathbf{v}}_g = \nabla_{\hat{\mathbf{k}}}\omega$ which is perpendicular to the EFS at the allowed $\hat{\mathbf{k}}$ points (point A or B) and which points towards increasing values of frequency. Since for a conventional homogeneous isotropic dielectric medium n is always larger than one, the radii of the EFS increase with increasing frequency. Hence the group velocity always points outwards and $\hat{\mathbf{v}}_g \cdot \hat{\mathbf{k}} > 0$. Furthermore, the correct choice of $\hat{\mathbf{k}}$ is the one that gives a $\hat{\mathbf{v}}_g$ that points away from the source. Hence, in this case $\hat{\mathbf{k}}$ should point to B. In fact, Fig. 3.11a is simply a graphical representation of Snell's law in $\mathbf{k}$ space [3, 17]

$$n_1 \sin\theta_1 = n_2 \sin\theta_2, \tag{3.90}$$

where n_1 and n_2 are the phase refractive indices of material 1 and 2, respectively and θ_1 and θ_2 are the angles the propagation directions in material 1 and 2 make with respect to the interface normal (see Fig. 3.1).

A similar graphical picture can be made to study light propagation in diffraction gratings and photonic crystals [3, 17, 68, 79, 168, 170, 179, 193–196]. For these structures, the EFSs are periodically repeated in the wave vector diagram and the $\mathbf{k}_{\|}$ conservation rule is generalized

to satisfy the periodic boundary condition. The $\mathbf{k}_{\parallel}$ conservation condition reads [58]

$$\mathbf{k}_{\parallel,m} = k \sin\theta + \frac{2\pi m}{a_s}, \tag{3.91}$$

where k denotes the length of the incoming wave vector, θ denotes the angle of incidence, a_s represents the periodicity of the interface and m is an integer equal to $0, \pm 1, \pm 2, \ldots$. In the wave vector diagram, Eq. (3.91) is represented by m parallel lines, all perpendicular to the interface and separated by a distance $2\pi m/a_s$. The lines are often called construction lines [194]. Using the vector diagram analysis, Notomi has shown that the propagation characteristics of diffraction gratings and weakly modulated photonic crystals, that is photonic crystals built from constituents with a small difference in dielectric constant ($\mu = 1$), are very similar [3, 17]. For such periodic structures a phase index in terms of Snell's law cannot be defined [3, 17]. If one would define a phase index, the index would strongly depend on the incident angle and therefore Snell's law loses its meaning. However, the wave vector diagram analysis can be used to explain typical features of a diffraction grating such as, for example, beam decomposition into diffracted waves and strong sensitivity of beam propagation to the incident angle and wavelength [3, 17]. Also the anomalous light propagation reported for photonic crystals such as for example the superprism effect and the ultrarefractive properties can be understood within this picture [3, 17]. Thus these phenomena cannot be understood within a refraction picture and must be understood as diffraction. Note that for a complete understanding of light propagation in diffraction gratings and photonic crystals it is not sufficient to study propagation modes in the first Brillouin zone [3, 18]. All allowed propagation modes in the repeated zone scheme should be investigated [3, 18].

However for strongly modulated photonic crystals near the photonic band gap an effective phase refractive index can be defined to explain the light propagation inside the photonic crystal using Snell's law and this in spite of the presence of strong multiple diffraction [3, 17]. For simplicity of notation, we also denote this effective refractive index by n. In strongly modulated photonic crystals, the phase refractive index can be smaller than one and can also be negative. This can lead to unusual refraction phenomena such as ultrarefractivity and negative refraction.

To explain this we consider a two-dimensional photonic crystal slab made from dielectric pillars with radius $r = 0.35a$ and $\hat{n} = 3.6$ arranged in a triangular lattice with lattice constant a [3, 17]. We use the MIT Photonic-Bands software [190] to calculate the photonic band structure diagram for the TE-mode. The result is shown in Fig. 3.12. For the dimensionless frequency range $f = \omega a/2\pi c \in [0.562, 0.607]$, we obtain the EFS depicted in Fig. 3.13. From Fig. 3.13 it can be seen that for increasing frequencies, that is for frequencies coming close to one of the gap frequencies, the shape of the EFSs becomes rounded and finally becomes circular. In the latter case, the EFS plot looks similar to that of a conventional dielectric material as shown in Fig. 3.11a. This means that we can define an effective refractive

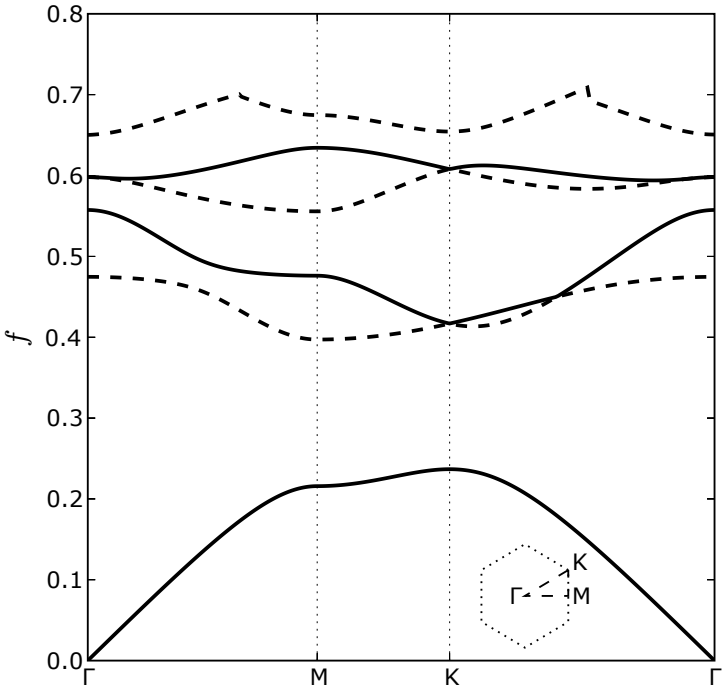

Figure 3.12: Photonic band structure diagram of TE modes for a two-dimensional photonic crystal made from dielectric pillars with radius $r = 0.35a$ and refractive index $\hat{n} = 3.6$ arranged in a triangular lattice with lattice constant a. $f = \omega a/2\pi c$ is the dimensionless frequency. The first Brillouin zone of a triangular lattice and the symmetry points are shown in the inset (see Appendix A).

index $\hat{n}$ from the radius of the EFS using Snell's law, suggesting that for these frequencies the beam propagation is refraction like. However, for these frequencies there is a striking difference from conventional refraction. For example, for the frequency $f = 0.6$, the radius of the EFS gives $|\hat{n}| = 0.47$. Hence, in the schematic picture that describes the light incident problem from air to the photonic crystal, the circle (equifrequency contour) for air is larger than the one for the photonic crystal (see Fig. 3.11b). As a consequence, for certain angles of incidence no light beam propagates in the photonic crystal since the light is totally reflected off the interface. This corresponds to total internal reflection, a phenomenon which does not occur when a light beam is incident from air to a conventional material.

The sign of $\hat{n}$ is determined from the behavior of the EFSs. In this case the EFSs move inwards with increasing frequency, as can be seen from Fig. 3.13. Hence $\hat{\mathbf{v}}_g \cdot \hat{\mathbf{k}} < 0$. It can be proven analytically that for the infinite photonic crystal system, the direction of the group velocity coincides with the direction of the energy velocity [58, 197]. Therefore, the group velocity vector represents the direction of propagation for the electromagnetic wave in the photonic crystal. The sign of $\hat{n}$ is given by the sign of $\hat{\mathbf{v}}_g \cdot \hat{\mathbf{k}}$ (see Section 3.2.1). Thus in this

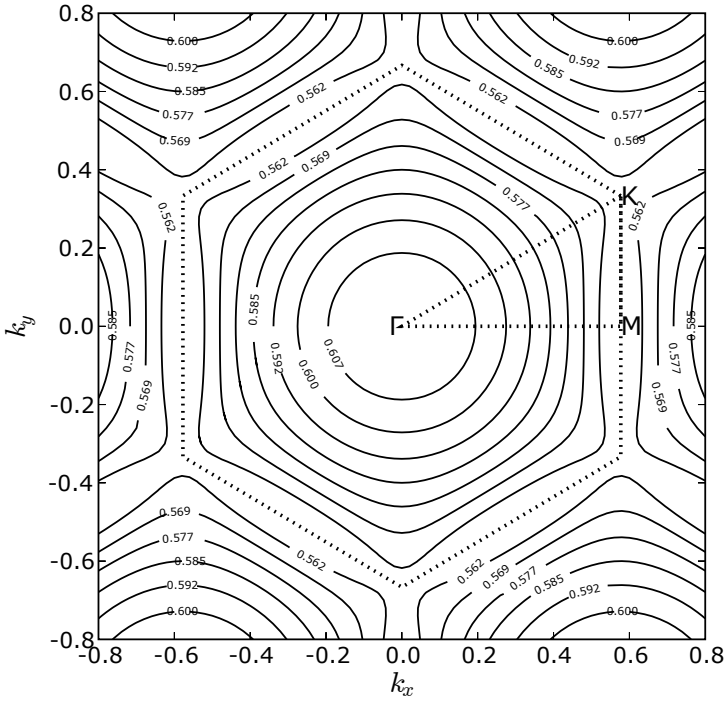

Figure 3.13: EFS plot of TE modes in a two-dimensional photonic crystal made from dielectric pillars with radius $r = 0.35a$ and refractive index $\hat{n} = 3.6$ positioned in a triangular lattice with lattice constant a. The frequencies f range from 0.562 to 0.607. The first Brillouin zone of a triangular lattice (dotted line) and the symmetry points are also shown (see Appendix A).

case we have $\hat{n} = -0.47$. The propagation direction of the electromagnetic wave is inward. This results in a negative propagation angle for all incident angles. Schematically, this can be seen from Fig. 3.11b. Due to the $\mathbf{k}_{||}$ conservation rule, there are two choices for $\hat{\mathbf{k}}$, to point towards A or to point towards B. Since the direction of propagation is determined by the group velocity and points away from the source, $\hat{\mathbf{k}}$ should point to A. The group velocity is perpendicular to the EFS at point A. Note that for this particular example, it is sufficient to study the propagation modes in the first Brillouin zone only. Therefore it is sufficient to display the EFSs in the reduced zone scheme. In what follows, we will only use the extended or repeated zone scheme if it is necessary to explain the wave propagation.

The wave vector diagram analysis method is an adequate method to determine the propagation angles. However, since the method gives no information on the amplitude across the interface, it cannot be predicted whether or not waves with these propagation angles are excited by the incident wave.

3.3.6 Note on the use of two-dimensional models

Since three-dimensional FDTD calculations are very time and computer memory consuming and since we want to explore a large parameter space we study in the following chapters only three-dimensional photonic crystals with translational invariance in the z-direction. As mentioned before, in this case the numerical problem of solving the time-dependent Maxwell equations reduces to a two-dimensional problem and the time-dependent Maxwell equations can be solved for the TM and TE mode separately.

In contrast to these pure two-dimensional photonic crystals, the two-dimensional photonic crystals investigated in many experiments are not infinite in the z-direction. Two-dimensional photonic crystals are often fabricated by sandwiching a central layer of a dielectric material between two other layers with a lower index of refraction than the central layer. Note that the two outer layers can also be considered to be air so that only one thin layer of dielectric material is present. The upper and lower layer can be chosen to be identical in order to construct a so-called symmetric waveguide, or different, to construct an asymmetric waveguide. In most cases the photonic crystals consist of a periodic pattern of air holes deeply etched in these waveguide structures, but several other constructions can be thought of [198]. All these structures are called planar photonic crystals or photonic crystal slabs. We prefer the name planar photonic crystals in order to make a distinction between slabs in two and three dimensions. Namely, a two-dimensional plate of a photonic crystal is also called a slab. In what follows, we only consider symmetric waveguides.

In planar photonic crystals, electromagnetic waves are confined in the vertical direction by waveguiding with dielectric index mismatch and in the horizontal direction by the two-dimensional photonic crystal. Two-dimensional calculations cannot be used to study these three-dimensional structures. However, in order to minimize the computational efforts, the theoretical analysis of these structures is often restricted to two-dimensional approximate models, making use of an effective refractive index [199, 200]. In order to identify the modes that can radiate vertically, the projected band structure is computed. The eigensolutions of the bulk top and bottom layer are $\omega = c\sqrt{|\mathbf{k}|^2 + k_z^2}/n_0$, where n_0 denotes the refractive index of the dielectric material of the top and bottom layer, $\mathbf{k} = (k_x, k_y)$ denotes the two-dimensional Bloch wave vector and k_z denotes the z-component (vertical component) of the wave vector. If these eigensolutions are plotted against $\mathbf{k}$, they form the so-called light cone $\omega \geq c\,|\mathbf{k}|\,/n_0$. The light-line $\omega = c\,|\mathbf{k}|\,/n_0$ in the photonic band structure diagram separates the radiation from the guided modes. The guided modes lie below the light line and are stationary Bloch modes that are ideally not subject to propagation losses. These modes are infinitely extended within the plane of the planar photonic crystal and decay exponentially into the vertical direction. This confinement is analogous to internal reflection and is due to the difference in refractive index between the central and outer layers (higher effective refractive index in the central layer compared to the refractive index in the outer layers). Above the light line, the

spectrum becomes a continuum of modes. At the edge of the light cone, there exist resonances called quasi-guided modes. These modes exhibit intrinsic propagation losses due to out-of-plane diffraction. Photonic band gaps that are complete for a pure two-dimensional photonic crystal become incomplete band gaps in the guided mode spectrum. For a planar two-dimensional photonic crystal, a band gap is a range of frequencies in which no guided modes exist. It is an incomplete band gap because there are still radiation modes at those frequencies. The presence of a gap is strongly dependent on the thickness of the planar photonic crystal [198]. The height of the planar photonic crystal should not be too small in order not to have a weak confinement of the modes inside the structure and not too large in order not to allow higher order modes that fill the gap. If, as in the cases we consider in this section, the horizontal mid-plane of the planar photonic crystal is a mirror symmetry plane, then the guided bands can be classified according to whether they are even or odd with respect to reflections through this plane. These even and odd modes have strong similarities with the TE and TM modes, respectively, of the ideal two-dimensional photonic crystal, and are therefore called TE-like and TM-like modes. Note that in the mirror plane itself, the even and odd modes are pure TE and TM modes, respectively.

Comparison of approximate two-dimensional calculations that use an effective refractive index with full three-dimensional calculations has shown that good qualitative agreement can be obtained [199, 200]. Evidently, the two-dimensional transmission is considerably larger than the corresponding three-dimensional transmission because no out-of-plane losses are included in the two-dimensional calculations [200]. In [201], a two-dimensional study of losses in planar photonic crystals has been made using a two-dimensional model, which treats a system of trenches etched in the step-index dielectric waveguide [201]. Also in this study good qualitative agreement has been found with the full three-dimensional results [201]. Hence, two-dimensional numerical studies can provide sufficient guidance in designing planar photonic crystals for various purposes.

In the following chapters we consider pure two-dimensional photonic crystals and not the planar photonic crystals as mentioned before. However, these planar photonic crystals are only one alternative to real three-dimensional photonic crystals studied in experiments. Namely, in order to have, in experiments, full control of electromagnetic wave propagation in photonic crystals, a complete photonic band gap is required. This can only be found in a three-dimensional photonic crystal, but they are very difficult to fabricate (see Section 3.3.1). As an alternative, three-dimensional crystals are made from their two-dimensional analogues, either by making planar photonic crystals, having vertical radiation losses that can be minimized to tolerable levels by various strategies, or by making photonic crystals with very deep holes or very long cylinders, that is by increasing the vertical dimension of the photonic crystal until this dimension can be treated as infinite. Macroporous silicon is an example of the latter kind of photonic crystals [202–205]. Recently, a similar photonic crystal made from another material was used to demonstrate negative refraction and to make a lens with subwavelength

resolution [118]. Our two-dimensional simulation results presented in the following chapters can provide guidance in designing these very long hole or very long cylinders type of photonic crystals for various purposes.

Chapter 4

Focussing light in triangular lattice photonic crystals

In the previous chapter, we have discussed the possibility to observe negative refraction in photonic crystals and to focus light by means of thin slabs of photonic crystal material. In this chapter, we study these phenomena in great detail for triangular lattice photonic crystals. We present finite-difference time domain (FDTD) simulation results for the propagation of light in planar photonic crystals with triangular lattice symmetry and use the FDTD technique described in Chapter 2 to investigate the space and time evolution of the electromagnetic waves. Photonic band structure diagrams and equifrequency surface (EFS) plots are obtained by using the MIT Photonic-Bands software [190].

4.1 Dielectric circular rods in air

In this section, we study photonic crystal structures made from dielectric cylindrical pillars organized in a triangular lattice. The pillars are surrounded by air. We use $\varepsilon = 12.96$ for the dielectric constant, $\mu = 1$ for the magnetic permeability and $r = 0.35a$ for the radius of the rods, where a denotes the lattice constant. This allows us to compare some of our results to the results presented in Refs. [3, 17, 79].

4.1.1 Photonic band structure diagram and EFS plots

The photonic band structure diagram for the TE mode (magnetic field aligned along the axis of the cylinders) is shown in Fig. 3.12. For the dimensionless frequency range $f = \omega a/2\pi c \in$

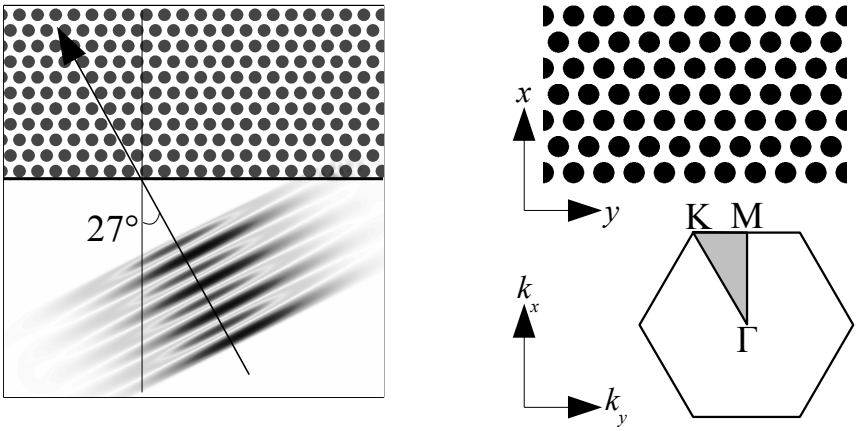

Figure 4.1: Left: Amplitude of the magnetic field of an electromagnetic wave propagating along a 27° direction from air into a photonic crystal system. For the simulation parameters we refer to the text. The snapshot is taken at $t = 5\lambda/c$. Top right: Schematic picture of the photonic crystal system consisting of dielectric rods with radius $r = 0.35a$ and $n = 3.6$ arranged in a triangular lattice with lattice constant a. Bottom right: First and irreducible (shaded region) Brillouin zone of a triangular lattice (see Appendix A). Note that in Section 4.1.2, we use a Cartesian coordinate system in which we interchange the role of x and y (see text).

$[0.562, 0.607]$, corresponding to frequencies in band 5, the EFS plot is depicted in Fig. 3.13. As discussed in Section 3.3.5, for some frequencies the shape of the EFS becomes circular. In that case, we can define an effective refractive index $\hat{n}$ from the radius of the EFS using Snell's law. Since for band 5 the equifrequency contours move inwards with increasing frequency, as can be seen from Fig. 3.13, the effective refractive index is negative.

4.1.2 Reflection and refraction at the interface between air and the photonic crystal

Foteinopoulou *et al.* showed by means of FDTD simulations that a TE wave, with dimensionless frequency $f = \omega a/2\pi c = 0.58$, coming from air and hitting the photonic crystal interface refracts in the negative direction [79]. As a check, we repeat the numerical simulations on the photonic crystal system as described in [79]. As discussed in Section 1.2, we adopt the convention that in our simulations the wave is propagating along the x-direction. Therefore, as in [79] the wave is propagating in the upward direction and not from left to right, we use for this particular example a Cartesian coordinate system in which the x- and y-axis are interchanged.

The dimensions of the photonic crystal slab are $8\lambda \times 20\lambda$. The total simulation area has dimensions $L_x = 16\lambda$ and $L_y = 20\lambda$. The boundaries of the simulation area are absorbing. We discretize space in a square grid with lattice spacing $\delta = 0.01\lambda$. This results in a total

number of lattice points of 3200000. We use a time step $\delta t = 0.001\lambda/c$. A finite line source modeled by Eq. (3.60) is placed in front of the air/photonic crystal interface at an angle of 27°, as shown in Fig. 4.1. Note that the air/photonic crystal interface is perpendicular to the ΓM direction. The source starts gradually emitting at $t = 0$ a TE wave (the $\mathbf{E}$ field in the plane of incidence) of dimensionless frequency $f = 0.58$. As indicated in Fig. 4.1, the propagation direction of the wave is almost along the ΓK symmetry direction of the triangular lattice. In the work of Foteinopoulou *et al.* the incident wave propagates along a 30° direction from air into the photonic crystal system, that is the incident wave propagates exactly along the ΓK symmetry direction of the triangular lattice [79]. We have chosen a slightly different angle of incidence in order to be able to put the line source on the grid points of the square grid (in [79] a rectangular grid is used). Also note that our line source is different from the one used in [79]. In [79] an almost monochromatic source with half-width $\Delta\omega \simeq 0.02\omega$ is used, while the source we use is monochromatic.

A detailed time sequence of our simulation results for the light propagation of the magnetic field in the photonic crystal system is shown in Fig. 4.2f-j. For comparison, we also present the results of Foteinopoulou *et al.* [79] (Fig. 4.2a-e). The material structure of the photonic crystal slab is not shown in the snapshots in order to give a better image of the light propagation inside the slab. As discussed by Foteinopoulou *et al.* [79], the wave is trapped initially at the interface, gradually reorganizes itself, and finally propagates along the negative angle direction. Our simulation results qualitatively agree with the results in [79].

The direction of propagation in the photonic crystal can be predicted from the EFS analysis presented in Fig. 4.3a. The EFS for air and for the photonic crystal for a frequency $f = 0.58$ is represented by the thin and thick solid contours, respectively. The shape of the EFS for the photonic crystal is a rounded hexagon and is not a perfect circle. This results in an anisotropic $\hat{n}(\mathbf{k})$. Therefore we expect to have different values for the refractive index along different propagation directions with incoming wave vector $\mathbf{k}$. The magnitude of the angle dependent effective refractive index can be derived from the radius of the EFS. For an angle of incidence of 27° we find $|\hat{n}(27^\circ)| \approx 0.75$. The sign of $\hat{n}$ can be determined from the behavior of the EFSs.

The incoming wave vector $\mathbf{k}$ is drawn on the reciprocal lattice such that it starts at the origin of the reciprocal lattice (the Γ-point) and such that it points in the direction of the incident wave. The length of the vector is determined by the radius of the EFS in air (see Fig. 4.3a). Application of the k conservation rule, given by the dashed vertical line in Fig. 4.3a, determines the allowed refracted wave vectors $\hat{\mathbf{k}}$. There are two choices for $\hat{\mathbf{k}}$, pointing towards A or towards B. For every choice of $\hat{\mathbf{k}}$ the corresponding group velocity vector $\mathbf{v}_g = \nabla_{\mathbf{k}}\omega$ is normal to the EFS at point A or B (depending on the choice for $\hat{\mathbf{k}}$) and points towards increasing values of frequency. The correct choice for $\hat{\mathbf{k}}$ is the one that gives a $\mathbf{v}_g$ that points away from the source. As can be seen from the EFS plot in Fig. 3.13, the frequency increases

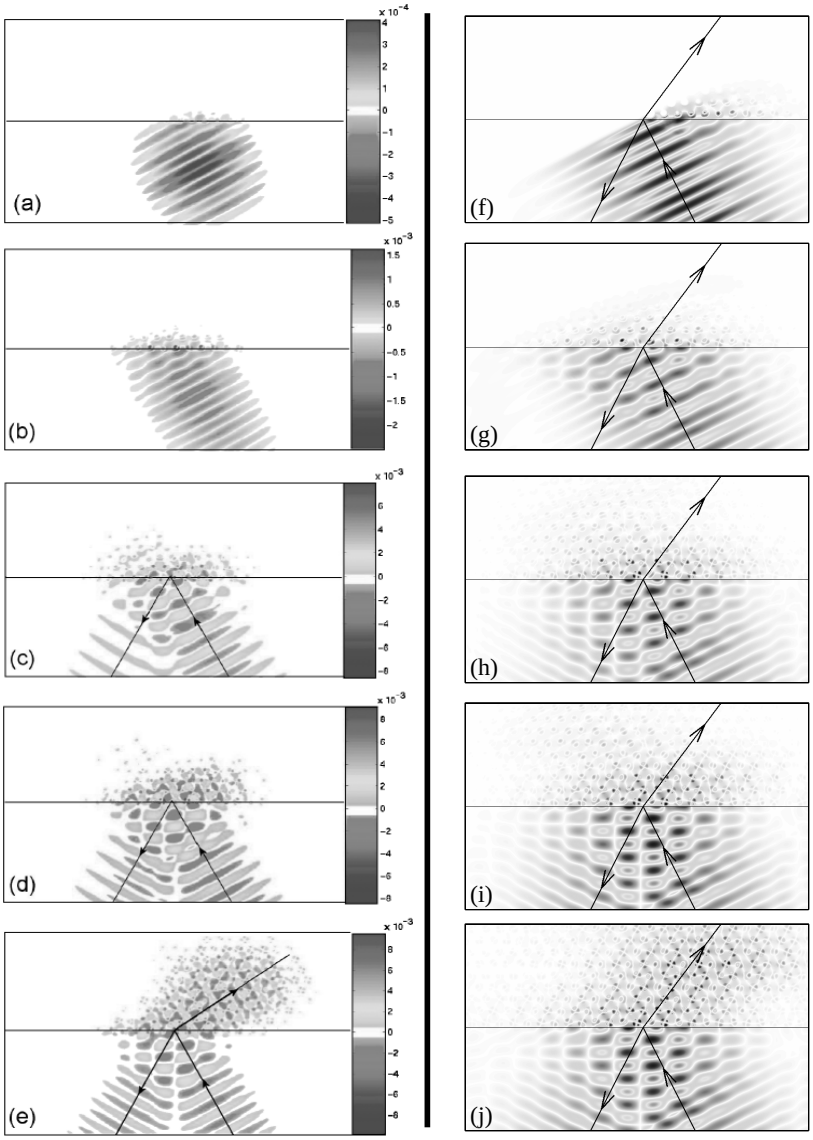

Figure 4.2: Time sequence of the amplitude of the magnetic field of the electromagnetic wave undergoing reflection and refraction at the interface between air (bottom part of the figures) and the photonic crystal (top part of the figures). (a)-(e): FDTD simulation results by Foteinopoulou *et al.* [79] for an angle of incidence of 30°. The arrows indicate the direction of propagation. (f)-(j): Our FDTD simulation results for an angle of incidence of 27°. The arrows indicate the direction of propagation according to Snell's law and the law of refraction for the case of reflection and refraction at an interface between air and a homogeneous isotropic material with $\hat{n} = -0.75$. For the simulation parameters we refer to the text. Snapshots are taken at (a): t=3.7; (b): t=6.7; (c): t=15.6; (d): t=22.3; (e): t=46; (f): t= 4; (g): t=7; (h): t=16; (i): t=22; (j): t=46 (t is in units of λ/c).

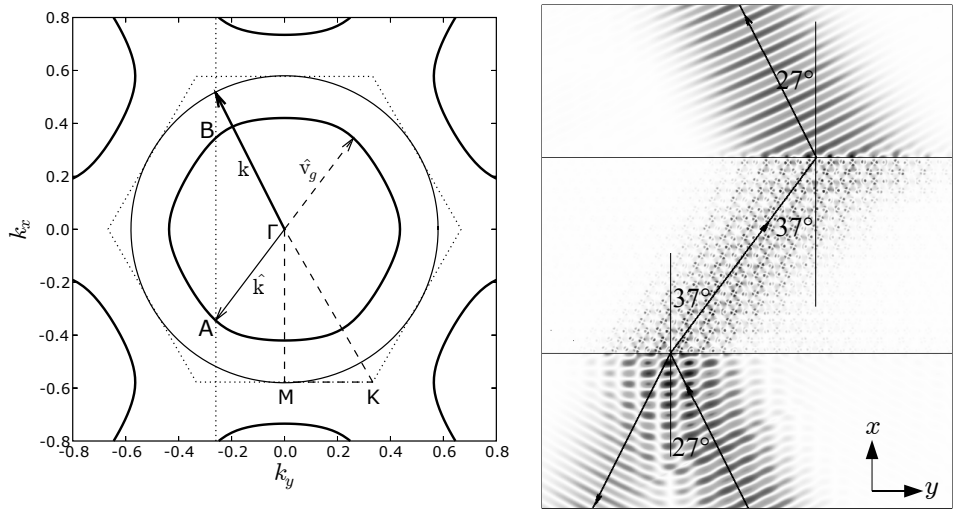

(a) (b)

Figure 4.3: (a): Schematics of refraction of an electromagnetic wave (TE mode) with frequency $f = 0.58$ at the air/photonic crystal interface. The angle of incidence is $27°$. The thin and thick solid contours represent the EFSs for air and the photonic crystal, respectively. $\mathbf{k}$ is the incident wave vector, $\hat{\mathbf{k}}$ the refracted wave vector, and $\hat{\mathbf{v}}_g$ the group velocity vector of the refracted wave. The dotted vertical line represents the conservation of the parallel component of the wave vector. The first Brillouin zone (dashed hexagon) and the symmetry points are also shown (see Appendix A). (b): Amplitude of the magnetic field of an electromagnetic wave propagating along a $27°$ direction from air into a photonic crystal slab. The snapshot is taken at $t = 120\lambda/c$. The arrows indicated the direction of propagation according to Snell's law and the law of reflection for the case of a homogeneous isotropic slab with refractive index $n = -0.75$ and thickness $10.63a$. For the simulation parameters we refer to the text. Note that in Section 4.1.2, we use a Cartesian coordinate system in which we interchange the role of x and y (see text).

inwards, hence the correct choice for $\hat{\mathbf{k}}$ is to point towards point A. Consequently, $\mathbf{v}_g \cdot \mathbf{k} < 0$ and $\hat{n} < 0$. Since the group velocity coincides with the energy velocity, the group velocity vector in Fig. 4.3a represents the direction of propagation for the electromagnetic wave in the photonic crystal.

The theoretically predicted value for the effective refractive index is thus $\hat{n} = -0.75$. Using Snell's law this results in an angle of refraction of $-37°$. In our simulation we find an angle of $-40°$, as can be seen from Fig. 4.2j. Foteinopoulou *et al.* found a refraction angle of $-44°$ (see Fig. 4.2e). They however assumed that the photonic crystal system has an effective refractive index of -0.7 [79]. Indeed, for an angle of incidence of $30°$, we also find $\hat{n}(30°) = -0.7$. For this value of $\hat{n}$ the theoretically predicted angle of refraction is $-46°$. Hence, both our simulations and the simulations of Foteinopoulou *et al.* show a small deviation from Snell's law. This might be due to the relatively early point in time at which the snapshots are taken. If we study the light propagation through a photonic crystal slab of thickness $10.6259a$ we find good agreement with Snell's law, as shown in the snapshot in Fig. 4.3b

taken at $t = 120\lambda/c$. For earlier times, deviations from Snell's law are also observed (results not shown).

In conclusion, our results qualitatively agree with the results presented in [79]. A quantitative comparison cannot be made because of a lack of detailed information about the simulation setup in [79]. The negative angle of refraction obtained from the FDTD simulations agrees quite well with the angle predicted from the EFS analysis. The agreement can also be seen from the data presented in [3, 17, 65, 79, 206].

4.2 Circular air holes in dielectric material

Although the photonic crystal system described in the previous section has a negative effective refraction index $\hat{n}$ for some frequencies, $|\hat{n}|$ is always smaller than one. However, as described in Section 3.2.4, the interesting property of negative index materials to focus light occurs for $\hat{n} = -1$. Therefore, in this section we study photonic crystals that have $\hat{n} \approx -1$ [3, 171–176, 196].

In this section we study photonic crystal structures made of dielectric material with circular holes drilled in a triangular lattice configuration. If not mentioned otherwise, we use the value of 12.96 for the dielectric constant, $\mu = 1$ and $r = 0.4a$ for the radius of the holes, where a denotes the lattice constant. This allows us to compare some of our results to the results presented in [3, 17, 171, 173–176, 196].

4.2.1 Photonic band structure diagram and EFS plots

The photonic band structure diagram for the TM mode is shown in Fig. 4.4. For the dimensionless frequency range $f = \omega a/2\pi c \in [0.26, 0.33]$, corresponding to frequencies in band 2, the EFS plot is depicted in Fig. 4.5a. For some frequencies the shape of the EFSs becomes circular. In that case, we can define an effective refractive index $\hat{n}$ from the radius of the EFS using Snell's law (see Section 3.3.5). The EFSs move inwards with increasing frequency and hence, $\hat{n} < 0$. In Fig. 4.5b we show the effective refractive index $\hat{n}$ as a function of the angle θ of the incoming wave vector $\mathbf{k}$ for various frequencies f. As can be seen from Fig. 4.5b, for $f = 0.3$ the effective refractive index $\hat{n}$ is almost equal to -1 and only fluctuates a little as a function of θ. Note that relatively small changes in the frequency lead to relatively large changes in the effective refractive index.

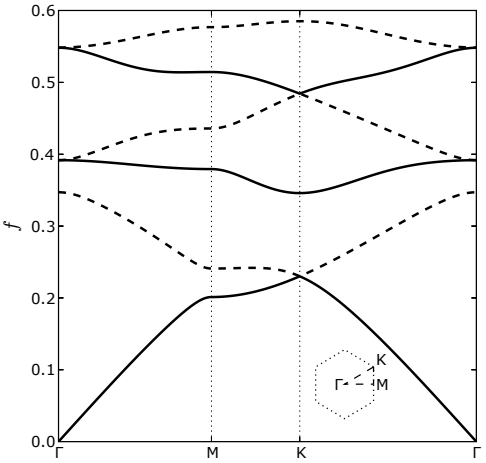

Figure 4.4: Photonic band structure diagram of TM modes for a triangular lattice photonic crystal consisting of air holes drilled in a dielectric medium ($\varepsilon = 12.96, \mu = 1$). The holes have a radius $r = 0.4a$. $f = \omega a/2\pi c$ is the dimensionless frequency. The first Brillouin zone of a triangular lattice and the symmetry points are shown in the inset (see Appendix A).

4.2.2 Negative refraction and Snell's law

As discussed in Section 3.3.5, the EFS analysis can be used to predict the direction of light propagating from air into a photonic crystal slab. From Fig. 4.5 it can be seen that the theoretically predicted value for the effective refractive index at the frequency $f = 0.3$ is $\hat{n} \approx -1$. Using Snell's law for an angle of incidence of 26.57°, this results in an angle of refraction of -26.57°. In Fig. 4.6 we make a comparison between this theoretical result and our FDTD simulation results. We consider a photonic crystal slab with dimensions $6.48\lambda \times 26\lambda$. The total simulation area has dimensions $L_x = 30\lambda$ and $L_y = 26\lambda$. The boundaries of the box are absorbing. We discretize space, using a square grid with lattice spacing $\delta = 0.01\lambda$. We use a time step $\delta t = 0.001\lambda/c$. A finite line source modeled by Eq. (3.60) with $W = 6\lambda$, is placed in front of the air/photonic crystal interface at an angle of 26.57° as shown in Fig. 4.6. The source starts gradually emitting at $t = 0$ a TM wave of dimensionless frequency $f = 0.3$. The snapshots depicted in Fig. 4.6 are taken at $t = 14\lambda/c$ (a), $t = 25\lambda/c$ (b) and $t = 60\lambda/c$ (c). The material structure of the photonic crystal slab is not shown in the snapshots in order to give a better image of the light propagation inside the slab. Note that the air/photonic crystal interface is perpendicular to the ΓM direction. The arrows indicate the direction of propagation according to Snell's law and the law of reflection for the case of a homogeneous isotropic slab with $\hat{n} = -1$. For small times t, light propagation does not follow Snell's law and no negative refraction is seen (see Fig. 4.6a). The refracted beam seems to propagate towards positive angles. However, after some time ($t > 20\lambda/c$) the refracted beam bends into the negative direction (see Fig. 4.6b). Then it still takes some time ($20\lambda/c \leq t \leq 50\lambda/c$)

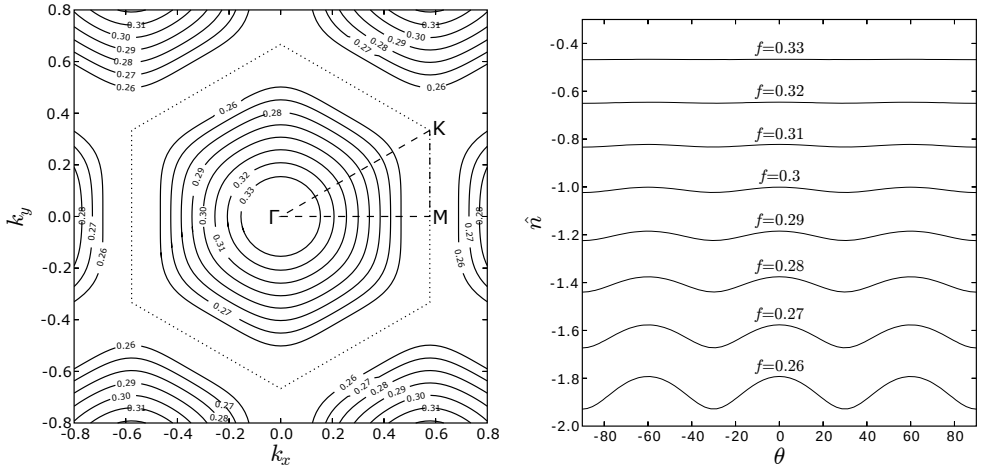

(a) (b)

Figure 4.5: (a): EFS plot for the frequency range $f = \omega a/2\pi c \in [0.26, 0.33]$ corresponding to band 2 in Fig. 4.4. The first Brillouin zone of a triangular lattice (dotted line) and the symmetry points are also shown (see Appendix A). (b): Effective refractive index $\hat{n}$ (obtained from the EFS plot shown in the left panel) as a function of the angle θ of the incoming wave vector $\mathbf{k}$ for the frequency range $f = 0.26 - 0.33$.

before the transmitted beam on the right hand side of the slab propagates according to Snell's law (see Fig. 4.6c). From that time on, there is a very good agreement between the negative angle of refraction obtained from the EFS analysis and from the FDTD simulations. For other angles of incidence small deviations from Snell's law can be seen since the effective refractive index is not exactly equal to minus one for all angles of incidence (see Fig. 4.5). A similar transient time during which the wave reorganizes and finally moves along negative directions is observed in [79] (see Section 4.1.2). Results of a more detailed investigation of the transient times in negative and positive index photonic crystals are presented in [207].

Light propagating through a homogeneous isotropic slab with $\hat{n} = -1$ and which is embedded in air, does not reflect at the air/slab interface. However, light propagating through a slab of photonic crystal with an effective refractive index $\hat{n} = -1$, is reflected at the air/slab interfaces, as can be clearly seen in Fig. 4.6. This results in a considerable loss of intensity of the transmitted wave. Using the layer-KKR (Korringa-Kohn-Rostoker) method, Ruan *et al.* have calculated the reflection coefficient as a function of the incident angle [196]. For the air/slab interface normal to the ΓM direction the minimum reflection coefficient is about 35% [196]. However, the reflection can be reduced by cutting the surface [172]. In general, transmission depends strongly on the surface termination of the photonic crystal slab [122, 172, 174, 208, 209]. So, although the EFS analysis method is an adequate method to determine the propagation angles for refraction at an air/photonic crystal interface, the method does not give any information about the amplitude of the propagating wave. More-

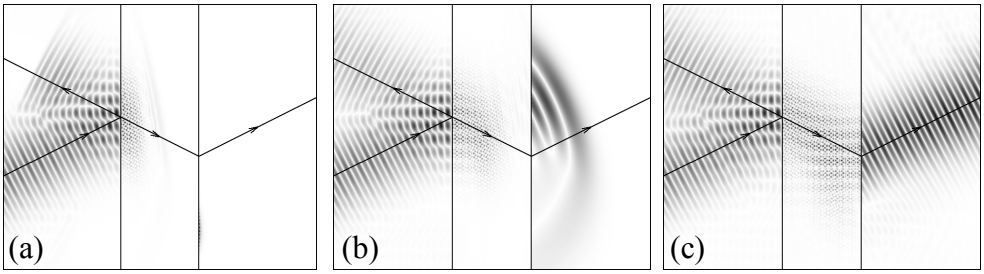

Figure 4.6: Amplitude of the electric field of a TM wave propagating along a $26.54°$ direction from air into a slab made from a two-dimensional photonic crystal consisting of a dielectric medium ($\varepsilon = 12.96$) with holes of radius $r = 0.4a$ drilled in a triangular lattice configuration with lattice constant a. The thickness of the slab is $12\sqrt{3}a + 0.8a$. The air/photonic crystal interface is perpendicular to the ΓM direction. The snapshots are taken at $t = 14\lambda/c$ (a), $t = 25\lambda/c$ (b) and $t = 60\lambda/c$ (c). The arrows indicate the direction of propagation according to Snell's law and the law of reflection for a homogeneous isotropic slab with $\hat{n} = -1$. The amplitudes are plotted on a linear scale ranging from -1 to +1 and are scaled differently for the regions on the left and right of the slab and inside the slab.

over, although for some frequencies an effective index of refraction, defined by the radius of a circular EFS, can be associated with the photonic crystal, the photonic crystal cannot be considered as a homogeneous isotropic material. This was also observed in an experimental and theoretical analysis of the self-focussing effect of light by a photonic crystal lens consisting of alumina rods arranged in a triangular lattice [120]. For lenses with the surface normal of the slab along the ΓK direction, only light rays that propagate at large angles from the ΓK direction can enter the photonic crystal slab [120]. Hence, most of the light is reflected. A similar conclusion was made in [196] in which the coupling between plane waves in conventional dielectric media and Bloch waves in photonic crystals with negative effective refractive index is studied.

4.2.3 Imaging by a flat slab: single source

Although a photonic crystal with negative refractive index does not behave as a homogeneous negative index material, a flat slab of negative index photonic crystal material can focus electromagnetic waves with a subwavelength resolution. The focussing effects have been shown experimentally [119–121, 124] as well as theoretically [3, 17, 120, 121, 124, 170–175]. Note that here we only mention the results obtained for triangular-lattice photonic crystals. In spite of the relatively large amount of publications related to the topic of photonic crystal lenses, no systematic study of the properties of photonic crystal imaging has been made. In this section we make a detailed analysis of the focussing properties of a photonic crystal slab with $\hat{n} \approx -1$.

4.2.3.1 Effects of surface terminations

It is well known that the terminations of the slab have an influence on the strength and sharpness of the external focus, that is the image [122, 172–174, 208, 209]. Therefore we first study the imaging properties of a photonic crystal slab with $\hat{n} \approx -1$ for various surface terminations.

The system we consider is composed of a photonic crystal slab, which is surrounded by air. The slab has a thickness D. We specify D in the number of rows of air holes (N) minus two times the width C of the cut area at the air/photonic crystal interfaces, and/or in units of λ. The formula to compute D reads

$$D = (N-1)\sqrt{3}/2 + 2(r - C). \tag{4.1}$$

The simulation area has dimensions $L_x = 10\lambda$ and $L_y = 10\lambda$. The boundaries of the box are absorbing. We discretize space using a square grid with lattice spacing $\delta = 0.01\lambda$ and we use a time step $\delta t = 0.001\lambda/c$. A point source located at $\mathbf{r} = \mathbf{r}_0$ and modeled by

$$\mathbf{J}(\mathbf{r}, t) = \mathbf{O}\,\theta(t)\delta(\mathbf{r} - \mathbf{r}_0)\sin\Omega t, \tag{4.2}$$

where Ω is the angular frequency of the source and $\mathbf{O}$ defines the direction of the electric current, is placed in front of the air/photonic crystal interface at a distance L from the interface. As indicated by the step function $\theta(t)$ in Eq. (4.2), the source is turned on at $t = 0$. In order to have a photonic crystal slab with $\hat{n} \approx -1$, at $t = 0$ the point source starts gradually emitting a TM wave of dimensionless frequency $f = 0.3$. To analyze the image quality, we first let the system evolve in time until a stationary state is reached and then we average the electric field intensity over one period $2\pi/\Omega$.

Figure 4.7 depicts the electric field intensities $\mathbf{E}^2(\mathbf{r}, t)$ for photonic crystal slabs containing 9 rows of air holes and having various surface terminations. Because of the relatively large intensity in the images inside and behind the slab, compared to the intensity in the surroundings, intensities are plotted on the $\log_{10}$ scale. The material structure of the photonic crystal slab is not shown in order to give a better picture of the light focussing inside the slab. The lines indicate the direction of propagation according to Snell's law for the case of a homogeneous isotropic slab with $\hat{n} = -1$. From Fig. 4.7, it can be clearly seen that the best image is obtained for a slab with $C = 0.4r$ or $C = 0.5r$. For these surface terminations, the image is well-separated from the air/photonic crystal interface and there is relatively good agreement between our simulation results and the results obtained from the rules of geometric optics. As well inside as outside the photonic crystal slab an image is formed. The external image, that is the image formed on the right hand side of the slab is not circular, but elongated in the direction of propagation. This has also been observed in previous works [121, 170, 175] and is due to slight deviations of $\hat{n}$ from -1 for different angles of incidence.

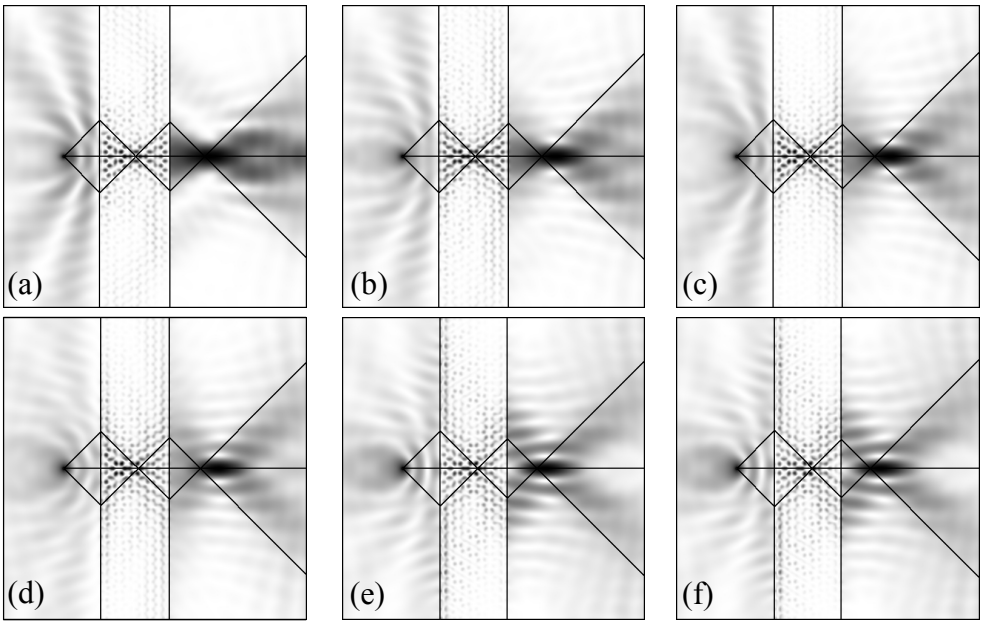

Figure 4.7: Intensity of the electric field of a TM wave, generated by a point source placed at a distance L from the air/photonic crystal interface of a slab made from a two-dimensional photonic crystal consisting of a dielectric medium ($\varepsilon = 12.96$) with holes of radius $r = 0.4a$ drilled in a triangular lattice configuration with lattice constant a. The thickness of the slab is denoted by D and is defined by the number N of rows of air holes (here $N = 9$) and by the width C of the cut area at the air/photonic crystal interfaces: $D = (N-1)\sqrt{3}a/2 + 2(r - C)$. The air/photonic crystal interfaces are perpendicular to the ΓM direction. The lines indicate the direction of propagation according to Snell's law for a homogeneous isotropic slab with $\hat{n} = -1$. Intensities are plotted on the $\log_{10}$ scale. The intensities are scaled between 0 and 1 and are scaled differently for the regions to the left and right of the slab and inside the slab. (a): $L = 1.19\lambda$, $D = (4\sqrt{3} + 0.8)a = 2.32\lambda\,[C = 0]$. (b): $L = 1.20\lambda$, $D = (4\sqrt{3}+0.8-0.08)a = 2.29\lambda\,[C = 0.1r]$. (c): $L = 1.21\lambda$, $D = (4\sqrt{3}+0.8-0.16)a = 2.27\lambda\,[C-0.2r]$. (d): $L = 1.23\lambda$, $D = (4\sqrt{3}+0.8-0.24)a = 2.25\lambda\,[C = 0.3r]$. (e): $L = 1.24\lambda$, $D = (4\sqrt{3}+0.8-0.32)a = 2.22\lambda\,[C = 0.4r]$. (f): $L = 1.25\lambda$, $D = (4\sqrt{3} + 0.8 - 0.4)a = 2.2\lambda\,[C = 0.5r]$.

Figure 4.8 shows the electric field intensity distribution $\mathbf{E}^2(\mathbf{r}, t)$, plotted along the image center perpendicular (dashed line) and parallel (solid line) to the slab surface, for the 9-layer slab with $C = 0.5r$ (see Fig. 4.7f). The spatial resolution of the imaging, defined as the ratio of the full width at half maximum (FWHM) to λ, is $R_x = 1.34$ and $R_y = 0.42$. These numbers are comparable to the numbers found in previous work [174–176]. Note that the electric field intensity distribution, plotted along the image center perpendicular to the slab surface (dashed line) is not only quite broad but is also asymmetric. As discussed before, the image is elongated in the direction of propagation due to slight deviations of $\hat{n}$ from -1 for different angles of incidence. The asymmetry of the image in the direction of propagation is due to a difference in interference effects very near the slab interface (left side of the image) and further away from the slab (right side of the image). For the cases shown in Fig. 4.7, the

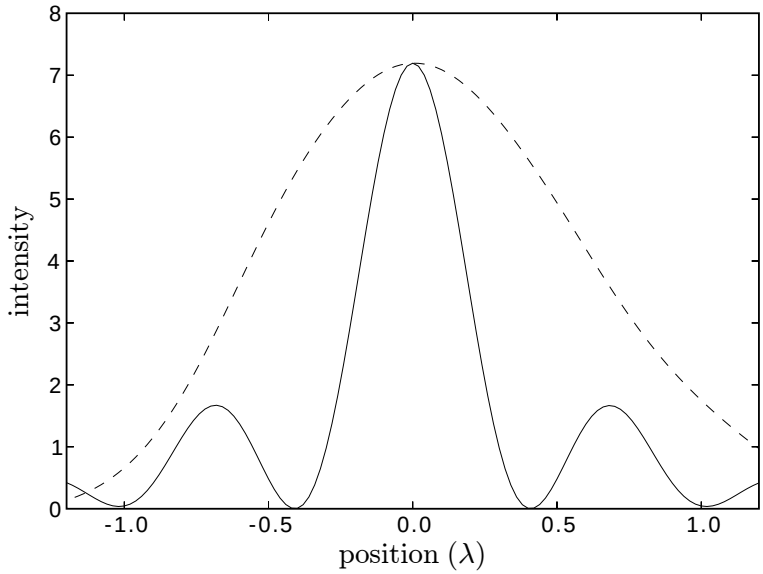

Figure 4.8: Electric field intensity distribution, plotted along the image center perpendicular (dashed line) and parallel (solid line) to the slab surface, for the 9-layer slab with $C = 0.5r$ (see Fig. 4.7f).

slab possesses mirror symmetry. In the literature it has been argued that the image strength is maximized if the slab possesses mirror symmetry and if the slab thickness is equal to an odd-integer number of $\lambda/4$ [174, 179]. Therefore, in Fig. 4.9 we compare the results for a slab with and without mirror symmetry. The external images look very similar. A comparison of the intensity maxima in the external images, shows indeed that the image formed by the slab with nine layers of air holes is brighter than the image formed by the 10-layer slab. However, the difference is small. Moreover, for both slabs also the spatial resolutions of the images, R_x and R_y are the same. Since our aim is to make a qualitative study of the light focussing by a photonic crystal slab, we do not optimize the termination to maximize the image intensity and the photonic crystal lens resolution.

4.2.3.2 Dependence on source/slab distance and slab thickness

We now study the dependence of the focussing properties of the photonic crystal lens on the source/slab distance L and the slab thickness D. The rules of geometric optics predict that when the source is closer to a negative index material slab, or the slab becomes thicker, the image distance L' increases. The image shift with respect to the change in L and D, strongly depends on the refractive index of the negative index material. For $\hat{n} = -1$, $L' = D - L$ (see Fig. 3.10).

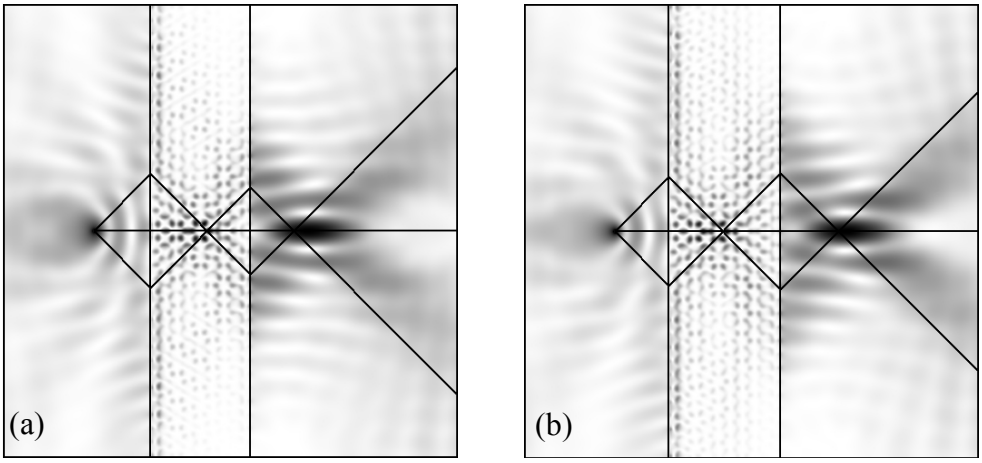

Figure 4.9: Same as Fig. 4.7. (a): $L = 1.25\lambda; N = 9, C = 0.5r$, so $D = 2.20\lambda$. (b): $L = 1.2\lambda; N = 10, C = 0.5r$, so $D = 2.52\lambda$.

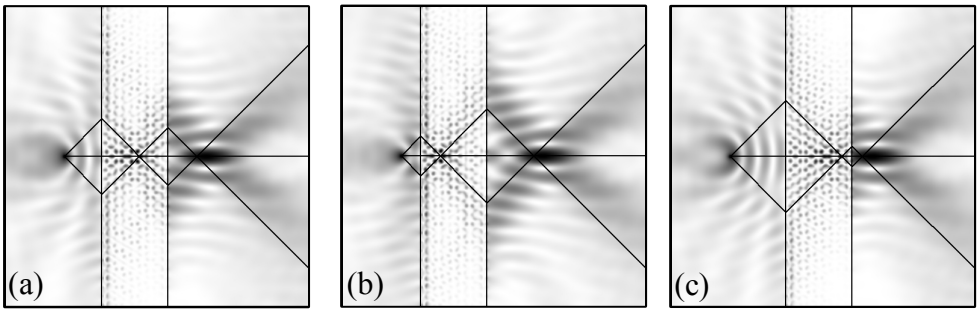

Figure 4.10: Same as Fig. 4.7f for: (a): $L = 1.25\lambda$. (b): $L = 0.65\lambda$. (c): $L = 1.85\lambda$.

Our earlier investigations have shown that the best image is obtained for surface terminations with $C = 0.5r$. Hence, we now only consider slabs having these surface terminations. Fig. 4.10a shows the electric field intensity $\mathbf{E}^2(\mathbf{r}, t)$ for a 2.20λ thick slab. The point source is placed at a distance $L = 1.25\lambda$ from the left surface of the slab. The image is formed at a distance $L' = 1.25\lambda$ from the slab. Note that in our simulation L' is determined by the position of the maximum of the electric field intensity $\mathbf{E}^2(\mathbf{r}, t)$ in the region to the right of the slab. Figures 4.10b,c show the results for displacements of the source so that $L = 0.65\lambda$ and $L = 1.85\lambda$, respectively. For the latter two cases $L' = 1.83\lambda$ and $L' = 0.67\lambda$, respectively. Hence, for all three cases we find $L + L' \neq D$ (see Table 4.1), indicating that $\hat{n} \neq -1$. This can also be observed by comparing the simulation results with the lines in Fig. 4.10, which indicate the direction of propagation according to Snell's law for a homogeneous isotropic

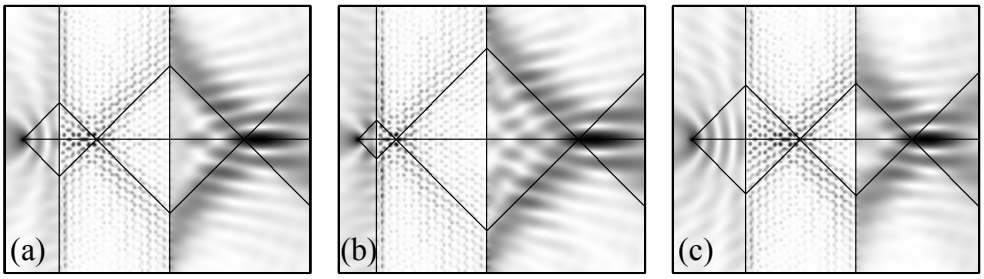

Figure 4.11: Same as Fig. 4.10 for $D = 3.76\lambda$ ($N = 15, C = 0.5r$).

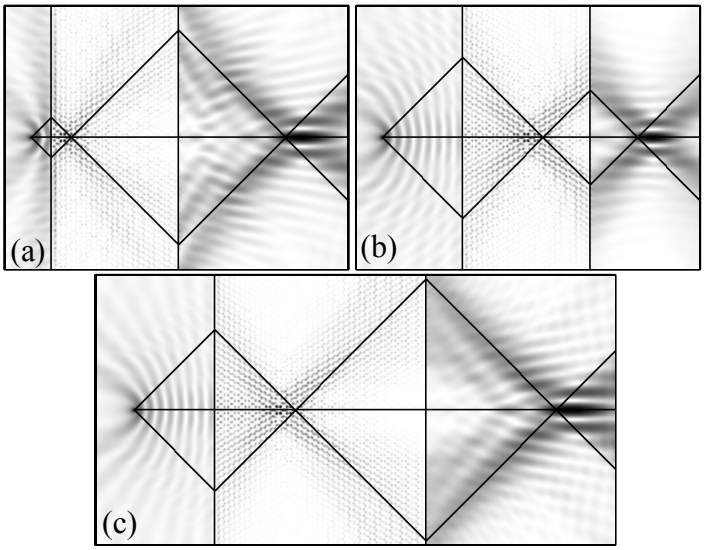

Figure 4.12: Same as Fig. 4.7 for (a): $L = 1.01\lambda; N = 25, C = 0.5r$, so $D = 6.34\lambda$. (b): $L = 4.01\lambda; N = 25, C = 0.5r$, so $D = 6.34\lambda$. (c): $L = 4.01\lambda; N = 41, C = 0.5r$, so $D = 10.51\lambda$.

slab with $\hat{n} = -1$. However, the agreement between our simulation results and the results from geometric optics is reasonably good.

We now increase the thickness of the slab to $D = 3.76\lambda$ and see what happens to the imaging behavior. The simulation results are shown in Fig. 4.11. The slab/source distances are the same as the ones used to obtain the results depicted in Fig. 4.10. We again find good agreement between our simulation results and the results obtained from the rules of geometric optics. Comparing Fig. 4.10a and Fig. 4.11a shows that when the slab becomes thicker, the image distance L' increases, as predicted by the rules of geometric optics.

From these observations, we can conclude that the dependence of the imaging behavior on

Table 4.1: Summary of the results presented in Figs. 4.10-4.12. L denotes the source/slab distance, D the slab thickness, L' the slab/image distance (see Fig. 4.10), R_x the longitudinal and R_y the transversal resolution.

$L\,(\lambda)$	$D\,(\lambda)$	$L'\,(\lambda)$	R_x	R_y	$L+L'\,(\lambda)$
0.65	2.20	1.83	1.34	0.42	2.48
1.25	2.20	1.25	1.34	0.42	2.50
1.85	2.20	0.67	1.34	0.42	2.52
0.65	3.76	3.63	1.90	0.46	4.28
1.25	3.76	2.99	1.90	0.46	4.24
1.85	3.76	2.41	1.56	0.42	4.26
1.01	6.34	6.07	2.00	0.46	7.08
4.01	6.34	3.05	1.60	0.42	7.06
4.01	10.51	7.12	2.06	0.50	11.13

the source/slab distance and the slab thickness follows the rules of geometric optics for a flat plate of negative index material with $\hat{n} \approx -1$ and embedded in vacuum. Hence, for some frequencies these photonic crystal slabs behave as a homogeneous effective medium with an effective refractive index of approximately -1. The deviation from $\hat{n} = -1$ does not become more prominent if we further increase the thickness of the slab, as can be observed from Fig. 4.12. However, from Table 4.1, which summarizes the results depicted in Figs. 4.10-4.12, it can be seen that the lens resolution of the thin slabs is better than that of the thick slabs. Also the intensity maximum in the external image decreases if the slab becomes thicker. The latter is due to the fact that the total transmission of light is reduced for thick slabs compared to thin slabs. This resolution and intensity dependence of the image on the thickness of the slab has also been observed in [175].

4.2.3.3 Internal image position

A careful study of the electric field intensity $\mathbf{E}^2(\mathbf{r}, t)$ inside the photonic crystal slab shows that the intensity displays minima in the air spheres and maxima in the high dielectric material. So, it is interesting to investigate what the effects on the imaging properties are, if according to the rules of geometric optics the internal focus is inside or outside an air sphere. For this purpose we consider a photonic crystal slab of width $D = 2.26\lambda$ ($N = 9, C = 0.25r$) and we place the point source at three different positions so that, according to the rules of geometric optics, the internal focus is created inside an air sphere and in between air spheres. As an example, we consider the internal focussing positions indicated by the numbers 1, 2 and 3 in Fig. 4.13a. To obtain focussing in points 1 and 2 we place the source at a distance $L = 1.14\lambda$ from the left surface of the slab. Taking $L = 1.05\lambda$ leads to an internal focus at position 3. We also move the source in the direction parallel to the slab surface in order to get the correct lateral position of the internal focus.

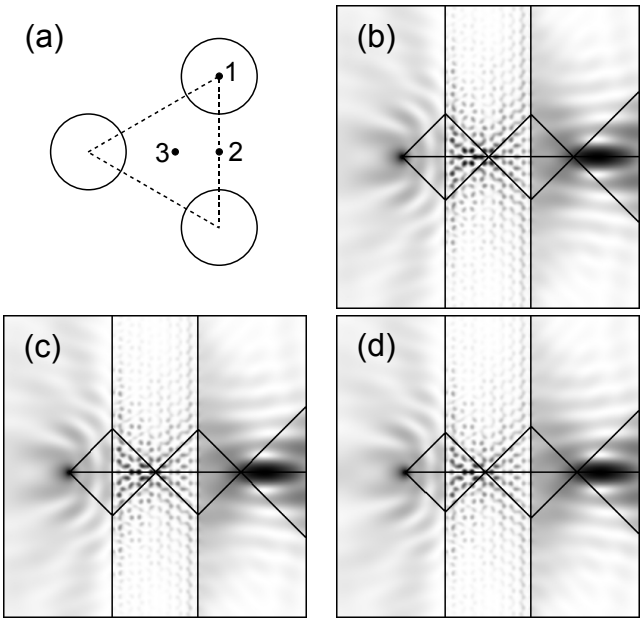

Figure 4.13: Same as Fig. 4.7 for $D = 2.26\lambda$ ($N = 9, C = 0.25r$). (a): Schematic picture of the internal focus positions. The internal focus at position 1 is inside an air sphere and the internal focus at positions 2 and 3 is inside the material with $\varepsilon = 12.96$. (b): $L = 1.14\lambda$, internal focus at position 1. (c): $L = 1.14\lambda$, internal focus at position 2. (d): $L = 1.05\lambda$, internal focus at position 3.

Figures 4.13b-d depict the electric field intensities $\mathbf{E}^2(\mathbf{r}, t)$ for internal focussing at position 1, 2 and 3, respectively. The lines indicate the direction of propagation according to Snell's law for the case of a homogeneous isotropic slab with $\hat{n} = -1$. Analysis of the position and the resolution of the external image shows that despite the different intensity profile and the different position of the internal image for the three cases, the external image is exactly the same for all three of them. This observation was also reported in [175]. Hence, the slab behaves as a homogeneous isotropic negative index material.

4.2.4 Imaging by a flat slab: two sources

As demonstrated in Section 4.2.3, for some frequencies a triangular lattice photonic crystal slab behaves in many respects as a slab made from a homogeneous effective medium with an effective refractive index of approximately -1 and thus operates as a negative-index lens. Therefore, it is of interest to study how far two identical point sources, positioned on a line parallel to the surface of the lens, have to be placed from each other, so that they can be observed as two separated images behind the lens. Fig. 4.14 depicts the electric field intensity $\mathbf{E}^2(\mathbf{r}, t)$ for a 2.26λ thick slab ($N = 9, C = 0.25r$). The two point sources are placed at a

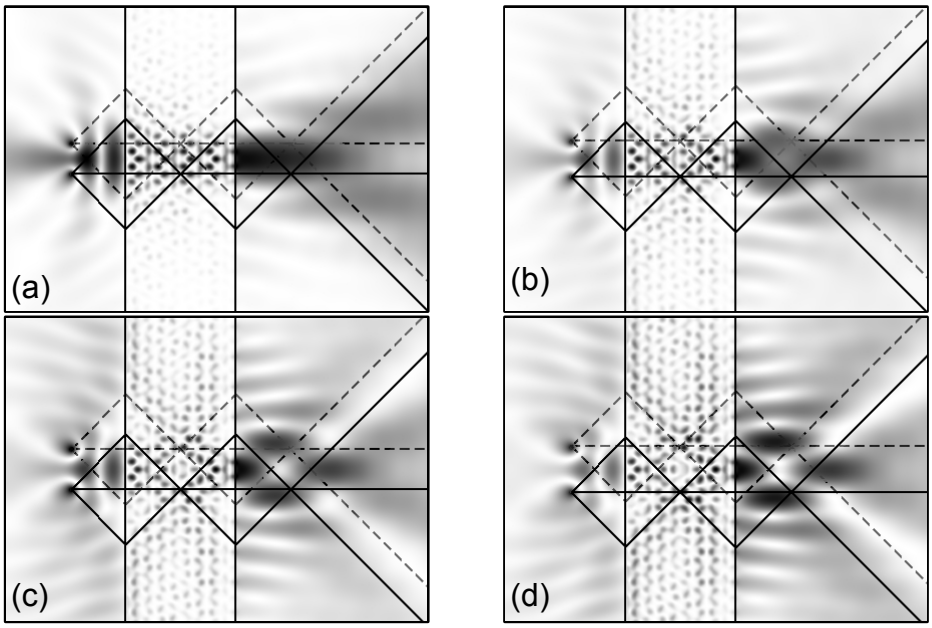

Figure 4.14: Same as Fig. 4.7 for $D = 2.26\lambda$ ($N = 9, C = 0.25r$) but now two point sources are placed in front of the surface at a distance $L = 1.14\lambda$. The two point sources are placed on a line parallel to the surface of the slab and are separated by a distance h from each other. (a): $h = 0.6\lambda$. (b): $h = 0.7\lambda$. (c): $h = 0.8\lambda$. (d): $h = 0.9\lambda$.

distance $L = 1.14\lambda$ from the left surface of the slab and are separated by a distance h varying from 0.6λ to 0.9λ. For $h \geq 0.8\lambda$ we can distinguish four high intensity regions behind the slab. These high intensity regions are placed on the corners of a diamond. The upper and lower regions can be identified as the images of the two point sources, as can be seen from the ray tracing analysis for a homogeneous isotropic slab with $\hat{n} = -1$. However, the other two "images" cannot be explained by the ray tracing analysis and are the result of constructive interference of the electromagnetic waves coming from the two point sources. As can be observed from Fig. 4.14, and also from the figures in Section 4.2.3, $\hat{n}$ is somewhat larger than -1. This results in the elongated images of the two sources. Comparing the images in Fig. 4.14 to, for example, the images in Fig. 4.7, it can be seen that the image of the upper (lower) source is moved upwards (downwards) with respect to the normal to the surface through the point source, while for the single-source case, the image of the source is centered around this normal. As a result, the distance between the images of the two sources is slightly larger than h. Also this effect is probably due to the constructive and destructive interference of the electromagnetic waves of the two sources.

In [171], a similar simulation was performed as the one presented in this subsection. In [171] it was found that for $h \geq 0.5\lambda$, the images of the two point sources can be observed as

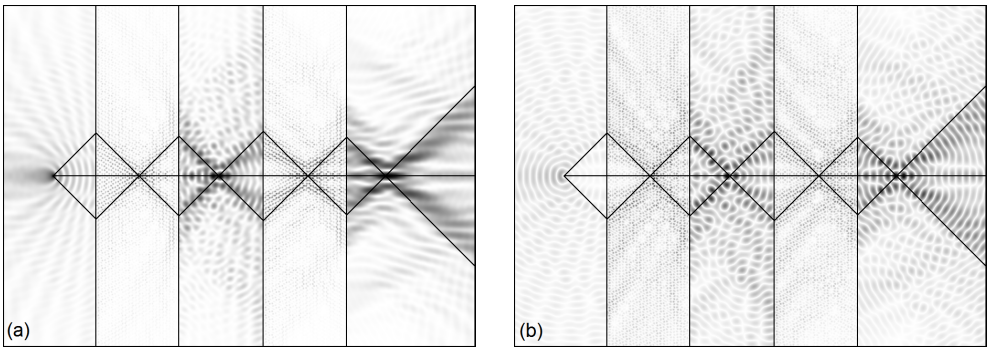

Figure 4.15: (a): Intensity of the electric field of a TM wave with frequency $f = 0.299$, generated by a point source placed in front of a cascaded stack composed of two photonic crystal slabs with an air layer in between. For the description of the imaging system we refer to the text. The lines indicate the propagation directions according to Snell's law for a homogeneous slab with $\hat{n} = -1$. Intensities are plotted on a $\log_{10}$ scale. The field intensities are scaled between 0 and 1 and are scaled differently for the regions to the left of the stack, in between the slabs, behind the stack and inside the slabs. (b): Amplitude of the electric field. The electric field amplitudes are plotted on a linear scale ranging from -1 to +1 and are scaled differently for the regions to the left of the stack, in between the slabs, behind the stack and inside the slabs.

two separate images. Hence, we find a spatial resolution that is worse compared to the one found in [171]. In order to find out the cause of this discrepancy we performed simulations with smaller values for the lattice spacing δ and the time step δt. These simulations give similar results as the ones presented here. Hence, we can conclude that the discrepancy has no numerical origin. However, in [171] it is not specified in detail how the point source is modeled and the method we use to model the point source is different from what is used in most FDTD simulations [20]. Maybe this is the reason for the difference in the results.

4.2.5 Image transfer by a cascaded stack[1]

Besides imaging by a flat lens, Notomi mentioned two other applications of negative index materials: Open cavity formation [3, 17] and image transfer by a cascaded stack of alternatively positioned, positive and negative refractive media [17]. Recently, an open cavity formed by three 60-degree wedges of a photonic crystal with a negative effective refractive index has been designed and studied [176–178]. In this section we study image transfer by a cascaded stack consisting of two and three two-dimensional photonic crystal slabs separated by air.

We consider photonic crystal slabs made of the same material as used in the previous subsections, that is made of a triangular lattice of air holes, drilled in a dielectric material with $\varepsilon = 12.96$, $\mu = 1$. The holes have a radius $r = 0.4a$. The photonic band structure

[1] Results of this section were published in Optics Express **14**, 879 (2006).

diagram for the TM mode is shown in Fig. 4.4. For the dimensionless frequency range $f = \omega a/2\pi c \in [0.26, 0.33]$, the EFS plots and the effective refractive index $\hat{n}$ as a function of the angle of the incoming wave vector $\mathbf{k}$ are shown in Fig. 4.5a and Fig. 4.5b, respectively. The cascaded stack is illuminated by a point source located at $\mathbf{r} = \mathbf{r}_0$ and modeled by Eq. (4.2). The point source is placed in front of the stack at a distance L from the most left air/photonic crystal interface. The location of the source is such that it is located at one of the E_z-points of the two-dimensional Yee grid (TM mode). As indicated by the step function in Eq. (4.2), the source is turned on at $t = 0$. In order to study the imaging properties of the cascaded stack we solve the time-dependent Maxwell equations by means of the FDTD method discussed in Chapter 2. We use rectangular simulation areas having boundaries that are absorbing. We employ a square grid with lattice spacing $\delta = 0.01\lambda$ and use a time step $\delta t = 0.001\lambda/c$. Firstly, we let the system evolve in time until a stationary state is reached and then we average the electric field intensity $\mathbf{E}^2(\mathbf{r}, t)$ over one period $2\pi/\omega$. We study the image quality from the electric field intensity distribution, plotted along the image center perpendicular (along the x-axis) and parallel (along the y-axis) to the air/photonic crystal slab interfaces. For reference, and because it is most frequently shown in the current literature, we also show the electric field amplitude $\mathbf{E}(\mathbf{r}, t)$.

Light propagating through a homogeneous isotropic slab with $\hat{n} = -1$ embedded in air is not reflected at the air/slab interfaces. For a slab made of a photonic crystal with an effective refractive index of $\hat{n} = -1$, the transmission of light is not 100% and strongly depends on the orientation of the photonic crystal slab and on the terminations of the air/photonic crystal interfaces. Transmission is maximal if the surface normal to the slabs is along the ΓM direction [196] and if the air holes at the air/photonic crystal interfaces are cut (see Section 4.2.3.1). We therefore consider photonic crystal slabs consisting of N layers of air spheres with cut air/photonic crystal interfaces normal to the ΓM direction. The cut area at both air/photonic crystal interfaces has a width $C = 0.5r$, resulting in the best image quality (see Section 4.2.3.1). Hence, the thickness of the slabs is given by $D = (N-1)\sqrt{3}a/2 + 0.4a$.

A flat plate of thickness D made of negative refractive index material with $n = -1$ and situated in vacuum can focus radiation from a point source P positioned at a distance $L < D$ from one side of the plate to a point P' located at a distance $L' = D - L$ from the other side of the plate [64]. Also inside the plate an image is formed. Due to the relation $L + L' = D$, the distance between P and P' is always equal to $2D$. Hence, to increase the distance between P and P' there are two possibilities: Increasing D or applying the principle of image transfer by a cascaded stack. If the flat plates are made of a photonic crystal with an effective refractive index $\hat{n} = -1$, only one option is feasible: Taking one photonic crystal slab and increasing its thickness leads to worsening spatial resolutions of the image that is formed behind the slab.

In order to have photonic crystal slabs with $\hat{n} \approx -1$, we consider a source, emitting TM

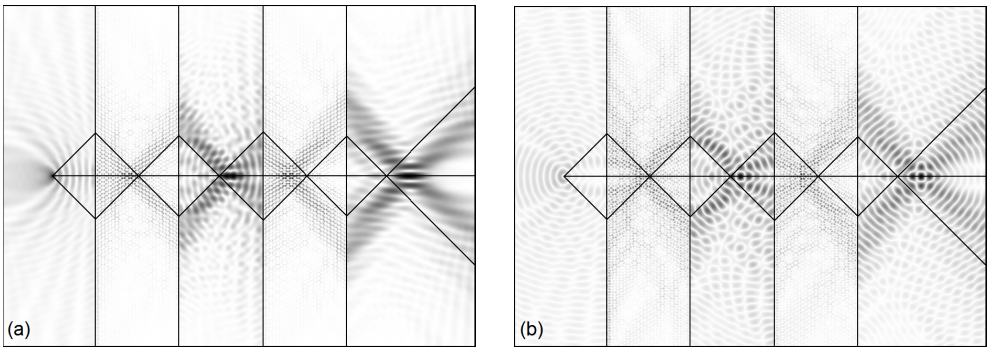

Figure 4.16: Same as Fig. 4.15 for $f = 0.300$.

waves with a frequency $f = 0.299$ (see Fig. 4.5). We first consider a cascaded stack composed of two photonic crystal slabs with thickness $D = 6.33\lambda$ ($N = 25$). The slabs are separated by an air layer of thickness 6.43λ. The source is placed at a distance $L = 3.29\lambda$ from the left surface of the first photonic crystal slab. Figures 4.15a and b depict the electric field intensity $\mathbf{E}^2(\mathbf{r}, t)$ and amplitude $\mathbf{E}(\mathbf{r}, t)$, respectively. The material structure of the photonic crystal slab is not shown in order to give a better image of the light focusing inside the slabs. The lines indicate the direction of propagation according to Snell's law for the case of a homogeneous isotropic slab with $\hat{n} = -1$. From Fig. 4.15a it can be seen that there is a relatively good agreement between our simulation results and the results obtained from the rules of geometric optics. Light focusing occurs inside the slabs, in between the two slabs and behind the two slabs. The focus behind the two slabs is not circular, but elongated in the direction of propagation. This we already have observed in Section 4.2.3 and is due to slight deviations of $\hat{n}$ from -1 for different angles of incidence. Hence, we do not observe point focusing and in a strict sense, there is no image formation. However, we can say we observe image formation with some aberrations. The spatial resolutions of the image behind the second slab are $R_x = 1.76$ and $R_y = 0.46$. As can be clearly seen from Fig. 4.15a, this image is different from the image in between the two slabs. However, if we remove the second slab and repeat the same calculation, then an image with the same spatial resolutions is formed (results not shown). Hence, the first image (behind the first slab) is transferred through the second slab, so that the second image (behind the second slab) is a copy of the first image. The first image gets distorted by reflections from the second slab. This would not happen in the ideal case, that is in the case of two slabs made of a homogeneous isotropic material with $\hat{n} = -1$. Note that the picture of the electric field amplitude (see Fig. 4.15b) suggests a more circular image that is transferred by the cascaded stack, and thus indicates better imaging properties of the slabs. However the picture of the electric field amplitude displays only a snapshot. Moreover, it is not sufficient to study field amplitudes in order to investigate the imaging properties of a photonic crystal system, since they cannot be measured directly.

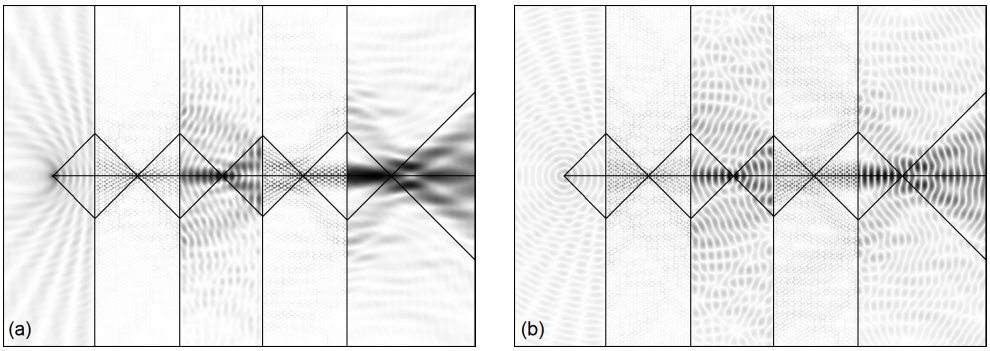

Figure 4.17: Same as Fig. 4.15 for air/photonic crystal interfaces that are not cut.

The imaging properties of the cascaded stack are very sensitive to the frequency of the source and the surface terminations of the photonic crystal slabs. Fig. 4.16 shows the electric field intensity and amplitude for the same setup as the one that was used to obtain the results displayed in Fig. 4.15 but for the frequency $f = 0.300$. For this frequency images are also formed inside the slabs, in between the two slabs and behind the two slabs, but the deviations from propagation through a homogeneous isotropic slab with $\hat{n} = -1$ is much larger than for $f = 0.299$, as indicated by the propagation lines obtained from Snell's law. Moreover, the image formed behind the two slabs is no longer an exact copy of the image formed behind the first slab. The spatial resolution changes from $R_x = 1.60$, $R_y = 0.42$ for the first image to $R_x = 1.70$, $R_y = 0.42$ for the second image. Hence, for this particular case additional longitudinal aberrations are induced by the second slab. Note however, that the spatial resolutions of the image formed behind the second slab in Fig. 4.16a are better than the ones of the image formed behind the second slab in Fig. 4.15a. Figure 4.17 shows the electric field intensity $\mathbf{E}^2(\mathbf{r}, t)$ and amplitude $\mathbf{E}(\mathbf{r}, t)$ for the same setup as the one that was used to obtain the results displayed in Fig. 4.15 but the air/photonic crystal interfaces of the slabs are not cut. It is clearly seen that in this case no image transfer by the cascaded stack can be observed.

Another important issue is the irradiance of the images. If we normalize the maximum of the source intensity to 100%, then, for the case studied in Fig. 4.15, the intensity maximum in the first slab corresponds to 7.7%, in between the two slabs to 1.8%, inside the second slab to 1.7% and behind the second slab to 0.7%. Similar simulation results for a cascaded stack with two photonic crystal slabs with $N = 15$, show that the intensity maximum in the first slab corresponds to 7.0%, in between the two slabs to 3.8%, inside the second slab to 2.6% and behind the second slab to 1.3%. Hence, even for cascaded stacks with thin photonic crystal slabs the maximum of the transmitted intensity is rather low. This observation is in agreement with the observation that the maximum coupling coefficient between a plane wave in air and the Bloch wave in the photonic crystal is only about 65% and rapidly decreases

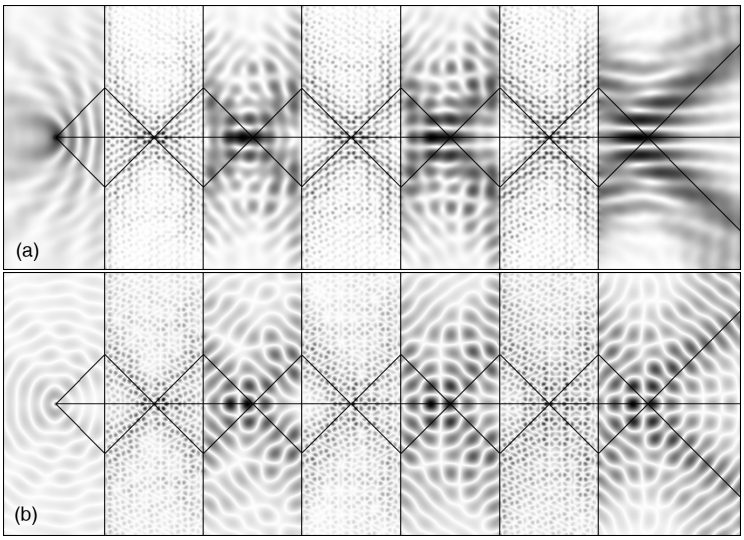

Figure 4.18: Same as Fig. 4.15 for a cascaded stack with three photonic crystal slabs. For the description of the imaging system we refer to the text.

for angles of incidence larger than $30°$, for an air/photonic crystal interface normal to the ΓM direction [196]. Additional simulations (results not shown) show that the intensity in the images depends on the thickness of the slabs, the frequency and the size of the cut area at the surface terminations. However, for all cases studied the intensities were of the same order as mentioned before.

In order to investigate the dependence of the maxima of the transmitted intensity on the number of slabs in the stack, we consider a cascaded stack composed of three photonic crystal slabs with thickness $D = 3.74\lambda\,(N = 15)$. The photonic crystal slabs are separated by air layers of the same thickness as the slabs. The source is placed at a distance $L = 1.87\lambda$ from the left surface of the first photonic crystal slab. Figure 4.18 depicts the electric field intensity. The intensity maximum in the first slab corresponds to 6.6%, in between slab 1 and slab 2 to 3.6%, in the second slab to 3.3%, in between slab 2 and 3 to 1.5%, in the third slab to 1.6% and behind the third slab to 0.7%. Hence, for cascaded stacks with three photonic crystal layers with $N = 15$, our simulations show that the maximum of the intensity behind the last slab decreases, compared to the case of a cascaded stack with only two photonic crystal slabs: For three slabs, the maximum of the intensity behind the last slab corresponds to 0.7%, while for the two slab case it corresponds to 1.3%, as shown before. Similar simulations with one single slab show that for a single slab the maximum of the transmitted intensity corresponds to 3.4%. These results indicate that each slab that is added to the stack reduces the intensity by a factor of two. In this particular case, additional longitudinal aberrations are induced by each slab that is added to the stack. The transversal spatial resolution of the image remains

approximately the same upon transfer of the image through the stack.

To summarize, in order to increase the source/image distance in flat slab imaging, which is limited to two times the thickness of the slab, one could use one thick slab or a cascaded stack consisting of several thinner slabs separated by air. If the slabs are made of a photonic crystal material, using one thick slab is not an option, since the image resolution becomes worse as the thickness increases. In this section we have demonstrated the working principle of image transfer by a cascaded stack consisting of two and three photonic crystal slabs separated by air. The quality of the image transferred by the stack and the maximum of the transmitted intensity depends on the frequency of the light, the thickness of the photonic crystal slabs, the surface termination of the photonic crystal slabs and on the distance between the slabs. Although the transmitted intensity is rather low for cascaded stacks consisting of two photonic crystal slabs, it seems that more slabs can be added without a further significant decrease of the intensity. The image transfer over a given distance requires the solution of an optimization problem, involving the number of slabs in the stack, the thickness of the slabs, the distance between the slabs and the frequency of the light.

4.3 Conclusions

In this chapter we have shown that for some frequencies negative refraction can be observed in triangular lattice photonic crystals. We have considered both photonic crystal structures made from dielectric cylindrical pillars organized in a triangular lattice and photonic crystal structures made from a dielectric material with circular holes drilled in a triangular lattice configuration. Since only the latter photonic crystal structure can have an effective refractive index $\hat{n} \approx -1$, we have used those structures to study the lensing mechanism. We have shown that for some frequencies a photonic crystal slab consisting of a dielectric medium with circular holes drilled in a triangular lattice configuration behaves in many respects as a slab made from a homogeneous effective medium with an effective refractive index of approximately -1 and thus operates as a negative-index lens. Since $\hat{n}$ slightly deviates from -1 for different angles of incidence, the image of a point source, formed behind the photonic crystal slab, is not circular but elongated in the direction of propagation. Hence, in a strict sense we did not observe image formation. However, we can say that we did observe image formation with some aberrations. The spatial resolution in the direction of propagation is larger than the wavelength λ of the light, but the spatial resolution of the image in the direction perpendicular to the direction of propagation is smaller than $\lambda/2$. Hence, only in the direction perpendicular to the direction of light propagation, a subwavelength resolution of the image could be achieved. We also have demonstrated that the images of two identical point sources separated by a lateral distance $h \geq 0.8\lambda$ and placed in front of a photonic crystal lens with $\hat{n} \approx -1$ can be resolved.

Another important difference between such a photonic crystal lens and a negative-index lens is that at the surfaces of the photonic crystal lens most of the light is reflected, while no reflection occurs for a negative-index lens with $\hat{n} = -1$. Hence, using the photonic crystal lens causes a tremendous loss in light intensity. Despite of this, we have shown that image transfer by a cascaded stack, consisting of two and three triangular lattice photonic crystal slabs separated by a layer of air, is feasible.

Chapter 5

Focussing light in square lattice photonic crystals

In the previous chapter we have shown that the phenomena of negative refraction and superlensing can occur in photonic crystals with triangular lattice symmetry and that the phenomena are due to a negative effective refractive index. However, negative refraction can only be obtained for frequency ranges in the upper photonic bands. For these relative high frequencies, the absolute value of the effective refractive index is smaller than one. Just as in the case of propagation of light through a homogeneous isotropic slab of material with refractive index $n < 1$, total internal reflection can be expected for a large range of angles of incidence (see Section 3.1.6). As a result, the intensity of the transmitted light can be rather low. Obtaining negative refraction at lower frequencies in the photonic band structure diagram would therefore be more desirable for the fabrication of a superlens.

Luo *et al.* demonstrated that negative refraction for beams of all incident angles from air, a phenomenon which they define as all-angle negative refraction (AANR), can be obtained at the lowest band of planar photonic crystals with square lattice symmetry [179]. However, this band has a positive refractive index [179]. Based on the phenomena of all-angle negative refraction, Luo *et al.* designed and numerically demonstrated a microsuperlens [179]. As discussed in Section 3.3.2, this type of microlens has been subject of debate. In this chapter we study the negative refraction in photonic crystals with square lattice symmetry in more detail. We present finite-difference time domain (FDTD) simulation results for the propagation of light in planar photonic crystals with square lattice symmetry. We use the FDTD techniques described in Chapter 2 to investigate the space and time evolution of the electromagnetic waves. Photonic band structure diagrams and EFS plots are obtained using the MIT Photonic-Bands software [190].

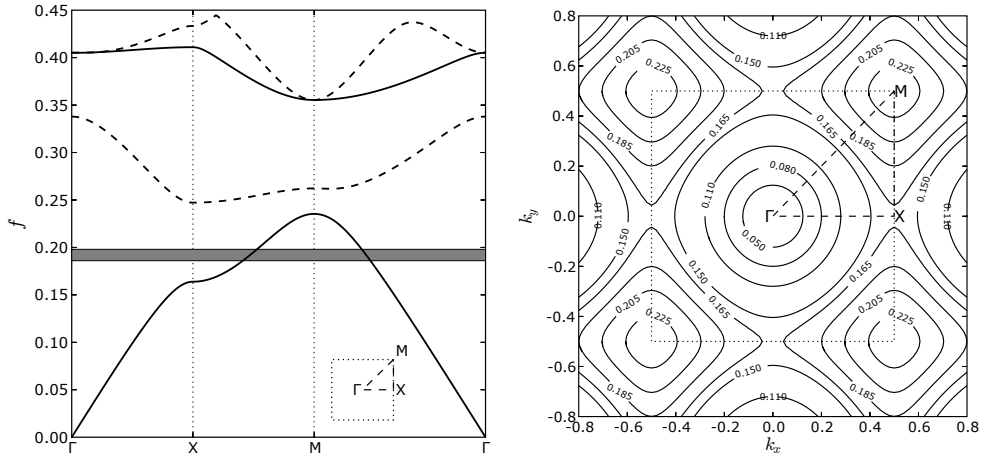

(a) (b)

Figure 5.1: (a): Photonic band structure diagram of TE modes for a two-dimensional photonic crystal consisting of a dielectric medium ($\varepsilon = 12, \mu = 1$) with holes of radius $r = 0.35a$ drilled in a square lattice configuration with lattice constant a. The AANR frequency range is highlighted in grey. (b): EFS plot for the frequency range $f = \omega a/2\pi c \in [0.05, 0.225]$ corresponding to band 1 of Fig. 5.1a. The first Brillouin zone (dotted line) of a square lattice and the symmetry points are also shown (see Appendix A).

5.1 Circular air holes in dielectric material

In this section, we study photonic crystal structures made of dielectric material with circular holes drilled in a square lattice configuration. If not mentioned otherwise, we use $\varepsilon = 12$ for the dielectric constant, $\mu = 1$ and $r = 0.35a$ for the hole radius, where a denotes the lattice constant. This allows us to compare some of our results to the results presented in [179].

5.1.1 Photonic band structure diagram and EFS plots

The photonic band structure diagram for the TE mode is shown in Fig. 5.1a. For the dimensionless frequency range $f = \omega a/2\pi c \in [0.05, 0.225]$, corresponding to frequencies in band 1, the EFS plot is depicted in Fig. 5.1b. Based on this EFS plot, Luo *et al.* found a frequency range so that for all incident angles one obtains only a single negative-refracted beam, a phenomenon they defined as all-angle negative refraction (AANR) [179]. Single-beam AANR can be realized if the following conditions are fulfilled [179]:

1. EFSs of the photonic crystal are convex.

2. EFSs of the photonic crystal are larger than the one of air.

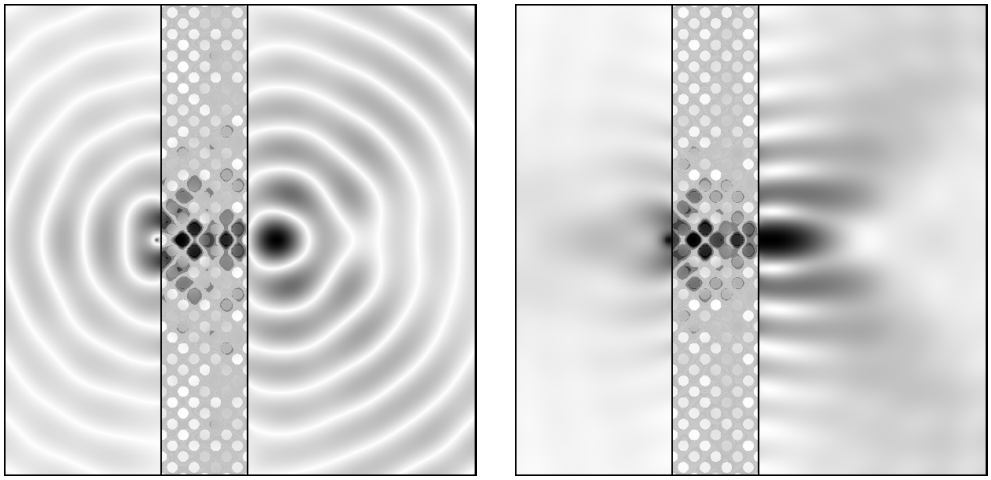

(a) (b)

Figure 5.2: (a): Amplitude of the magnetic field (H_z) of a TE wave emitted by a point source placed at a distance $L = 0.35a = 0.07\lambda$ from the left-hand surface of a (11)-oriented slab of a photonic crystal made of a square lattice of holes in a dielectric medium with $\varepsilon = 12, \mu = 1$, lattice constant a and hole radius $r = 0.35a$. The slab has a thickness $D = 4\sqrt{2}a = 1.10\lambda$. The snapshot is taken at $t = 23.4\lambda/c$. The amplitude is plotted on a linear scale ranging from -1 to +1 and is scaled differently for the regions to the left and right of the slab and inside the slab. (b): Intensity of the magnetic field. The field intensity is plotted on a $\log_{10}$ scale. The intensity is scaled between 0 and 1 and is scaled differently for the regions to the left and right of the slab and inside the slab.

3. The frequency should be smaller than $0.5 \times 2\pi/a_s$, where a_s is the surface period.

Conditions 1 and 2 are required if beams with any incident angle need to be refracted negatively and the third condition is necessary to have single beam behavior [179]. However, as pointed out in [18], condition 3 guarantees that, if electromagnetic waves are incident in the photonic crystal from air, any higher order Bragg reflected beams for any angle of incidence are absent. In general, the presence of only a single reflected beam is neither a prerequisite nor does it guarantee the presence of a single beam coupling into the photonic crystal medium. Hence, condition 3 does not guarantee single-beam refraction [18]. However, following the criteria for single-beam AANR of Luo *et al.*, there are two frequency regions for which single beam AANR is possible [179]. The largest one ranges from $f = 0.186$ to $f = 0.198$, indicated by the grey region in Fig. 5.1.

5.1.2 Imaging by a flat lens

Using the phenomenon of single beam AANR, Luo *et al.* designed a microsuperlens [179]. Ideally, such a superlens can focus a point source at one side of the lens into a real point

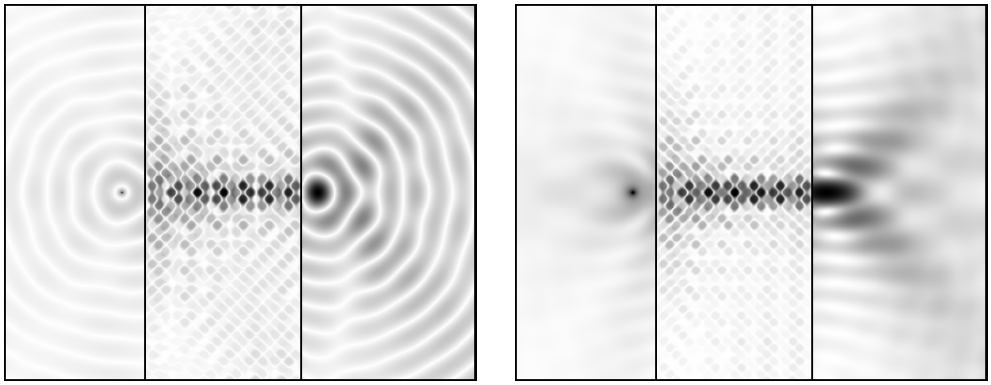

(a) (b)

Figure 5.3: Same as Fig. 5.2 for $D = 12\sqrt{2}a = 3.31\lambda$ and $L = 0.5\lambda$. The snapshot of the magnetic field amplitude (a) is taken at $46.0\lambda/c$.

image on the other side, even for the case of a parallel-sided slab of material [64, 81]. We repeat the simulations as described in [179].

The superlens is modelled by a (11)-oriented slab of the photonic crystal, that is the air-photonic crystal interface is perpendicular to the ΓM direction. The slab thickness is $D = 4\sqrt{2}a = 1.10\lambda$, that is the slab contains in the horizontal direction 7 layers of complete circular holes and the front and back layers consist of half circular holes, as can be seen from Fig. 5.2. The thickness and surface termination of the slab is chosen to minimize reflection [179]. This is accomplished by requiring the slab to posses both mirror symmetry and a thickness equal to an integer multiple of half the wavelength of the light in the slab [179]. As discussed in Section 4.2.3.1, cutting the interface of the photonic crystal slab can lead to a better image with a higher intensity [122, 174, 208, 209]. For some cuts, surface waves at the interface can be excited [122, 208, 209] and they can enhance the transmission. The total simulation area has dimensions $L_x = 8\lambda$ and $L_y = 6\lambda$. The boundaries of the simulation area are absorbing. We discretize space in a square grid with lattice spacing $\delta = 0.005\lambda$. This results in a total number of 1920000 lattice points. In our simulations we use a time step $\delta t = 0.0005\lambda/c$.

A point source modeled by

$$\mathbf{M}(\mathbf{r}, t) = \mathbf{O}\,\theta(t)\delta(\mathbf{r} - \mathbf{r}_0)\sin\Omega t, \tag{5.1}$$

where Ω is the angular frequency of the source and $\mathbf{O}$ defines the direction of the magnetic current, is placed at a distance $L = 0.35a = 0.07\lambda$ from the left-hand surface of the photonic crystal slab. The source is placed in front of one of the half circular air holes, as can be seen from Fig. 5.2. The source starts emitting at $t = 0$ a TE wave of dimensionless frequency $f =$

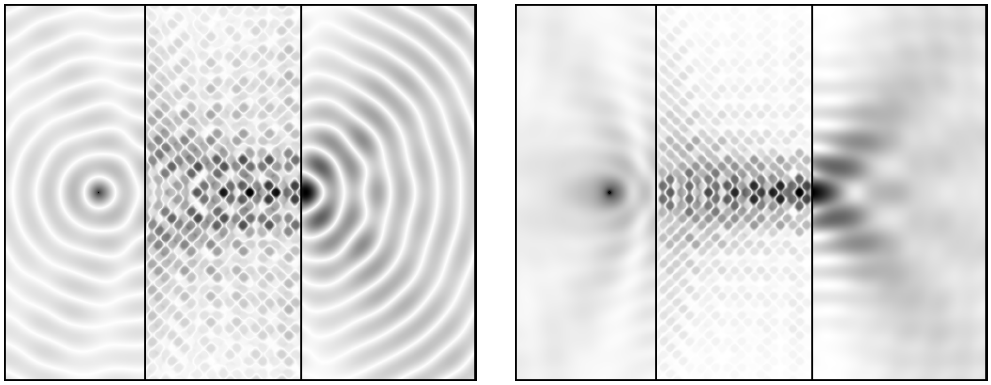

(a) (b)

Figure 5.4: Same as Fig. 5.3 for $L = 1.0\lambda$. The snapshot of the magnetic field amplitude (a) is taken at $43.7\lambda/c$.

0.195, chosen to lie within the AANR frequency range indicated in Fig. 5.1. We investigate the space and time evolution of the emitted electromagnetic waves. The simulation results at $t = 23.4\lambda/c$ are depicted in Fig. 5.2a. A "point" image can be observed at the right-hand side of the superlens, as described in [179]. Although we are able to obtain a similar result as the one presented in [179], we want to point out here that the snapshots depend significantly on the simulation time and that in [179] it is not mentioned at which time the snapshot is taken.

Although we find a similar simulation result as the one presented in [179], we cannot conclude on the basis of this single result that the photonic crystal slab behaves as a lens. In order to make this conclusion, additional imaging properties of the photonic crystal slab must be investigated, such as for example the dependence of the image position on the position of the source and the thickness of the slab (see Section 4.2.3.2). Moreover, as demonstrated in the previous chapter, it is not sufficient to study field amplitudes in order to investigate the imaging properties of a photonic crystal system, since they cannot be measured directly. Therefore, we show both the results for the field amplitude and the field intensity.

Figure 5.2b shows the magnetic field intensity $\mathbf{H}^2(\mathbf{r}, t)$ corresponding to the magnetic field amplitude $\mathbf{H}(\mathbf{r}, t)$ depicted in Fig. 5.2a. From Fig. 5.2b it can be seen that the image formed behind the slab is not circular and not well-separated from the right slab interface. This is in contrast to the point-like "image" in Fig. 5.2a. Moreover, for a negative index material lens the rules of geometric optics predict that also focussing of the electromagnetic wave inside the photonic crystal slab should be observed. Neither the results depicted in Fig. 5.2a nor the results depicted in Fig. 5.2b provide evidence for focussing inside the slab. Because the slab in Fig. 5.2 might be too thin to observe the internal focus, we repeat the same simulations for a slab of thickness $D = 12\sqrt{2} = 3.31\lambda$ and for a source placed at a distance $L = 0.5\lambda$ from the left surface of the slab. The results are shown in Fig. 5.3. Also for this thick slab no

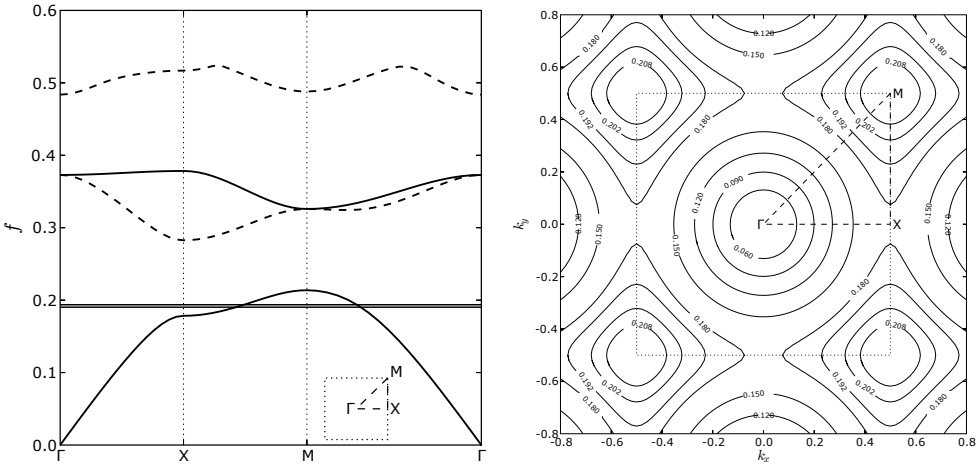

(a) (b)

Figure 5.5: (a): Photonic band structure diagram of TM modes for a two-dimensional photonic crystal made from dielectric rods ($\varepsilon = 14, \mu = 1$) with radius $r = 0.3a$ positioned in a square lattice with lattice constant a. The AANR frequency range is highlighted in grey. (b): EFS plot for the frequency range $f = \omega a/2\pi c \in [0.06, 0.208]$ corresponding to band 1. The first Brillouin zone (dotted line) of a square lattice and the symmetry points are also shown (see Appendix A).

internal focus is seen. Instead, it seems that after entering the slab the wave is first collimated and then travels across the slab as if it is travelling inside a waveguide.

Apart from the internal focus, the rules of geometric optics also predict that when a source moves further away from a negative index material slab, the image distance decreases (see Fig. 3.10). In order to observe the displacement of the image, we repeat the same simulation as the ones to obtain the results depicted in Fig. 5.3 but for a source/slab distance $L = 1\lambda$. The results are shown in Fig. 5.4. Comparing Fig. 5.3 and Fig. 5.4 shows that the image moves indeed closer to the slab if the source is placed further away from the slab. Solely based on this results, one could conclude that the photonic crystal slab behaves as a lens. Note however that compared to the triangular-lattice photonic crystal slab (see Chapter 4), it is impossible to obtain an image that is well-separated from the slab.

Based on all previous observations, we conclude that the photonic crystal slab consisting of dielectric rods arranged in a square lattice does not behave as a negative-index lens. This confirms the observations made in previous works [66, 183]. The so-called "imaging" properties of the slab are not due to negative refraction.

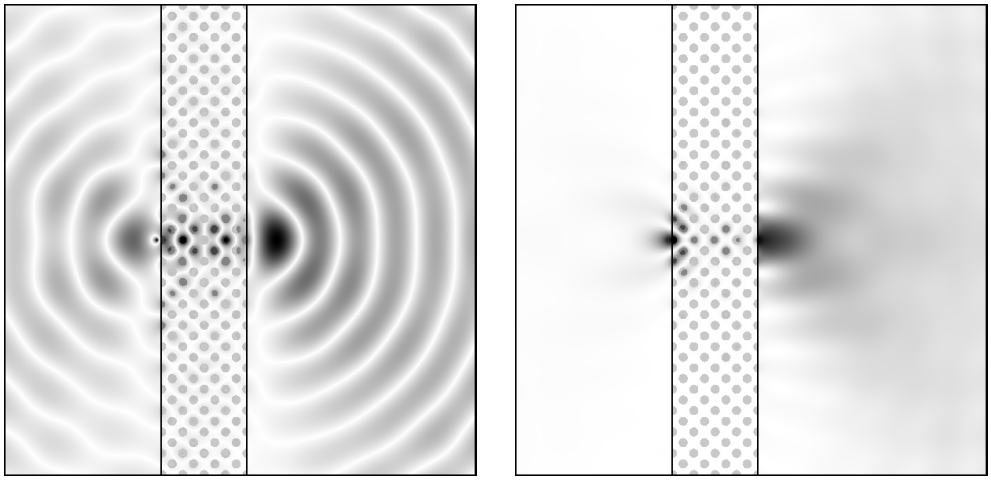

(a) (b)

Figure 5.6: (a): Amplitude of the electric field (E_z) of a TM wave emitted by a point source placed at a distance of $L = 0.3a = 0.06\lambda$ from the left-hand surface of a (11)-oriented slab of a photonic crystal made of a square lattice of photonic crystal made from dielectric rods ($\varepsilon = 14, \mu = 1$) with radius $r = 0.3a$ positioned on a square with lattice constant a. The slab has a thickness $D = 4\sqrt{2}a = 1.09\lambda$. The snapshot is taken at $t = 23.4\lambda/c$. The amplitude is plotted on a linear scale ranging from -1 to +1 and is scaled differently for the regions to the left and right of the slab and inside the slab. (b): Intensity of the electric field. The intensity is plotted on a $\log_{10}$ scale. The intensity is scaled between 0 and 1 and is scaled differently for the regions to the left and right of the slab and inside the slab.

5.2 Dielectric circular rods in air

In this section we study a square lattice photonic crystal structure of dielectric cylindrical pillars in air. If not mentioned otherwise we use the parameters $\varepsilon = 14, \mu = 1, r = 0.3a$, where a is the lattice constant. This allow us to compare some of our results to the results presented in [179].

5.2.1 Photonic band structure diagram and EFS plot

The photonic band structure diagram for the TM mode and the EFS plot for some frequencies in the first band are shown in Fig. 5.5a and Fig. 5.5b, respectively. A single-beam AANR region of about 3.5% near $f = 0.192$ [179] is indicated by the grey region in Fig. 5.5.

5.2.2 Imaging by a flat lens

Using the phenomenon of single-beam AANR, Luo *et al.* also designed a superlens based on this photonic crystal structure. We repeat the simulation as described in [179]. The photonic

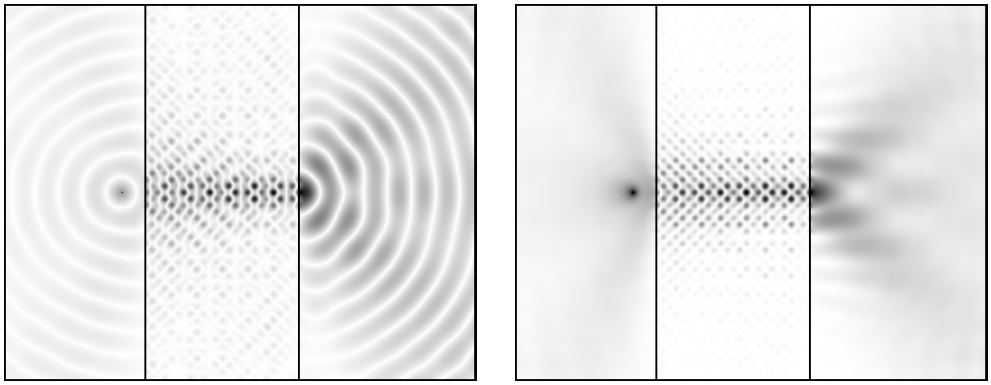

(a) (b)

Figure 5.7: Same as Fig. 5.6 for $D = 12\sqrt{2}a = 3.26\lambda$ and $L = 0.5\lambda$. The snapshot of the electric field amplitude (a) is taken at time $t = 43.7\lambda/c$.

crystal slab and the simulation area have the same dimensions as described in Section 5.1.2. A point source emitting a TM wave of dimensionless frequency $f = 0.192$, is placed at a distance $0.3a$ from the left-hand surface of the photonic crystal slab, as can be seen from Fig. 5.6.

Figure 5.6a shows the FDTD simulation results for the electric field amplitude $\mathbf{E}(\mathbf{r}, t)$ at $t = 23.4\lambda/c$. Also for this case there is good agreement with the results presented in [179]. From the electric field intensity (see Fig. 5.6b) it can be seen that also for this photonic crystal slab the image formed behind the slab is not well-separated from the slab interface and again no internal focus is observed.

Fig. 5.7 shows the simulation results for a slab with thickness $D = 12\sqrt{2}a = 3.26\lambda$ and for a source placed at a distance $L = 0.5\lambda$ from the left surface of the slab. Also for this thick slab no internal focus can be seen. Instead, after entering the slab, the wave is slightly collimated and then travels across the slab as if it is travelling inside a waveguide. For this case the collimation is much less pronounced as for the photonic crystal slab described in Section 5.1.2 (see Fig. 5.3). It seems that a guiding channel is formed that connects the source with the near-field image. The latter phenomenon was also reported in [181]. Furthermore, in [181] it was observed that the width of this guiding channel increases if the source/slab distance increases. Therefore, in Fig. 5.8 we show the simulation results for the same set-up as the one to obtain the results presented in Fig. 5.7, but now we place the source at a distance $L = 1\lambda$ from the left surface of the photonic crystal slab. As can be seen from Fig. 5.8, the width of the guiding channel indeed increases if the source/slab distance increases. Moreover, instead of one image at least two near-field images can be observed. This means that the photonic crystal slab is not focussing at all. Hence, also the photonic crystal slab consisting of a dielectric

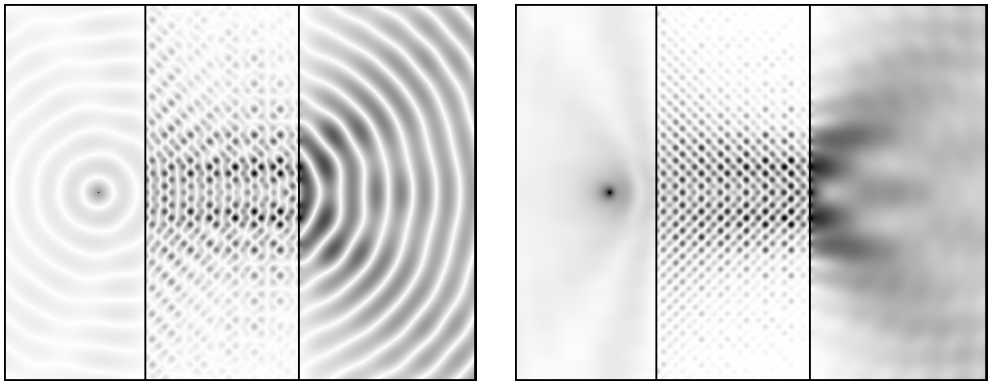

(a) (b)

Figure 5.8: Same as Fig. 5.7 for $L = 1.0\lambda$. The snapshot of the electric field amplitude (a) is taken at time $t = 43.7\lambda/c$.

medium with holes drilled in a square lattice configuration does not behave as a negative index lens. This also confirms the observations made in previous works [66, 181, 182, 184–189].

5.3 Conclusions

In this chapter we have shown that neither photonic crystal slabs made from dielectric cylindrical pillars organized in a square lattice nor photonic crystal slabs made from a dielectric material with circular holes drilled in a square lattice configuration behave as a negative-index lens. The imaging effects, which have been previously interpreted as a signature of negative refraction, can only be observed for sources placed in the vicinity of the slab. Moreover, the so-called “image” is always formed right behind the slab.

Chapter 6

Control of spontaneous emission in photonic crystals

In chapters 4 and 5 we have studied the phenomena of negative refraction and the focusing of light by two-dimensional photonic crystals. In this chapter we focus on another interesting optical property of photonic crystals, namely their ability to control the spontaneous emission of defects inside the photonic crystal.

6.1 Spontaneous emission of light

Spontaneous emission of light is a widely studied phenomenon, both due to its importance in the fundamental understanding of light-matter interactions and in the applications, such as for example transistors, optical switches, microlasers, solar cells, . . ., which depend on it. As early as in 1946, it was noticed that spontaneous emission can be controlled with cavity structures [210]. Theoretically, the spontaneous emission rate can be obtained from Fermi's golden rule containing the local radiative density of states (LRDOS) [211]. For relatively simple cavity structures, the modification of the spontaneous emission rate can be calculated analytically using either a classical [212–218] or a quantum mechanical approach [219–232]. It has been shown that the classical and quantum mechanical results for the spontaneous emission are equivalent [212, 213, 215, 217, 218, 232]. This equivalence allows the calculation of the spontaneous emission rate [233–235], the external quantum efficiency [235] and the spontaneous emission factor [235, 236] in a microcavity of arbitrary geometry, using a finite-difference time domain (FDTD) algorithm [20].

Control of spontaneous emission is also one of the main applications of photonic crystals [4]. It was suggested that complete photonic band gaps allow complete inhibition of spontaneous emission for frequencies deep inside the photonic band gap [4]. Also photonic band gap materials that do not possess complete photonic band gaps but pseudogaps are of interest, since they can allow for a substantially suppressed spontaneous emission. In the early experimental studies on the variation of spontaneous emission in photonic crystals [237–242], the light sources were dye molecules. Theoretical calculations have shown that the effect of the photonic band gap on the fluorescence lifetime of the dye molecules in these structures was very small and that the experimentally measured variations in lifetime were mainly caused by other processes such as electronic/chemical interactions between the molecules and the medium [243]. In 2002, Koenderink *et al.* made the first observation of the inhibition of spontaneous emission in a photonic crystal consisting of a FCC crystal of air spheres in Titania [244]. They demonstrated that in their experiment the reduction in the emitted power was not due to chemical interactions of the dye with its environment. An experiment in the same spirit showed the inhibition of spontaneous emission of a light emitting Indium-Gallium-Arsenide-Phosphide (InGaAsP) multiple quantum well in a GaAs woodpile structure [245]. The first experiment showing true control of spontaneous emission (by changing the lifetime of the excited state) made use of semiconductor quantum dots in inverse opal photonic crystals [246]. Subsequent experiments demonstrating the suppression of light emission caused by the defect of the photonic band gap are described in [247–250].

In this chapter, we present a simple procedure to determine the spontaneous emission rate from short-time FDTD simulation data of the electromagnetic energy field. We validate this procedure by computing the LRDOS of two-dimensional photonic crystals, employing the unconditionally stable FDTD method described in Chapter 2. Although this computation is more expensive than the procedure based on the electromagnetic field energy data, this FDTD based method does not require a solution of the eigenvalue problem nor integrations over the first Brillouin zone.

6.2 The emission rate

As discussed in Chapter 2, we can write the time-dependent Maxwell equations for the electromagnetic fields in linear, isotropic, nondispersive, lossless dielectric materials without electric charges and magnetic current sources as

$$\frac{\partial}{\partial t}\Psi(t) = \mathcal{H}\Psi(t) - \mathcal{S}(t), \tag{6.1}$$

where $\Psi(t) = (\sqrt{\mu(\mathbf{r})}\mathbf{H}(\mathbf{r},t), \sqrt{\varepsilon(\mathbf{r})}\mathbf{E}(\mathbf{r},t))^{\mathrm{T}}$, $\mathcal{H}$ denotes the operator

$$\begin{pmatrix} 0 & -\frac{1}{\sqrt{\mu(\mathbf{r})}}\nabla\times\frac{1}{\sqrt{\varepsilon(\mathbf{r})}} \\ \frac{1}{\sqrt{\varepsilon(\mathbf{r})}}\nabla\times\frac{1}{\sqrt{\mu(\mathbf{r})}} & 0 \end{pmatrix}, \tag{6.2}$$

and $\mathcal{S}(t) = (0, \mathbf{J}(\mathbf{r},t)/\sqrt{\varepsilon(\mathbf{r})})^{\mathrm{T}}$ denotes the source term.

From the definition of $\Psi(t)$ it follows that

$$\langle\Psi(t)|\Psi(t)\rangle = \int_V [\varepsilon(\mathbf{r})(\mathbf{E}^2(\mathbf{r},t) + \mu(\mathbf{r})\mathbf{H}^2(\mathbf{r},t)]\, d\mathbf{r}, \tag{6.3}$$

relating the length (norm) of vector $\Psi(t)$ to the energy density $w(\mathbf{r},t) = \varepsilon(\mathbf{r})\mathbf{E}^2(\mathbf{r},t) + \mu(\mathbf{r})\mathbf{H}^2(\mathbf{r},t)$ of the electromagnetic fields. Here V denotes the volume of the enclosing box. The energy emitted by the point source can thus be defined as $U(t) = \langle\Psi(t)|\Psi(t)\rangle$. The emission rate can be obtained by differentiation of $U(t)$: $P(t) = \partial U(t)/\partial t$.

As mentioned earlier, the emission properties can also be investigated by calculating the LRDOS. Here we demonstrate that there is a simple relation between the emitted energy and the LRDOS. The formal solution of Eq. (6.1) is given by

$$\Psi(t) = e^{tH}\Psi(0) - \int_0^t e^{(t-u)H} S(u)\, du. \tag{6.4}$$

We assume that the electric current density of a unit point source located at $\mathbf{r} = \mathbf{r_0}$ is given by

$$\mathbf{J}(\mathbf{r},t) = \mathbf{O}\theta(t)\delta(\mathbf{r}-\mathbf{r_0})\sin\Omega t, \tag{6.5}$$

where Ω is the angular frequency of the source and $\mathbf{O}$ defines the direction of the electric current. As indicated by the step function $\theta(t)$ in Eq. (6.5), the source is turned on at $t = 0$. Making use of Eq. (6.4) and Eq. (6.5) and assuming that $\Psi(\mathbf{r}, t = 0) = 0$, we find

$$\begin{aligned} U(t) =& \langle\Psi(t)|\Psi(t)\rangle = \frac{1}{\varepsilon(\mathbf{r}_0)}\int_0^t\int_0^t \langle\mathbf{S}_0|e^{(u'-u)H}\mathbf{S}_0\rangle \sin\Omega u \sin\Omega u'\, du\, du' \\ =& \frac{1}{2\pi}\int_{-\infty}^{+\infty}\int_0^t\int_0^t N_{rad}(\mathbf{S}_0,\mathbf{O},\omega)\cos\omega(u'-u)\sin\omega u\sin\omega u' du du' d\omega, \end{aligned} \tag{6.6}$$

where $\mathbf{S}_0 = (0, \hat{\mathbf{S}}_0)$ and $\langle\mathbf{r}|\hat{\mathbf{S}}_0\rangle = \mathbf{O}\,\delta(\mathbf{r}-\mathbf{r}_0)$. The LRDOS is defined by $N_{rad}(\mathbf{S}_0,\mathbf{O},\omega) = \varepsilon(\mathbf{r}_0)^{-1}N(\mathbf{S}_0,\mathbf{O},\omega)$ (see Eq. (2.51)), where

$$N(\mathbf{S}_0,\mathbf{O},\omega) \equiv \int_{-\infty}^{+\infty} e^{i\omega t}\langle\mathbf{S}_0|e^{tH}\mathbf{S}_0\rangle\, dt, \tag{6.7}$$

denotes the local density of states (LDOS) for frequency ω and direction $\mathbf{O}$ at the position

$\mathbf{r}_0$. We carry out the time integration to obtain

$$U(t) = \frac{1}{\pi}\int_{-\infty}^{+\infty} N_{rad}(\mathbf{S}_0, \mathbf{O}, \omega) \left[\frac{\sin^2 t(\omega-\Omega)/2}{(\omega-\Omega)^2} - \frac{\sin t(\omega-\Omega)/2}{\omega-\Omega}\frac{\sin t(\omega+\Omega)/2}{\omega+\Omega}\cos t\Omega\right] d\omega. \quad (6.8)$$

In the limit $t \to \infty$ the contribution of the second term in Eq. (6.8) vanishes, yielding for the emission rate

$$\begin{aligned}\lim_{t\to\infty} P(t) = \lim_{t\to\infty}\frac{\partial U(t)}{\partial t} &= \lim_{t\to\infty}\int_{-\infty}^{+\infty} N_{rad}(\mathbf{S}_0, \mathbf{O}, \omega)\frac{\sin t(\omega-\Omega)}{2\pi(\omega-\Omega)}\, d\omega, \\ &= N_{rad}(\mathbf{S}_0, \mathbf{O}, \Omega)/2, \end{aligned} \quad (6.9)$$

which, apart from some constants, agrees with Eq. (26) in [217] and with the expression obtained by using Fermi's Golden Rule [211].

For microcavities of arbitrary geometry, $U(t)$ is most easily calculated by solving the time-dependent Maxwell equations by means of an FDTD method [20]. We employ an algorithm that, in the absence of external currents, conserves the energy exactly (see Chapter 2). This property ensures that the time-dependence of $U(t)$ is due to the presence of the source only. In our numerical work, we use square simulation areas completely filled with the photonic crystal and having boundaries that are perfect reflecting conductors. We measure distances in units of the wavelength λ of light in air. Time and frequency are then expressed in units of λ/c and c/λ, respectively, where c denotes the velocity of light in air. For photonic crystals with lattice constant a, $f = \omega a/2\pi c$ is the dimensionless frequency.

6.3 Spontaneous emission in two-dimensional photonic crystals

We study the emission properties of a point source embedded in a two-dimensional photonic crystal. The photonic crystal consists of a triangular lattice of air holes drilled in a dielectric material with $\varepsilon = 12.96$ and $\mu = 1$. We study two cases, the holes having a diameter $d = 0.80a$ and $d = 0.96a$, respectively. For reference, we use the MIT Photonic-Bands package [190] to compute the photonic band structure diagram for the TM mode. The results are shown in Fig. 6.1. For $d = 0.80a$, no gap is observed for the TM mode, but a gap extending from $f = 0.24$ to $f = 0.40$ is observed for the TE mode. For $d = 0.96a$, the photonic crystal has a complete photonic band gap. For the TM mode the gap extends from $f = 0.43$ to $f = 0.52$ and for the TE mode from $f = 0.36$ to $f = 0.53$.

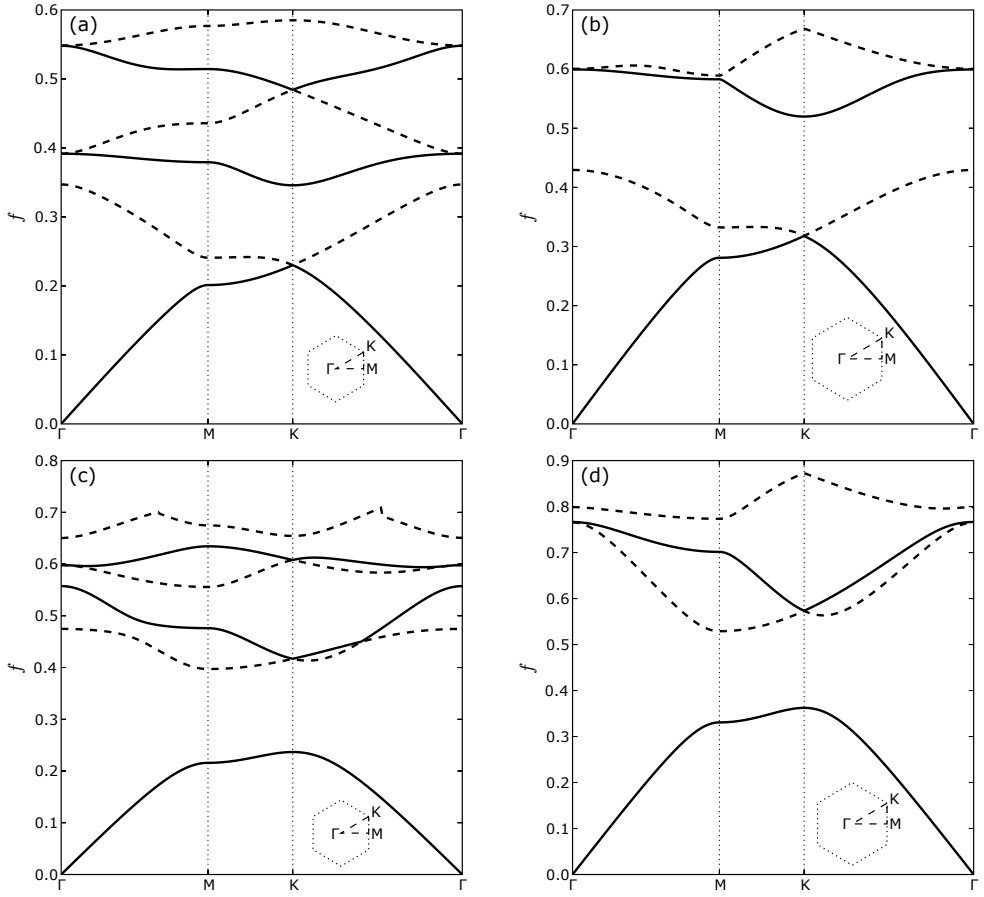

Figure 6.1: Photonic band structure diagram of TM (top) and TE (bottom) modes for a triangular lattice of air holes drilled in a dielectric medium ($\varepsilon = 12.96$, $\mu = 1$, $\sigma = 0$). The holes have a diameter d. (a): TM mode, $d = 0.80a$. (b): TM mode, $d = 0.96a$. (c): TE mode, $d = 0.80a$. (d): TE mode, $d = 0.96a$. $f = \omega a/2\pi c$ is the dimensionless frequency. The first Brillouin zone of a triangular lattice and the symmetry points are shown in the inset (see Appendix A).

6.3.1 TM mode[1]

To compute the emitted energy we put a point source with a current density specified by Eq. (6.5) at different locations $\mathbf{r}_0$ near the center of the simulation area. The locations are chosen such that the source is located at one of the E_z-points of the two-dimensional Yee grid (see Fig. 2.2, TM mode). The emitted energy $U(t)$ is trivially obtained from the solution for the electromagnetic fields, see Eq. (6.3). In order to have a reference value for the emitted energy, we first compute $U(t)$ for a point source located in the middle of a square

[1] Results of this section were published in Physical Review Letters **96**, 120401 (2006).

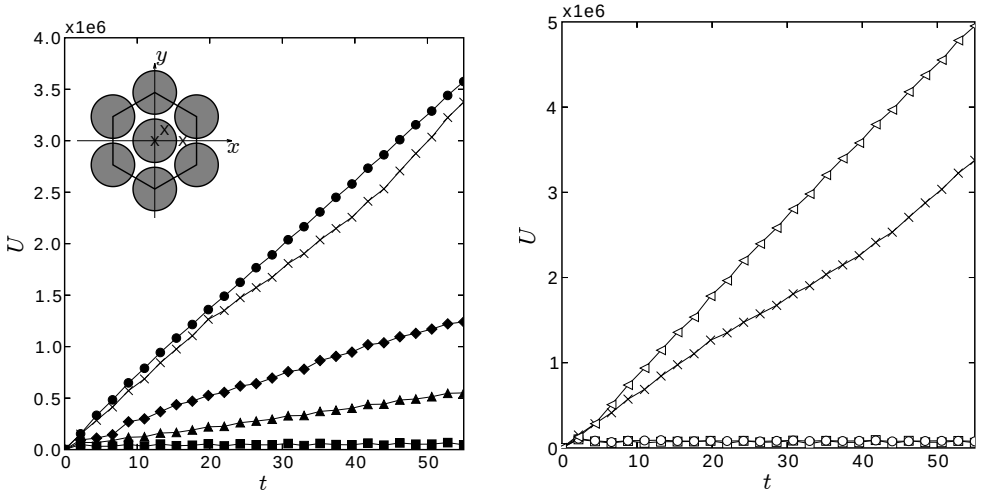

Figure 6.2: Emitted energy U (TM mode) as a function of time t for a point source embedded in air (crosses) and for a point source located at position $\mathbf{r}_0$ in a two-dimensional photonic crystal. The photonic crystal consists of a triangular lattice of air holes with diameter d drilled in a dielectric material ($\varepsilon = 12.96$, $\mu = 1$). The inset shows the triangular lattice network with spacing a in real space. The crosses indicate the source positions $\mathbf{r}_0$. Solid symbols: $d = 0.80a$, open symbols: $d = 0.96a$. Solid squares: $\mathbf{r}_0 = (0, 0)$, $f = 0.30$; solid triangles: $\mathbf{r}_0 = a(0.20, 0.23)$, $f = 0.30$; solid circles: $\mathbf{r}_0 = a(\sqrt{3}/3, 0)$, $f = 0.30$; solid diamonds: $\mathbf{r}_0 = (0, 0)$, $f = 0.53$; open squares: $\mathbf{r}_0 = (0, 0)$, $f = 0.48$; open circles: $\mathbf{r}_0 = a(\sqrt{3}/3, 0)$, $f = 0.48$; open triangles: $\mathbf{r}_0 = (0, 0)$, $f = 0.56$.

area completely filled with air. In what follows, we refer to this setup as the empty area. The result is shown in Fig. 6.2 (crosses). The slope of the line that can be drawn through the data for $t \leq 20$ gives a measure for the emission rate (up to a scaling factor). For larger times the data deviates from a straight line. This is due to reflections at the boundaries of the simulation area. The solid symbols in Fig. 6.2 denote the results for a point source embedded in the triangular-lattice photonic crystal with $d = 0.80a$. We show three results for a source emitting light with a frequency $f = 0.30$. If the source is located in the center of a hole (solid squares) the emitted energy is very small and almost constant as a function of time. Hence, light emission is strongly suppressed and for all practical purposes inhibited. If we move the source away from the center of the hole, but so that it is still located in the air region (solid triangles), light emission is enhanced compared to the case for which the source was placed in the centre of the hole (solid squares), but strongly suppressed compared to the empty area case (crosses). Placing the source in a region with $\varepsilon = 12.96$ leads to an emission enhancement (solid circles) compared to the empty area case. Changing the frequency of the emitted light to $f = 0.53$ and putting the source in the center of a hole also leads to a suppression of the light emission (solid diamonds), but not to an inhibition of the emission, as in the case of $f = 0.3$. From these results, it can be concluded that the emission rate strongly depends on the location of the source and on the frequency of the emitted light: Emission enhancement as well as emission suppression can be observed. Even if the photonic crystal has no photonic

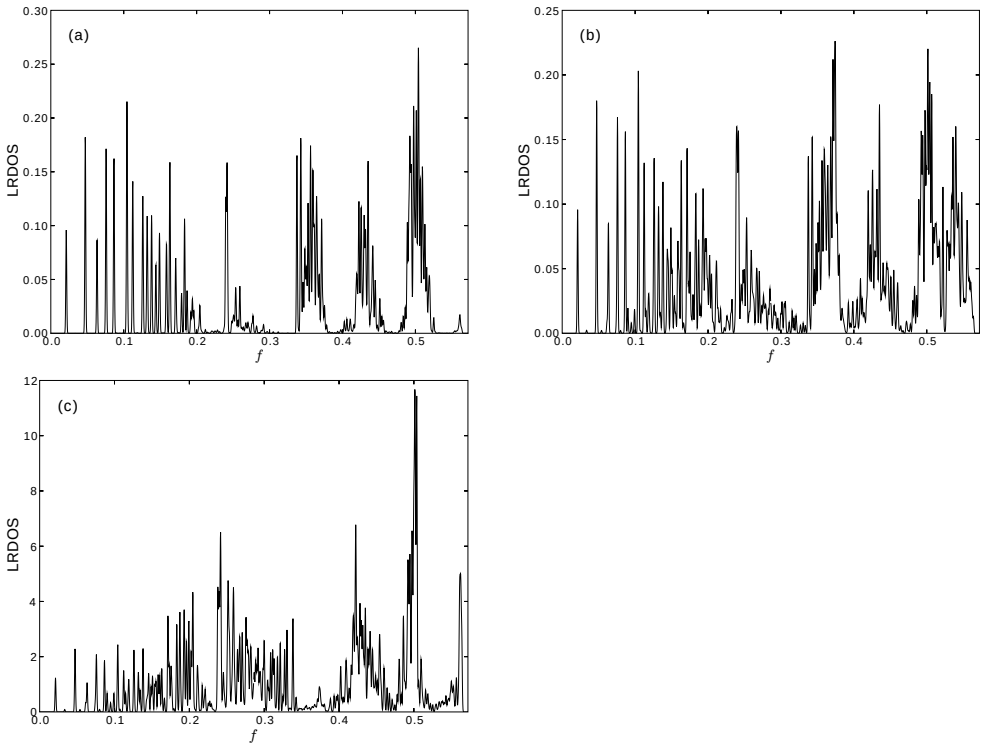

Figure 6.3: LRDOS (TM mode) for various source locations $\mathbf{r}_0$ in the triangular-lattice photonic crystal with $d = 0.80a$. (a): $\mathbf{r}_0 = (0, 0)$; (b): $\mathbf{r}_0 = a(0.20, 0.23)$; (c): $\mathbf{r}_0 = a(\sqrt{3}/3, 0)$. $f = \omega a/2\pi c$ is the dimensionless frequency.

band gap, the emission of a point source can be almost completely suppressed [52].

Fig. 6.2 also shows the results of the energy emitted by a point source embedded in the triangular-lattice photonic crystal with $d = 0.96a$, a photonic crystal having a photonic band gap. For $f = 0.48$, a frequency inside the photonic band gap, and sources located in the center of a hole (open squares) or in the dielectric material (open circles), light emission is inhibited for all practical purposes. Note that the values for $U(t)$ for these two cases are comparable to the value of $U(t)$ for the case of a source emitting light with a frequency $f = 0.3$ and located in the center of a hole in the photonic crystal with $d = 0.80a$. Increasing the frequency of the light emitted by a source, located at the center of a hole, to $f = 0.56$ (open triangles) leads to a strong emission enhancement compared to the empty area case.

We validate the conclusions based on the behavior of the results for $U(t)$ by computing the LRDOS. We use the following procedure: We first set the electromagnetic fields at the point $\mathbf{r}_0$ on the two-dimensional Yee grid so that $E_z(\mathbf{r}_0, t) = 1$ and so that all other (components of the) electromagnetic fields are zero at all other points of the grid. We then solve the

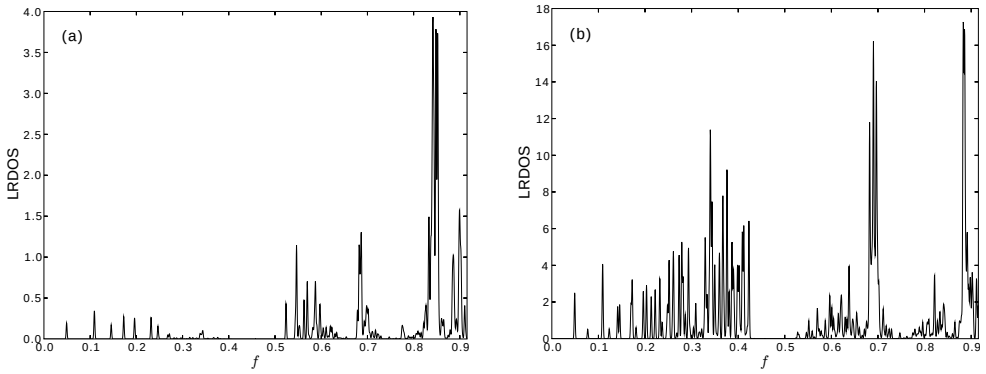

Figure 6.4: LRDOS (TM mode) for various source locations $\mathbf{r}_0$ in the triangular-lattice photonic crystal with $d = 0.96a$. (a): $\mathbf{r}_0 = (0, 0)$; (b): $\mathbf{r}_0 = a(\sqrt{3}/3, 0)$. $f = \omega a/2\pi c$ is the dimensionless frequency.

time-dependent Maxwell equations and store the values of $f(t) = \varepsilon(\mathbf{r}_0)^{-1} \left\langle \mathbf{S}_0 | e^{tH} \mathbf{S}_0 \right\rangle$. The (fast) Fourier transform of $f(t)$ then yields the LRDOS. By using an unconditionally stable algorithm (see Chapter 2) we do not have to solve the eigenvalue problem for H [51]. This is an important advantage over methods that compute the L(R)DOS by integrating the modulus of the electric field in the first Brillouin zone. Not only does the diagonalization require a lot of computer time, also all points of the entire first Brillouin zone should be included in the calculation of the L(R)DOS [251]. As pointed out in [251], this integral was often performed incorrectly within an irreducible first Brillouin zone[252–255] by using a linear tetrahedron method.

Figures 6.3 and 6.4 show the results for the LRDOS for the same source positions as the ones used to obtain the results depicted in Fig. 6.2. The height of the peaks in the LRDOS have a physical meaning: from Eq. (2.52) it follows that the height of the peak in the LRDOS at frequency ω is proportional to the electromagnetic field intensity of the corresponding eigenmode. For practical purposes, we consider the LRDOS to exhibit a gap if for a certain frequency range the electromagnetic field intensity is below the threshold of numerical noise, which in our numerical simulations is approximately 10^{-10}. Figure 6.3 shows the LRDOS for sources embedded in a triangular-lattice photonic crystal with $d = 0.80a$. If the source is located in the center of a hole (see Fig. 6.3a), then the LRDOS shows a small gap around $f = 0.30$. In this frequency range there are no electromagnetic modes. Hence, light with a frequency $f = 0.30$ emitted by a source positioned in the center of a hole cannot propagate into the photonic crystal. Note however, that the photonic crystal has no photonic band gap and hence the DOS has no gaps around $f = 0.30$. Increasing the frequency of the source to for example $f = 0.53$ allows the light to propagate through the system. Moving the source away from the center of a hole, but in a way that it is still located in the air region, results in an increase of the density of states around $f = 0.30$ (see Fig. 6.3b). Although the LRDOS is

still rather low at $f = 0.30$, light can now propagate into the photonic crystal. From Fig. 6.3c it can be seen that placing the source in a region with $\varepsilon = 12.96$ leads to a further increase of the LRDOS around $f = 0.3$. Comparing the results of Fig. 6.2 with the results of Fig. 6.3 indicates that the number of modes at a given frequency gives a rough quantitative measure of the emission rate. Fig. 6.4 depicts the LRDOS for the case $d = 0.96a$. For frequencies inside the photonic band gap, no modes are available, independent of the position of the source. Hence, for $f = 0.48$ emission is inhibited, as was also concluded from Fig. 6.2. For $f = 0.56$, a frequency in a pass band, no gaps in the LRDOS are seen for source positions in a hole. Note that in the low frequency domain the LRDOS depicted in Figs. 6.3 and 6.4 shows several small gaps. These gaps probably correspond to finite-size gaps. However, at these low frequencies it is very difficult to make a distinction between a finite-size gap and a real gap. This is a drawback of methods that use the LRDOS to study the emission rate.

6.3.2 TE mode

We now repeat the calculations for the TE mode instead of the TM mode. For this purpose, we replace the source term in Eq. (6.1) by

$$\mathcal{S}(t) = (0, \mathbf{M}(\mathbf{r}, t)/\sqrt{\mu(t)})^{\mathrm{T}}, \tag{6.10}$$

where $\mathbf{M}(\mathbf{r}, t)$ denotes the magnetic current source and we replace the operator $\mathcal{H}$ by

$$\begin{pmatrix} 0 & -\frac{1}{\sqrt{\mu(\mathbf{r})}}\nabla \times \frac{1}{\sqrt{\varepsilon(\mathbf{r})}} \\ \frac{1}{\sqrt{\varepsilon(\mathbf{r})}}\nabla \times \frac{1}{\sqrt{\mu(\mathbf{r})}} & 0 \end{pmatrix}, \tag{6.11}$$

We assume that the magnetic current density of a unit point source located at $\mathbf{r} = \mathbf{r}_0$ has a similar form as the electric current density given in Eq. (6.5). Hence, we take

$$\mathbf{M}(\mathbf{r}, t) = \mathbf{O}\, \theta(t)\delta(\mathbf{r} - \mathbf{r_0}) \sin \Omega t. \tag{6.12}$$

The expression for the energy emitted by the magnetic source is still given by Eqs. (6.3) and (6.8), but the LRDOS is now defined as

$$N_{rad}(\mathbf{S}_0, \mathbf{O}, \omega) = \mu(\mathbf{r}_0)^{-1} N(\mathbf{S}_0, \mathbf{O}, \omega). \tag{6.13}$$

Note that for the photonic crystal $\mu(\mathbf{r}) = 1$, so that for the TE mode the LRDOS equals the LDOS. To compute the emitted energy, we put a point source with a current density specified by Eq. (6.12) at different locations $\mathbf{r}_0$ near the center of the simulation area. The locations are chosen such that the magnetic current source is located at one of the $\mathbf{H}_z$-points of the two-dimensional Yee grid (see Fig. 2.2, TE-mode). The emitted energy is again obtained from the

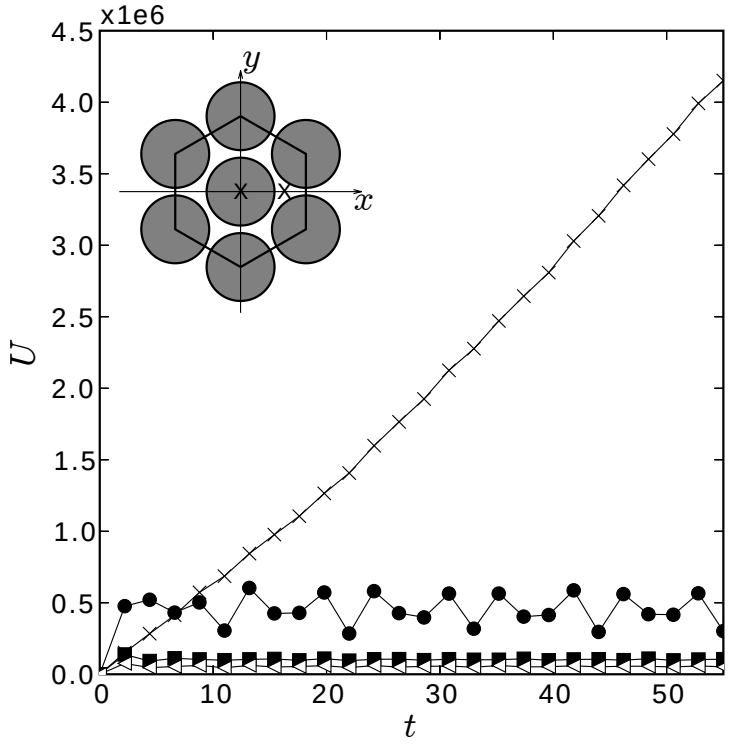

Figure 6.5: Emitted energy U (TE mode) as a function of time t for a point source embedded in air (crosses) and for a point source located at position $\mathbf{r}_0$ in a two-dimensional photonic crystal. The photonic crystal consists of a triangular lattice of air holes with diameter d drilled in a dielectric material ($\varepsilon = 12.96$, $\mu = 1$). The inset shows the triangular lattice network with spacing a in real space. The crosses indicate the source positions $\mathbf{r}_0$. Solid squares: $\mathbf{r}_0 = (0, 0)$, $f = 0.30$, $d = 0.80a$; Solid circles: $\mathbf{r}_0 = a(\sqrt{3}/3, 0)$, $f = 0.30$, $d = 0.80a$; Open triangles: $\mathbf{r}_0 = (0, 0)$, $f = 0.48$, $d = 0.96a$.

solution for the electromagnetic fields (see Eq. (6.3)). We first compute $U(t)$ for the empty area, which again serves as a reference value for the emitted energy in a photonic crystal. The result is shown in Fig. 6.5 (crosses). The solid (open) symbols in Fig. 6.5 denote the results for a point source embedded in the triangular-lattice photonic crystal with $d = 0.80a$ ($d = 0.96a$). For the TE mode, we only consider sources emitting frequencies in the photonic band gap. Hence, we expect that the emission of the point source is completely suppressed. For photonic crystals with $d = 0.80a$ we show two results for a source emitting light with a frequency $f = 0.3$. If the source is located in the center of a hole (solid squares) the emitted energy is very small and almost constant as a function of time. Hence, light emission is for all practical purpose inhibited. If we place the source in a region with $\varepsilon = 12.96$ (solid circles), the emitted energy is slightly enhanced and oscillates more compared to the case for which the source was placed in the center of a hole (solid squares), but on average the emission rate

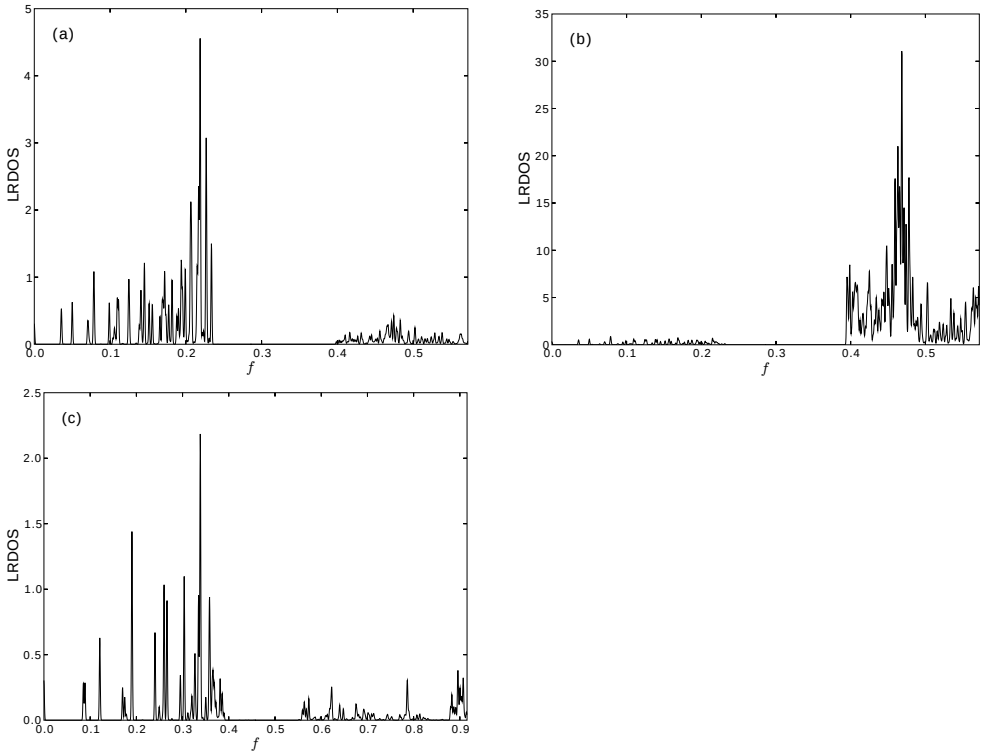

Figure 6.6: LRDOS (TE mode) for various source locations $\mathbf{r}_0$ in the triangular-lattice photonic crystal. (a): $\mathbf{r}_0 = (0,0), d = 0.80a$; (b): $\mathbf{r}_0 = a(\sqrt{3}/3, 0), d = 0.80a$. (c): $\mathbf{r}_0 = (0,0), d = 0.96a$. $f = \omega a/2\pi c$ is the dimensionless frequency.

is zero. Changing the frequency of the emitted light to $f = 0.48$ and putting the source in the center of a hole (open triangles) also leads to an inhibition of the emission, as in the case of $f = 0.3$. From these results, it can be concluded that the emission rate is zero for frequencies in the photonic band gap.

We validate the conclusions based on the behavior of the results for $U(t)$ by computing the LRDOS. In the case of the TE mode we use the following procedure: We first set the electromagnetic fields at the point $\mathbf{r}_0$ on the two-dimensional Yee grid so that $\mathbf{H}_z(\mathbf{r}_0, t = 0) = 1$ and so that all other (components of the) electromagnetic fields are zero at all other points of the grid. We then solve the time-dependent Maxwell equations and store the values of $f(t) = \mu(\mathbf{r}_0)^{-1}\langle \mathbf{S}_0 | e^{tH} \mathbf{S}_0 \rangle = \langle \mathbf{S}_0 | e^{tH} \mathbf{S}_0 \rangle$. The (fast) Fourier transform of $f(t)$ then yields the LRDOS, which in this case is equal to the LDOS.

Figure 6.6 shows the results for the LRDOS for the same source positions as the ones used to obtain the results depicted in Fig. 6.5. Figures 6.6a and 6.6b show the LRDOS for sources embedded in a triangular-lattice photonic crystal with $d = 0.80a$. If the source is located

in the center of a hole or in a region with $\varepsilon = 12.96$, then the LRDOS shows a gap around $f = 0.3$. The gap corresponds to the photonic band gap. In this frequency range there are no electromagnetic modes. Hence, light with a frequency $f = 0.3$ emitted by a point source positioned in the center of a hole or in a region with $\varepsilon = 12.96$ cannot propagate into the photonic crystal, as was also concluded from Fig. 6.5. Figure 6.6c depicts the LRDOS for the case $d = 0.96a$. Also for this case, the photonic crystal has a photonic band gap for the TE mode. For frequencies inside the photonic band gap, no modes are available, independent of the position of the source. Hence, for $f = 0.48$ emission is inhibited, as was concluded from Fig. 6.5.

6.4 Conclusions

In this chapter we have presented a simple and efficient procedure to extract the spontaneous emission rate from short-time FDTD simulation data of the electromagnetic field energy in microcavities of arbitrary geometry. We demonstrated its validity by comparison with L(R)DOS calculations for two-dimensional triangular-lattice photonic crystals.

By using an unconditionally stable algorithm to compute the L(R)DOS we do not have to solve an eigenvalue problem. This is an important advantage over methods that compute the L(R)DOS by integrating the modulus of the electric field in the first Brillouin zone. However, computing the LRDOS gives only qualitative information about the emission rate, while computing the emitted energy gives quantitative information about the emission rate. By using the unconditionally stable method to compute the emitted energy, we are guaranteed that, in the absence of external currents, the algorithm conserves the energy exactly. This ensures that the time-dependence of the emitted energy is due to the presence of the source only. Hence, extracting the spontaneous emission rate from short-time FDTD simulation data of the electromagnetic field energy, obtained by an unconditionally stable method to solve the time-dependent Maxwell equations, is the most simple and efficient method to study spontaneous emission in arbitrary microcavities.

Appendix A

The Brillouin zone

In this appendix we explain the concept of first (irreducible) and higher Brillouin zones for the two-dimensional square and triangular lattice closely following [191]. A fundamental concept in the description of a crystalline solid, or in general a periodic structure, is the Bravais lattice, which specifies the periodic array in which the repeated units of the structure (such as the crystal) are arranged [191]. A Bravais lattice consists of all points with position vectors $\mathbf{R}$ of the form

$$\mathbf{R} = \sum_i n_i \mathbf{a}_i, \tag{A.1}$$

where $\mathbf{a}_i$ are linear independent vectors, and n_i range through all integers. The vectors $\mathbf{a}_i$ are called primitive vectors and are said to generate or span the lattice. A Bravais lattice is thus an infinite array of discrete points with an arrangement and orientation that appears exactly the same, from whichever of the points the array is viewed [191].

Consider a set of points $\mathbf{R}$ constituting a Bravais lattice, and a plane wave $e^{i\mathbf{k}\cdot\mathbf{r}}$. Wave vectors $\mathbf{K}$, which satisfy the relation

$$e^{i\mathbf{K}\cdot(\mathbf{r}+\mathbf{R})} = e^{i\mathbf{K}\cdot\mathbf{r}}, \tag{A.2}$$

for any $\mathbf{r}$ and for all $\mathbf{R}$, belong to the reciprocal lattice of a Bravais lattice of points $\mathbf{R}$. Factoring out $e^{i\mathbf{K}\cdot\mathbf{r}}$, the reciprocal lattice can be characterized as the set of wave vectors $\mathbf{K}$ satisfying

$$e^{i\mathbf{K}\cdot\mathbf{R}} = 1, \quad \text{i.e.} \quad \mathbf{K}\cdot\mathbf{R} = N\cdot 2\pi, \tag{A.3}$$

where N is an integer. A reciprocal lattice is defined with reference to a particular Bravais lattice, which is called the direct lattice. The reciprocal lattice is itself a Bravais lattice. The reciprocal lattice of a reciprocal lattice is just the original direct lattice. In three-dimensional space, if $\mathbf{a}_i, i = 1, 2, 3$ are a set of primitive vectors of the direct lattice, the reciprocal lattice

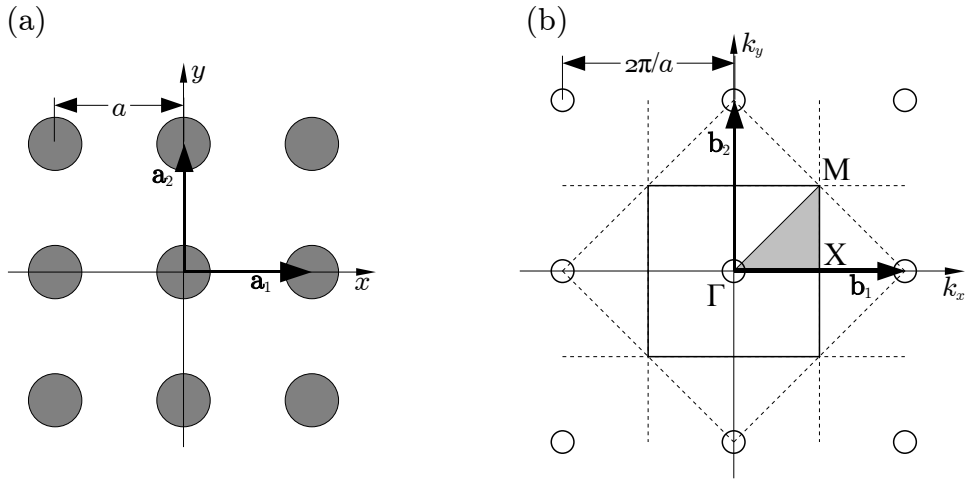

Figure A.1: The two-dimensional square lattice. (a): Square lattice network with spacing a in real space. The lattice vectors are denoted by $\mathbf{a}_1$ and $\mathbf{a}_2$. (b): Corresponding reciprocal lattice, a square lattice with spacing $2\pi/a$. The reciprocal lattice vectors are denoted by $\mathbf{b}_1$ and $\mathbf{b}_2$. The dotted lines are the perpendicular bisectors to the reciprocal lattice vectors connecting the origin (Γ point) to its nearest neighbor reciprocal lattice points. The region enclosed by these lines and containing the origin is the first Brillouin zone (solid square). The shaded area is the irreducible first Brillouin zone. The symmetry points Γ, M and X are also shown.

can be generated by the primitive vectors $\mathbf{b}_i, i = 1, 2, 3$

$$\begin{aligned}
\mathbf{b}_1 &= 2\pi \frac{\mathbf{a}_2 \times \mathbf{a}_3}{\mathbf{a}_1 \cdot (\mathbf{a}_2 \times \mathbf{a}_3)}, \\
\mathbf{b}_2 &= 2\pi \frac{\mathbf{a}_3 \times \mathbf{a}_1}{\mathbf{a}_1 \cdot (\mathbf{a}_2 \times \mathbf{a}_3)}, \\
\mathbf{b}_3 &= 2\pi \frac{\mathbf{a}_1 \times \mathbf{a}_2}{\mathbf{a}_1 \cdot (\mathbf{a}_2 \times \mathbf{a}_3)}.
\end{aligned} \tag{A.4}$$

In reciprocal space we can construct a region that surrounds the origin such that all $\mathbf{k}$-points enclosed are closer to the origin than to any other reciprocal lattice point. This set of points in $\mathbf{k}$-space is called the first Brillouin zone. As is geometrically evident, the first Brillouin zone is the region enclosed by the sets of planes that are perpendicular bisectors to the lattice vectors connecting the origin in $\mathbf{k}$-space to its nearest neighbor reciprocal lattice points. In general, planes that are perpendicular bisectors of a line joining the origin of k-space of a reciprocal lattice points are called Bragg planes. Hence, the first Brillouin zone can also be defined as the set of points in k-space that can be reached from the origin without crossing any Bragg plane. Due to symmetry reasons, most of the time we only need to analyze a part of the first Brillouin zone. This part is called the irreducible first Brillouin zone. Higher Brillouin zones are simply other regions bounded by the Bragg planes. The second Brillouin zone is

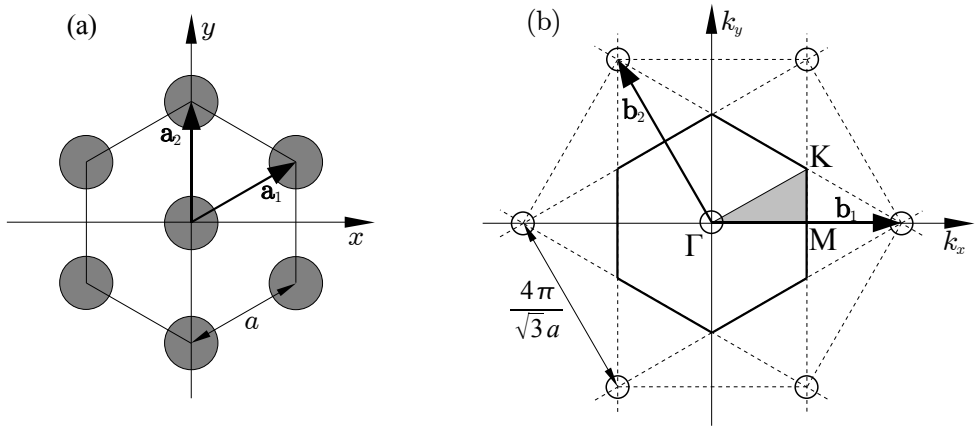

Figure A.2: The two-dimensional triangular lattice. (a) Triangular lattice network with spacing a in real space. The lattice vectors are denoted by $\mathbf{a}_1$ and $\mathbf{a}_2$. (b) Corresponding reciprocal lattice, a triangular lattice with spacing $4\pi/\sqrt{3}a$. The reciprocal lattice vectors are $\mathbf{b}_1$ and $\mathbf{b}_2$. The dotted lines are the perpendicular bisectors to the reciprocal lattice vectors connecting the origin (Γ point) to its nearest neighbor reciprocal lattice points. The region enclosed by these lines and containing the origin is the first Brillouin zone (solid hexagon). The shaded area is the irreducible first Brillouin zone. The symmetry points Γ, M and K are also shown.

defined as the set of points that can be reached from the first Brillouin zone by crossing only one Bragg plane. Similarly, the nth Brillouin zone is the set of points that can be reached from the $(n-1)$th zone by crossing one and only one Bragg plane. Alternatively, the nth Brillouin zone can be defined as the set of points that can be reached from the origin by crossing $n-1$ Bragg planes, but no fewer.

We now consider the two mostly used two-dimensional lattices, namely the square and the triangular lattice (often mistakenly called hexagonal lattice). For a square lattice with spacing a, the simplest lattice vectors are

$$\mathbf{a}_1 = a\hat{\mathbf{x}} \quad \text{and} \quad \mathbf{a}_2 = a\hat{\mathbf{y}}, \tag{A.5}$$

where $\hat{\mathbf{x}}$ and $\hat{\mathbf{y}}$ denote unit vectors along the x and y axis, respectively. In order to use (A.4), we can use a third basis vector in the z-direction of any length. The results are

$$\mathbf{b}_1 = (2\pi/a)\hat{\mathbf{x}} \quad \text{and} \quad \mathbf{b}_2 = (2\pi/a)\hat{\mathbf{y}}. \tag{A.6}$$

It is easily seen that the reciprocal lattice of the square lattice is also a square lattice, but with spacing $2\pi/a$ instead of a. The original lattice, the reciprocal lattice, the first Brillouin zone and the irreducible first Brillouin zone of the square lattice are depicted in Fig. A.1. The high symmetry $\mathbf{k}$-points, which are the three corners of the irreducible first Brillouin zone, are

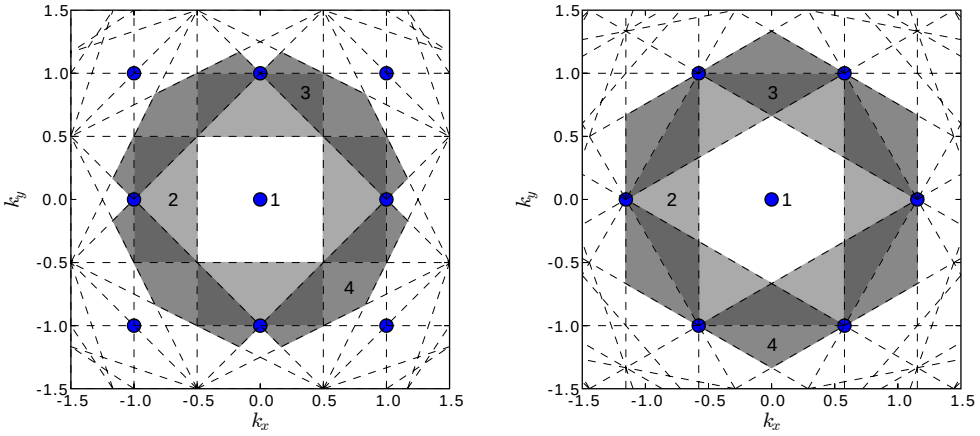

(a) Square lattice

(b) Triangular lattice

Figure A.3: The Brillouin zones for (a): the square lattice and (b): the triangular lattice. The solid circles are the lattice points and the dashed lines are the Bragg lines. The first four Brillouin zones are marked with different gray scales.

given by

$$\Gamma: \quad k_x = 0, \quad k_y = 0, \tag{A.7a}$$

$$\mathrm{M}: \quad k_x = \pi/a, \quad k_y = \pi/a, \tag{A.7b}$$

$$\mathrm{X}: \quad k_x = \pi/a, \quad k_y = 0. \tag{A.7c}$$

For a triangular lattice with spacing a, the lattice vectors can be chosen as

$$\mathbf{a}_1 = a(\sqrt{3}\hat{\mathbf{x}} + \hat{\mathbf{y}})/2 \quad \text{and} \quad \mathbf{a}_2 = a\hat{\mathbf{y}}, \tag{A.8}$$

as shown in Fig. Fig. A.2. Using (A.4), we obtain the reciprocal lattice vectors

$$\mathbf{b}_1 = \frac{4\pi}{\sqrt{3}a}\hat{\mathbf{x}} \quad \text{and} \quad \mathbf{b}_2 = \frac{4\pi}{\sqrt{3}a}(-\frac{\sqrt{3}}{2}\hat{\mathbf{x}} + \frac{1}{2}\hat{\mathbf{y}}). \tag{A.9}$$

The reciprocal lattice is again a triangular lattice. Fig. A.2 shows the original lattice, the reciprocal lattice, the first Brillouin zone and the irreducible first Brillouin zone. The three corners of the irreducible first Brillouin zone, the high symmetry $\mathbf{k}$-points, are defined as

follows

$$\Gamma: \quad k_x = 0, \quad k_y = 0, \tag{A.10a}$$

$$\mathrm{M}: \quad k_x = \tfrac{2\pi}{\sqrt{3}a}, \quad k_y = 0, \tag{A.10b}$$

$$\mathrm{K}: \quad k_x = \tfrac{2\pi}{\sqrt{3}a}, \quad k_y = \frac{2\pi}{3a}. \tag{A.10c}$$

In Fig. A.3 we show the Bragg planes (dashed lines) and the first four Brillouin zones for the two-dimensional square lattice and triangular lattice space.

References

[1] J. C. Maxwell. *A Dynamical Theory of the Electromagnetic Field*. Philosophical Transactions of the Royal Society of London **155**, 459 (1865).

[2] J. D. Joannopoulos, R. D. Meade, and J. N. Winn. *Photonic Crystals: Molding the flow of light* (Princeton Univ. Press, Princeton, New Jersey, 1995).

[3] M. Notomi. *Theory of light propagation in strongly modulated photonic crystals: Refractionlike behavior in the vicinity of the photonic band gap*. Phys. Rev. B **62**, 10696 (2000).

[4] E. Yablonovitch. *Inhibited Spontaneous Emission in Solid-State Physics and Electronics*. Phys. Rev. Lett. **58**, 2059 (1987).

[5] H. Kosaka, T. Kawashima, A. Tomita, M. Notomi, T. Tamamura, T. Sato, and S. Kawakami. *Superprism phenomena in photonic crystals*. Phys. Rev. B **58**, 10096 (1998).

[6] S. Enoch, G. Tayeb, and D. Maystre. *Numerical evidence of ultrarefractive optics in photonic crystals*. Opt. Commun. **161**, 171 (1999).

[7] J. S. Foresi, P. R. Villeneuve, J. Ferrera, E. R. Thoen, G. Steinmeyer, S. Fan, J. D. Joannopoulos, L. C. Kimerling, H. I. Smith, and E. P. Ippen. *Photonic-bandgap microcavities in optical waveguides*. Nature **390**, 143 (1997).

[8] B. Goss Levi. *Progress made in near-field imaging with light from a sharp tip*. Phys. Today **52**, 18 (1999).

[9] E. Yablonovitch. *Photonic crystals: semiconductors of light*. Sci. Am. **285**, 46 (2001).

[10] S. John, O. Toader, and K. Busch. *Photonic Band Gap Materials: A Semiconductor for Light, Encyclopedia of Physical Science and Technology Vol. 12* (Academic, Orlando, 2001).

[11] J. C. Knight and P. S. J. Russell. *New Ways to Guide Light*. Science **296**, 276 (2002).

[12] C. López. *Materials aspects of photonic crystals*. Adv. Mater. **15**, 1679 (2003).

[13] E. Flück, N. F. van Hulst, W. L. Vos, and L. Kuipers. *Near-field optical investigation of three-dimensional photonic crystals*. Phys. Rev. E **68**, 015601 (2003).

[14] E. Flück. *Local interaction of light with periodic photonic structures*. Ph.D. thesis, University of Twente (2003). Chapter 5.

[15] T. Fujimura, T. Itoh, A. Imada, R. Shimada, T. Koda, N. Chiba, H. Muramatsu, H. Miyazaki, and K. Ohtaka. *Near-field optical images of ordered polystyrene particle layers and their photonic band effect*. J. Luminescence **87-89**, 954 (2000).

[16] M. Born and E. Wolf. *Principles of Optics*. 7th edition (Pergamon, Oxford, 2002).

[17] M. Notomi. *Negative refraction in photonic crystals*. Opt. Quantum Elec. **34**, 133 (2002).

[18] S. Foteinopoulou and C. M. Soukoulis. *EM wave propagation in two-dimensional photonic crystals: a study of anomalous refractive effects* (2004). Cond-mat/0403542.

[19] K. S. Yee. *Numerical Solution of Initial Boundary Value Problems involving Maxwell's Equations*. IEEE Trans. Antennnas Prop. **14**, 302 (1966).

[20] A. Taflove and S. C. Hagness. *Computational Electrodynamics - The Finite-Difference Time-Domain Method*. 3rd edition (Artech House, Boston, 2005).

[21] K. S. Kunz and R. J. Luebbers. *Finite-Difference Time-Domain Method for Electromagnetics* (CRC Press, 1993).

[22] J. S. Kole. *New methods for the numerical solutions of Maxwell's Equations*. Ph.D. thesis, MSC, Univ. Groningen (2003).

[23] O. P. Gandi. In A. Taflove (editor) *Advances in Computational Eletrodynamics - The Finite-Difference Time-Domain Method* (Artech House, Boston, 1998).

[24] B. Houshmand, T. Itoh, and M. Piket-May. In A. Taflove (editor) *Advances in Computational Electrodynamics: The Finite-Difference Time-Domain Method* (Artech House, Boston, 1998).

[25] J. S. Kole, M. T. Figge, and H. De Raedt. *Unconditionally stable algorithms to solve the time-dependent Maxwell equations*. Phys. Rev. E **64**, 066705 (2001).

[26] J. S. Kole, M. T. Figge, and H. De Raedt. *Higher-order unconditionally stable algorithms to solve the time-dependent Maxwell equations*. Phys. Rev. E **65**, 066705 (2002).

[27] H. De Raedt, J. S. Kole, K. F. L. Michielsen, and M. T. Figge. *Unified framework for numerical methods to solve the time-dependent Maxwell equations*. Comp. Phys. Comm. **156**, 43 (2003).

[28] H. De Raedt. *Chapter 18: Advances in Unconditionally Stable Techniques*. In A. Taflove and S. C. Hagness (editors) *Computational Electrodynamics - The Finite-Difference Time-Domain Method* (Artech House, MA USA, 2005).

[29] M. Suzuki, S. Miyashita, and A. Kuroda. *Monte Carlo simulation of quantum spin systems. I*. Prog. Theor. Phys. **58**, 1377 (1977).

[30] H. De Raedt. *Product formula algorithms for solving the time-dependent Schrödinger equation*. Comp. Phys. Rep. **7**, 1 (1987).

[31] H. F. Trotter. *On the product of semi-group operators*. Am. Math. Soc. **10**, 545 (1959).

[32] M. Suzuki. *Decomposition formulas of exponential operators and Lie exponentials with some applications to quantum mechanics and statistical physics*. J. Math. Phys. **26**, 601 (1985).

[33] M. Suzuki. *General theory of fractal path integrals with applications to many-body theories and statistical physics*. J. Math. Phys. **32**, 400 (1991).

[34] H. De Raedt and B. De Raedt. *Applications of the generalized Trotter formula*. Phys. Rev. A **28**, 3575 (1983).

[35] M. Abramowitz and I. Stegun. *Handbook of Mathematical Functions* (Dover, New York, 1964).

[36] G. D. Mahan. *Many-Particle Physics* (Plenum Press, New York, 1981).

[37] J. H. Wilkinson. *The Algebraic Eigenvalue Problem* (Clarendon Press, Oxford, 1965).

[38] G. H. Golub and C. F. V. Loan. *Matrix computations* (John Hopkins University Press, Baltimore, 1983).

[39] R. Alben, M. Blume, H. Krakauer, and L. Schwartz. *Exact results for a three-dimensional alloy with site diagonal disorder: comparison with the coherent potential approximation*. Phys. Rev. B **12**, 4090 (1975).

[40] M. D. Feit, J. A. Fleck, and A. Steiger. *Solution of the Schroedinger equation by a spectral*

method. J. Comput. Phys **47**, 412 (1982).

[41] H. De Raedt and P. De Vries. *Simulation of two and three-dimensional disordered systems: Lifshitz tails and localization properties*. Z. Phys. B **77**, 243 (1989).

[42] T. Kawarabayashi and T. Ohtsuki. *Diffusion of electrons in two-dimensional disordered symplectic systems*. Phys. Rev. B **53**, 6975 (1996).

[43] T. Ohtsuki and T. Kawarabayashi. *Anomalous Diffusion at the Anderson Transitions*. J. Phys. Soc. Jpn. **66**, 314 (1997).

[44] T. Iitaka, S. Nomura, H. Hirayama, X.Zhao, Y. Aoyagi, and T. Sugano. *Calculating the linear response functions of noninteracting electrons with a time-dependent Schrödinger equation*. Phys. Rev. E **56**, 1222 (1997).

[45] S. Nomura, T. Iitaka, X. Zhao, T. Sugano, and Y. Aoyagi. *Linear scaling calculation for optical-absorption spectra of large hydrogenated silicon nanocrystallites*. Phys. Rev. B **56**, 4348 (1997).

[46] T. Iitaka and T. Ebisuzaki. *Efficient algorithm for calculating two-photon absorption spectra*. Phys. Rev. E **60**, 1178 (1999).

[47] T. Iitaka and T. Ebisuzaki. *Non-degenerate two photon absorption spectra of Si nanocrystallites*. Mic. Eng. **47**, 321 (1999).

[48] S. Nomura, T. Iitaka, X. Zhao, T. Sugano, and Y. Aoyagi. *Quantum-size effect in model nanocrystalline/amorphous mixed-phase silicon structures*. Phys. Rev. B **59**, 10309 (1999).

[49] T. Iitaka and T. Ebisuzaki. *Calculating response functions in time domain with nonorthonormal basis sets*. Phys. Rev. E **61**, 3314 (2000).

[50] P. De Vries and H. De Raedt. *Solution of the time-dependent Schrödinger equation for two-dimensional spin-$\frac{1}{2}$ Heisenberg systems*. Phys. Rev. B **47**, 7929 (1993).

[51] A. H. Hams and H. De Raedt. *Fast Algorithm for Finding the Eigenvalue Distribution of Very Large Matrices*. Phys. Rev. E **62**, 4365 (2000).

[52] R. Sprik, B. van Tiggelen, and A. Lagendijk. *Optical emission in periodic dielectrics*. Europhys. Lett. **35**, 265 (1996).

[53] P. M. Valanju, R. M. Walser, and A. P. Valanju. *Wave Refraction in Negative-Index Media: Always Positive and Very Inhomogeneous*. Phys. Rev. Lett. **88**, 187401 (2002).

[54] J. B. Pendry and D. R. Smith. *Comment on "Wave Refraction in Negative-Index Media: Always Positive and Very Inhomogeneous"*. Phys. Rev. Lett. **90**, 029703 (2003).

[55] P. M. Valanju, R. M. Walser, and A. P. Valanju. *Valanju, Walser, and Valanju Reply: Phys Rev. Lett. 90, 029704 (2003)*. Phys. Rev. Lett. **90**, 029704 (2003).

[56] Z. M. Zhang and K. Park. *On the Group Front and Group Velocity in a Dispersive Medium Upon Refraction From a Nondispersive Medium*. J. Heat Transfer **126**, 244 (2004).

[57] A. Bers. *Note on group velocity and energy propagation*. Am. J. Phys. **68**, 482 (2000).

[58] K. Sakoda. *Optical Properties of Photonic Crystals*. 2nd edition (Springer-Verlag, New York, 2005).

[59] A. Dogariu, A. Kuzmich, and L. J. Wang. *Transparent anomalous dispersion and superluminal light-pulse propagation at a negative group velocity*. Phys. Rev. A **63**, 053806 (2001).

[60] L. J. Wang, A. Kuzmich, and A. Dogariu. *Gain-assisted superluminal light propagation*. Nature **406**, 277 (2000).

[61] A. Moroz. *http://www.wave-scattering.com/negative.html*.

[62] H. Lamb. *On group-velocity*. Proc. London Math. Soc. **1**, 473 (1904).

[63] L. Brillouin. *Wave propagation and group velocity* (Acamemic press, New York, 1960).

[64] V. G. Veselago. *The electrodynamics of substances with simultaneously negative values of ε and μ.* Sov. Phys. Usp. **10**, 509 (1968). [Translation from the original Russian version in Usp. Fiz. Nauk. **92**, 517-526 (1967). This year was mislabeled in the translation as 1964.].

[65] S. Foteinopoulou and C. M. Soukoulis. *Negative refraction and left-handed behavior in two-dimensional photonic crystals.* Phys. Rev. B **67**, 235107 (2003).

[66] Z. Ye. *About negative refraction and left handed materials.* Chinese J. Phys. **43**, 1 (2005).

[67] A. Lakhtakia, M. W. McCall, W. S. Weiglhofer, J. Geradin, and J. Wang. *On Mediums with Negative Phase Velocity: a Brief Overview.* Arch. Elektr. Ueber. **56**, 407 (2002).

[68] I. V. Lindell, S. A. Tretyakov, K. I. Nikoskinen, and S. Ilvonen. *BW media - media with negative parameters, capable of supporting backward waves.* Microw. Opt. Tech. Lett. **31**, 129 (2001).

[69] I. V. Lindell and S. Ilvonen. *Waves in a slab of uniaxial BW medium.* J. of Electromagn. Waves and Appl. **16**, 303 (2002).

[70] R. G. E. Hutter. *Beam and wave electronics in microwave tubes* (Van Nostrand, Princeton, NJ, 1960), p. 220.

[71] P. E. Mayes, G. A. Deschamps, and W. T. Patton. *Backward-wave radiation from periodic structures and application to the design of frequency-independent antennas.* Proc. IRE **49**, 962 (1961).

[72] J. L. Altman. *Microwave circuits* (Van Nostrand, Princeton, NJ, 1964), chapter 7, p. 304.

[73] R. E. Collin. *Foundations for microwave engineering* (McGraw-Hill, New York, 1966).

[74] A. A. Oliner and T. Tamir. *Backward waves on isotropic plasma slabs.* J. Appl. Phys **33**, 231 (1962).

[75] H. C. Pocklington. *Growth of a wave-group when the group-velocity is negative.* Nature **71**, 607 (1905).

[76] R. W. Ziolkowski. *Wave propagation in media having negative permittivity and permeability.* Phys. Rev. E **64**, 056625 (2001).

[77] R. W. Ziolkowski. *Pulsed and CW Gaussian beam interactions with double negative metamaterial slabs.* Opt. Express **11**, 662 (2003).

[78] J. B. Pendry and D. R. Smith. *Reversing light with negative refraction.* Phys. Today **57**, 37 (2004).

[79] S. Foteinopoulou, E. N. Economou, and C. M. Soukoulis. *Refraction in Media with a Negative Refractive Index.* Phys. Rev. Lett. **90**, 107402 (2003).

[80] J. B. Brock, A. A. Houck, and I. L. Chuang. *Focusing inside negative index materials.* Appl. Phys. Lett. **85**, 2472 (2004).

[81] J. B. Pendry. *Negative Refraction Makes a Perfect Lens.* Phys. Rev. Lett. **85**, 3966 (2000).

[82] R. A. Silin. *Possibility of creating plane-parallel lenses.* Opt. Spectrosc. **44**, 109 (1978). [Translation from the original Russian version in Opt. Spektrosk. USSR **44**, 189 (1978).].

[83] L. I. Mandelshtam. *Complete Collected Works* (Akad. Nauk SSSR, Moscow, 1947), volume 2, p. 334.

[84] L. I. Mandelshtam. *Complete Collected Works* (Akad. Nauk SSSR, Moscow, 1950), volume 5, p. 419.

[85] R. A. Silin. *Optical properties of artificial dielectrics.* Izv. Vyssh. Uchebn. Zaved. Radiofiz. **15**, 809 (1972).

[86] G. W. 't Hooft. *Comment on "Negative refraction makes a perfect lens"*. Phys. Rev. Lett. **87**, 249701 (2001).

[87] J. M. Williams. *Some Problems with Negative Refraction*. Phys. Rev. Lett. **87**, 249703 (2001).

[88] N. Garcia and M. Nieto-Vesperinas. *Left-Handed Materials Do Not Make a Perfect Lens*. Phys. Rev. Lett. **88**, 207403 (2002).

[89] N. Garcia and M. Nieto-Vesperinas. *Erratum: Left-handed materials do not make a perfect lens [Phys. Rev. Lett. 88, 207403 (2002)]*. Phys. Rev. Lett. **90**, 229903 (2003).

[90] M. Nieto-Vesperinas and N. Garcia. *Nieto-Vesperinas and Garcia Reply:*. Phys. Rev. Lett. **91**, 099702 (2003).

[91] Z. Ye. *Optical transmission and reflection of perfect lenses by left handed materials*. Phys. Rev. B **67**, 193106 (2003).

[92] N. Fang and X. Zhang. *Imaging properties of a metamaterial superlens*. Appl. Phys. Lett. **82**, 161 (2003).

[93] P. F. Loschialpo, D. L. Smith, D. W. Forester, F. J. Rachford, and J. Schelleng. *Electromagnetic waves focused by a negative-index planar lens*. Phys. Rev. E **67**, 025602 (2003).

[94] P. F. Loschialpo, D. W. Forester, D. L. Smith, F. J. Rachford, and C. Monzon. *Optical properties of an ideal homogeneous causal left-handed material slab*. Phys. Rev. E **70**, 036605 (2004).

[95] J. B. Pendry. *Negative refraction*. Contemporary Physics **45**, 191 (2004).

[96] D. R. Smith, J. B. Pendry, and M. C. K. Wiltshire. *Metamaterials and Negative Refractive Index*. Science **305**, 788 (2004).

[97] J. B. Pendry, A. J. Holden, W. J. Stewart, and I. Youngs. *Extremely Low Frequency Plasmons in Metallic Mesostructures*. Phys. Rev. Lett. **76**, 4773 (1996).

[98] J. B. Pendry, A. J. Holden, D. J. Robbins, and W. J. Stewart. *Low frequency plasmons in thin-wire structures*. J. Phys.: Condens. Matter **10**, 4785 (1998).

[99] J. B. Pendry, A. J. Holden, D. J. Robbins, and W. J. Stewart. *Magnetism from Conductors, and Enhanced Non-Linear Phenomena*. IEEE trans. Microwave Theory Tech. **47**, 2075 (1999).

[100] D. R. Smith, W. J. Padilla, D. C. Vier, S. C. Nemat-Nasser, and S. Schultz. *Composite Medium with Simultaneously Negative Permeability and Permittivity*. Phys. Rev. Lett. **84**, 4184 (2000).

[101] R. A. Shelby, D. R. Smith, S. C. Nemat-Nasser, and S. Schultz. *Microwave transmission through a two-dimensional, isotropic, left-handed metamaterial*. Appl. Phys. Lett. **78**, 489 (2001).

[102] R. A. Shelby, D. R. Smith, and S. Schultz. *Experimental Verification of a Negative Index of Refraction*. Science **292**, 77 (2001).

[103] N. Garcia and M. Nieto-Vesperinas. *Is there an experimental verification of a negative index of refraction yet?* Opt. Lett. **27**, 885 (2002).

[104] A. Houck, J. B. Brock, and I. L. Chuang. *Experimental observations of a left-handed material that obeys Snell's law*. Phys. Rev. Lett. **90**, 137401 (2003).

[105] C. G. Parazzoli, R. B. Greegor, K. Li, B. E. C. Koltenbah, and M. Tanielian. *Experimental verification and simulation of negative index of refraction using Snell's law*. Phys. Rev. Lett. **90**, 107401 (2003).

[106] A. Grbic and G. V. Eleftheriades. *Overcoming the Diffraction Limit with a Planar Left-Handed Transmission-Line Lens*. Phys. Rev. Lett. **92**, 117403 (2004).

[107] J. Pendry. *A Chiral Route to Negative Refraction*. Science **306**, 1353 (2004).

[108] G. V. Eleftheriades, A. K. Iyer, and P. C. Kremer. *Planar Negative Refractive Index Media Using*

Periodically L-C Loaded Transmission Lines. IEEE trans. Microwave Theory Tech. **50**, 2702 (2002).

[109] A. K. Iyer, P. C. Kremer, and G. V. Eleftheriades. *Experimental and theoretical verification of focusing in a large, periodically loaded transmission line negative refractive index metamaterial*. Opt. Express **11**, 696 (2003).

[110] A. Grbic and G. V. Eleftheriades. *Experimental verification of backward-wave radiation from a negative refractive index metamaterial*. J. Appl. Phys **92**, 5930 (2002).

[111] A. Grbic and G. V. Eleftheriades. *Growing evanescent waves in negative-refractive-index transmission-line media*. Appl. Phys. Lett. **82**, 1815 (2003).

[112] A. Grbic and G. V. Eleftheriades. *Subwavelength Focusing Using a Negative-Refractive-Index Transmission Line Lens*. IEEE Antennas Wireless Propagat. Lett. **2**, 186 (2003).

[113] E. Cubukcu, K. Aydin, E. Ozbay, S. Foteinopolou, and C. M. Soukoulis. *Electromagnetic waves: Negative refraction by photonic crystals*. Nature **423**, 604 (2003).

[114] E. Cubukcu, K. Aydin, E. Ozbay, S. Foteinopolou, and C. M. Soukoulis. *Subwavelength Resolution in a Two-Dimensional Photonic-Crystal-Based Superlens*. Phys. Rev. Lett. **91**, 207401 (2003).

[115] P. V. Parimi, W. T. Lu, P. Vodo, and S. Sridhar. *Photonic crystals: Imaging by flat lens using negative refraction*. Nature **426**, 404 (2003).

[116] P. V. Parimi, W. T. Lu, P. Vodo, J. Sokoloff, J. S. Derov, and S. Sridhar. *Negative Refraction and Left-Handed Electromagnetism in Microwave Photonic Crystals*. Phys. Rev. Lett. **92**, 127401 (2004).

[117] P. Vodo, P. V. Parimi, W. T. Lu, S. Sridhar, and R. Wing. *Microwave photonic crystal with tailor-made negative refractive index*. Appl. Phys. Lett. **85**, 1858 (2004).

[118] Z. Lu, C. Chen, C. A. Schuetz, S. Shi, J. A. Murakowski, G. J. Schneider, and D. W. Prather. *Subwavelength imaging by a flat cylindrical lens using optimized negative refraction*. Appl. Phys. Lett. **87**, 091907 (2005).

[119] A. Berrier, M. Mulot, M. Swillo, M. Qiu, L. Thylén, A. Talneau, and S. Anand. *Negative Refraction at Infrared Wavelengths in a Two-Dimensional Photonic Crystal*. Phys. Rev. Lett. **93**, 073902 (2004).

[120] A. Martinez, H. Miguez, A. Griol, and J. Marti. *Experimental and theoretical analysis of the self-focusing of light by a photonic crystal lens*. Phys. Rev. B **69**, 165119 (2004).

[121] K. Guven, K. Aydin, K. B. Alici, C. M. Soukoulis, and E. Ozbay. *Spectral negative refraction and focusing analysis of a two-dimensional left-handed photonic crystal lens*. Phys. Rev. B **70**, 205125 (2004).

[122] R. Moussa, S. Foteinopoulou, L. Zhang, G. Tuttle, K. Guven, E. Ozbay, and C. M. Soukoulis. *Negative refraction and superlens behavior in a two-dimensional photonic crystal*. Phys. Rev. B **71**, 085106 (2005).

[123] Z. Lu, S. Shi, C. A. Schuetz, and D. W. Prather. *Experimental demonstration of negative refraction imaging in both amplitude and phase*. Opt. Express **13**, 2007 (2005).

[124] E. Ozbay, I. Bulu, K. Aydin, H. Caglayan, K. B. Alici, and K. Guven. *Highly Directive Radiation and Negative Refraction Using Photonic Crystals*. Laser Phys. **15**, 217 (2005).

[125] C. Luo, S. G. Johnson, and J. D. Joannopoulos. *All-angle negative refraction in a three-dimensionally periodic photonic crystal*. Appl. Phys. Lett. **81**, 2352 (2002).

[126] X. Ao and S. He. *Three-dimensional photonic crystal of negative refraction achieved by interference lithography*. Opt. Lett. **29**, 2542 (2004).

[127] Z. Lu, J. A. Murakowski, C. A. Schuetz, S. Shi, G. J. Schneider, and D. W. Prather. *Three-Dimensional Subwavelength Imaging by a Photonic-Crystal Flat Lens Using Negative Refraction at Microwave Frequencies*. Phys. Rev. Lett. **95**, 153901 (2005).

[128] N. Fang, H. Lee, C. Sun, and X. Zhang. *Sub-Diffraction-Limited Optical Imaging with a Silver Superlens*. Science **308**, 534 (2005).

[129] N. Fang, Z. Liu, T.-J. Yen, and X. Zhang. *Experimental study of transmission enhancement of evanescent waves through silver films assisted by surface plasmon excitation*. Appl. Phys. A **80**, 1315 (2005).

[130] Z. Liu, N. Fang, T.-J. Yen, and X. Zhang. *Rapid growth of evanescent wave by a silver superlens*. Appl. Phys. Lett. **83**, 5184 (2003).

[131] N. Fang, Z. Liu, T.-J. Yen, and X. Zhang. *Regenerating evanescent waves from a silver superlens*. Opt. Express **11**, 682 (2003).

[132] S. John. *Strong localization of photons in certain disordered dielectric superlattices*. Phys. Rev. Lett. **58**, 2468 (1987).

[133] K. M. Ho, C. T. Chan, and C. M. Soukoulis. *Existence of a photonic gap in periodic dielectric structures*. Phys. Rev. Lett. **65**, 3152 (1990).

[134] O. Toader and S. John. *Slanted-pore photonic band-gap materials*. Phys. Rev. E **71**, 036605 (2005).

[135] K. M. Ho, C. T. Chan, C. M. Soukoulis, R. Biswas, and M. Sigalas. *Photonic band gaps in three dimensions: New layer-by-layer periodic structures*. Solid State Commun. **89**, 413 (1994).

[136] H. S. Sözüer and J. P. Dowling. *Photonic Band Calculations for Woodpile Structures*. J. Mod. Opt. **41**, 231 (1994).

[137] A. Blanco, E. Chomski, S. Grabtchak, *et al. Large-scale synthesis of a silicon photonic crystal with a complete three-dimensional bandgap near 1.5 micrometres*. Nature **405**, 437 (2000).

[138] J. E. G. J. Wijnhoven and W. L. Vos. *Preparation of Photonic Crystals Made of Air Spheres in Titania*. Science **281**, 802 (1998).

[139] A. Chutinan and S. Noda. *Spiral three-dimensional photonic-band-gap structure*. Phys. Rev. B **57**, R2006 (1998).

[140] Y.-C. Tsai, J. B. Pendry, and K. W.-K. Shung. *Absolute three-dimensional photonic band gap in the infrared regime in woven structures*. Phys. Rev. B **59**, R10401 (1999).

[141] O. Toader and S. John. *Square spiral photonic crystals: Robust architecture for microfabrication of materials with large three-dimensional photonic band gaps*. Phys. Rev. E **66**, 016610 (2002).

[142] O. Toader and S. John. *Proposed Square Spiral Microfabrication Architecture for Large Three-Dimensional Photonic Band Gap Crystals*. Science **292**, 1133 (2001).

[143] M. O. Jensen and M. J. Brett. *Square spiral 3D photonic bandgap crystals at telecommunications frequencies*. Opt. Express **13**, 3348 (2005).

[144] A. Moroz. *Three-Dimensional Complete Photonic-Band-gap Structures in the Visible*. Phys. Rev. Lett. **83**, 5274 (1999).

[145] Z. Wang, C. T. Chan, W. Zhang, N. Ming, and P. Sheng. *Three-dimensional self-assembly of metal nanoparticles: Possible photonic crystal with a complete gap below the plasma frequency*. Phys. Rev. B **64**, 113108 (2001).

[146] L. Martin-Moreno, F. J. Garcia-Vidal, and A. M. Somoza. *Self-Assembled Triply Periodic Minimal Surfaces as Molds for Photonic Band Gap Materials*. Phys. Rev. Lett. **83**, 73 (1999).

[147] V. Babin, P. Garstecki, and R. Holyst. *Photonic properties of multicontinuous cubic phases*. Phys. Rev. B **66**, 235120 (2002).

[148] M. Maldovan, A. M. Urbas, N. Yufa, W. C. Carter, and E. L. Thomas. *Photonic properties of bicontinuous cubic microphases*. Phys. Rev. B **65**, 165123 (2002).

[149] K. Michielsen and J. S. Kole. *Photonic band gaps in materials with triply periodic surfaces and related tubular structures*. Phys. Rev. B **68**, 115107 (2003).

[150] M. Maldovan and E. L. Thomas. *Diamond structured photonic crystals*. Nature Materials **3**, 593 (2004).

[151] M. Maldovan and E. L. Thomas. *Six connected dielectric networks with simple cubic symmetry*. J. Opt. Soc. Am. B **22**, 466 (2005).

[152] E. Yablonovitch, T. J. Gmitter, R. D. Meade, A. M. Rappe, K. D. Brommer, and J. D. Joannopoulos. *Donor and acceptor modes in photonic band structure*. Phys. Rev. Lett. **67**, 3380 (1991).

[153] C. C. Cheng and A. Scherer. *Fabrication of photonic band-gap crystals*. J. Vac. Sci. Technol. B **13**, 2696 (1995).

[154] A. Chelnokov, K. Wang, S. Rowson, P. Garoche, and J.-M. Lourtioz. *Near-infrared Yablonovite-like photonic crystals by focused-ion-beam etching of macroporous silicon*. Appl. Phys. Lett. **77**, 2943 (2000).

[155] W. L. Vos, R. Sprik, A. van Blaaderen, A. Imhof, A. Lagendijk, and G. H. Wegdam. *Strong effects of photonic band structures on the diffraction of colloidal crystals*. Phys. Rev. B **53**, 16231 (1996).

[156] Y. A. Vlasov, X.-Z. Bo, J. C. Sturm, and D. J. Norris. *On-chip natural assembly of silicon photonic bandgap crystals*. Nature **414**, 289 (2001).

[157] M. Campbell, D. N. Sharp, M. T. Harrison, R. G. Denning, and A. J. Turberfield. *Fabrication of photonic crystals for the visible spectrum by holographic lithography*. Nature **404**, 53 (2000).

[158] S. Shoji and S. Kawata. *Photofabrication of three-dimensional photonic crystals by multibeam laser interference into a photopolymerizable resin*. Appl. Phys. Lett. **76**, 2668 (2000).

[159] H.-B. Sun, S. Matsuo, and H. Misawa. *Three-dimensional photonic crystal structures achieved with two-photon-absorption photopolymerization of resin*. Appl. Phys. Lett. **74**, 786 (1999).

[160] A. Chelnokov, S. Rowson, J.-M. Lourtioz, L. Duvillaret, and J.-L. Coutaz. *Terahertz characterisation of mechanically machined 3D photonic crystal*. Electron. Lett. **33**, 1981 (1997).

[161] A. Feigel, Z. Kotler, B. Sfez, A. Arsh, M. Klebanov, and V. Lyubin. *Chalcogenide glass-based three-dimensional photonic crystals*. Appl. Phys. Lett. **77**, 3221 (2000).

[162] J. G. Fleming, S. Y. Lin, I. El-Kady, R. Biswas, and K. M. Ho. *All-metallic three-dimensional photonic crystals with a large infrared bandgap*. Nature **417**, 52 (2002).

[163] S. Y. Lin, J. G. Fleming, D. L. Hetherington, B. K. Smith, R. Biswas, K. M. Ho, M. M. Sigalas, W. Zubrzycki, S. R. Kurtz, and J. Bur. *A three-dimensional photonic crystal operating at infrared wavelengths*. Nature **394**, 251 (1998).

[164] S. Noda, K. Tomoda, N. Yamamoto, and A. Chutinan. *Full Three-Dimensional Photonic Bandgap Crystals at Near-Infrared Wavelengths*. Science **289**, 604 (2000).

[165] E. Ozbay, A. Abeyta, G. Tuttle, M. Tringides, R. Biswas, C. T. Chan, C. M. Soukoulis, and K. M. Ho. *Measurement of a three-dimensional photonic band gap in a crystal structure made*

of dielectric rods. Phys. Rev. B **50**, 1945 (1994).

[166] K. Aoki, H. T. Miyazaki, H. Hirayama, K. Inoshita, T. Baba, K. Sakoda, N. Shinya, and Y. Aoyagi. *Microassembly of semiconductor three-dimensional photonic crystals*. Nature **2**, 117 (2003).

[167] R. de la Rue. *Photonic crystals: Microassembly in 3D*. Nature **2**, 74 (2003).

[168] B. Gralak, S. Enoch, and G. Tayeb. *Anomalous refractive properties of photonic crystals*. J. Opt. Soc. Am. A **17**, 1012 (2000).

[169] J. P. Dowling and C. M. Bowden. *Anomalous index of refraction in photonic bandgap materials*. J. Mod. Opt. **41**, 345 (1994).

[170] X. Zhang. *Image resolution depending on slab thickness and object distance in a two-dimensional photonic-crystal-based superlens*. Phys. Rev. B **70**, 195110 (2004).

[171] X. Wang, Z. F. Ren, and K. Kempa. *Unrestricted superlensing in a triangular two-dimensional photonic crystal*. Opt. Express **12**, 2919 (2004).

[172] S. Xiao, M. Qiu, Z. Ruan, and S. He. *Influence of the surface termination to the point imaging by a photonic crystal slab with negative refraction*. Appl. Phys. Lett. **85**, 4269 (2004).

[173] X. Wang, Z. F. Ren, and K. Kempa. *Improved superlensing in two-dimensional photonic crystals with a basis*. Appl. Phys. Lett. **86**, 061105 (2005).

[174] X. Wang and K. Kempa. *Effects of disorder on subwavelength lensing in two-dimensional photonic crystal slabs*. Phys. Rev. B **71**, 085101 (2005).

[175] A. Martinez and J. Marti. *Analysis of wave focusing inside a negative-index photonic-crystal slab*. Opt. Express **13**, 2858 (2005).

[176] S. He and Z. Ruan. *A completely open cavity realized with photonic crystal wedges*. J. Zhejiang Univ. SCI **6A**, 355 (2005).

[177] S. He, Y. Jin, Z. Ruan, and J. Kuang. *On subwavelength and open resonators involving metamaterials of negative refraction index*. New J. of Phys. **7**, 210 (2005).

[178] Z. Ruan and S. He. *Open cavity formed by a photonic crystal with negative effective index of refraction*. Opt. Lett. **30**, 2308 (2005).

[179] C. Luo, S. G. Johnson, J. D. Joannopoulos, and J. B. Pendry. *All-angle negative refraction without negative effective index*. Phys. Rev. B **65**, 201104 (2002).

[180] C. Luo, M. Ibanescu, S. G. Johnson, and J. D. Joannopoulos. *Cerenkov Radiation in Photonic Crystals*. Science **299**, 368 (2003).

[181] Z. Y. Li and L. L. Lin. *Evaluation of lensing in photonic crystal slabs exhibiting negative refraction*. Phys. Rev. B **68**, 245110 (2003).

[182] S. He, Z. Ruan, L. Chen, and J. Shen. *Focusing properties of a photonic crystal slab with negative refraction*. Phys. Rev. B **70**, 115113 (2004).

[183] H. T. Chien, H. T. Tang, C. H. Kuo, C. C. Chen, and Z. Ye. *Directed diffraction without negative refraction*. Phys. Rev. B **70**, 113101 (2004).

[184] C.-H. Kuo and Z. Ye. *Band gap or negative refraction effects?* cond-mat/0310423 (2003).

[185] C.-H. Kuo and Z. Ye. *Negative-refraction-like behavior revealed by arrays of dielectric cylinders*. Phys. Rev. E **70**, 026608 (2004).

[186] C.-H. Kuo and Z. Ye. *Optical transmission of photonic crystal structures formed by dielectric cylinders: Evidence for non-negative refraction*. Phys. Rev. E **70**, 056608 (2004).

[187] L.-S. Chen, C.-H. Kuo, and Z. Ye. *Guiding optical flows by photonic crystal slabs made of dielectric cylinders*. Physical Review E **69**, 066612 (2004).

[188] C.-H. Kuo and Z. Ye. *Flat lens imaging does not need negative refraction*. cond-mat/0312288 (2004).

[189] J. L. Garcia-Pomar and M. Nieto-Vesperinas. *Waveguiding, collimation and subwavelength concentration in photonic crystals*. Opt. Express **13**, 7997 (2005).

[190] S. G. Johnson and J. D. Joannopoulos. *Block-iterative frequency-domain methods for Maxwell's equations in a planewave basis*. Opt. Express **8**, 173 (2001).

[191] N. W. Ashcroft and N. D. Mermin. *Solid State Physics* (Saunders college, Philadelphia, 1976).

[192] K. Ohtaka, T. Ueta, and Y. Tanabe. *Photonic Bands Using Vector Spherical Waves. IV. Analogy of Optics of Photonic Crystals to That of Anisotropic Crystals*. J. Phys. Soc. Jpn. **65**, 3068 (1996).

[193] P. S. J. Russell. *Interference of integrated Floquet-Bloch waves*. Phys. Rev. A **33**, 3232 (1986).

[194] P. S. J. Russell. *Optics of Floquet-Bloch waves in dielectric gratings*. Appl. Phys. B **39**, 231 (1986).

[195] R. Zengerle. *Light Propagation in Singly and Doubly Periodic Planar Waveguides*. J. of Mod. Opt. **34**, 1987 (1987).

[196] Z. Ruan, M. Qiu, S. Xiao, S. He, and L. Thylen. *Coupling between plane waves and Bloch waves in photonic crystals with negative refraction*. Phys. Rev. B **71**, 045111 (2005).

[197] P. Yeh. *Electromagnetic propagation in birefringent layered media*. J. Opt. Soc. Am. **69**, 742 (1979).

[198] S. G. Johnson, S. Fan, P. R. Villeneuve, J. D. Joannopoulos, and L. A. Kolodziejski. *Guided modes in photonic crystal slabs*. Phys. Rev. B **60**, 5751 (1999).

[199] M. Qiu. *Effective index method for heterostructure-slab-waveguide-based two-dimensional photonic crystals*. Appl. Phys. Lett. **81**, 1163 (2002).

[200] M. Kafesaki, M. Agio, and C. M. Soukoulis. *Waveguides in finite-height two-dimensional photonic crystals*. J. Opt. Soc. Am. B **19**, 2232 (2002).

[201] M. Kafesaki, C. M. Soukoulis, and M. Agio. *Losses and transmission in two-dimensional slab photonic crystals*. J. Appl. Phys **96**, 4033 (2004).

[202] U. Grüning, V. Lehmann, and C. M. Engelhardt. *Two-dimensional infrared photonic band gap structure based on porous silicon*. Appl. Phys. Lett. **66**, 3254 (1995).

[203] H. W. Lau, G. J. Parker, R. Greef, and M. Holling. *High aspect ratio submicron silicon pillars fabricated by photoassisted electrochemical etching and oxidation*. Appl. Phys. Lett. **67**, 1877 (1995).

[204] U. Grüning, V. Lehmann, S. Ottow, and K. Busch. *Macroporous silicon with a complete two-dimensional photonic band gap centered at 5 mu m*. Appl. Phys. Lett. **68**, 747 (1996).

[205] J. Schilling, R. B. Wehrspohn, A. Birner, *et al. A model system for two-dimensional and three-dimensional photonic crystals: macroporous silicon*. J. Opt. A: Pure Appl. Opt. **3**, S121 (2001).

[206] M. Notomi, H. Suzuki, and T. Tamamura. *Directional lasing oscillation of two-dimensional organic photonic crystal lasers at several photonic band gaps*. Appl. Phys. Lett. **78**, 1325 (2001).

[207] R. Moussa, S. Foteinopoulou, and C. M. Soukoulis. *Delay-time investigation of electromagnetic waves through homogeneous medium and photonic crystal left-handed materials*. Appl. Phys. Lett. **85**, 1125 (2004).

[208] E. Moreno, F. J. Garcia-Vidal, and L. Martin-Moreno. *Enhanced transmission and beaming of light via photonic crystal surface modes*. Phys. Rev. B **69**, 121402 (2004).

[209] P. Kramper, M. Agio, C. M. Soukoulis, A. Birner, F. Muller, R. B. Wehrspohn, U. Gosele, and

V. Sandoghdar. *Highly Directional Emission from Photonic Crystal Waveguides of Subwavelength Width*. Phys. Rev. Lett. **92**, 113903 (2004).

[210] E. M. Purcell. *Spontaneous emission probabilities at radio frequencies*. Phys. Rev. **69**, 681 (1946).

[211] L. E. Ballentine. *Quantum Mechanics: A Modern Development* (World Scientific, Singapore, 2003).

[212] H. Morawitz. *Self-Coupling of a Two-Level System by a Mirror*. Phys. Rev. **187**, 1792 (1969).

[213] H. Kuhn. *Classical Aspects of Energy Transfer in Molecular Systems*. J. Chem. Phys. **53**, 101 (1970).

[214] K. H. Tews. *On the variation of luminescence lifetimes. The approximations of the approximative methods*. J. Lumin. **9**, 223 (1974).

[215] H. Chew. *Radiation and lifetimes of atoms inside dielectric particles*. Phys. Rev. A **38**, 3410 (1988).

[216] J. P. Dowling, M. O. Scully, and F. Demartini. *Radiation pattern of a classical dipole in a cavity*. Opt. Commun. **82**, 415 (1991).

[217] J. P. Dowling and C. M. Bowden. *Atomic emission rates in inhomogeneous media with applications to photonic band structures*. Phys. Rev. A **46**, 612 (1992).

[218] H. Rigneault and S. Monneret. *Modal analysis of spontaneous emission in a planar microcavity*. Phys. Rev. A **54**, 612 (1996).

[219] G. S. Agarwal. *Quantum electrodynamics in the presence of dielectrics and conductors. IV. General theory for spontaneous emission in finite geometries*. Phys. Rev. A **12**, 1475 (1975).

[220] A. O. Barut and J. P. Dowling. *Quantum electrodynamics based on self-energy: Spontaneous emission in cavities*. Phys. Rev. A **36**, 649 (1987).

[221] X.-P. Feng and K. Ujihara. *Quantum theory of spontaneous emission in a one-dimensional optical cavity with two-side output coupling*. Phys. Rev. A **41**, 2668 (1990).

[222] R. J. Glauber and M. L. Lewenstein. *Quantum optics of dielectric media*. Phys. Rev. A **43**, 467 (1991).

[223] G. Björk, S. Machida, Y. Yamamoto, and K. Igeta. *Modification of spontaneous emission rate in planar dielectric microcavity structures*. Phys. Rev. A **44**, 669 (1991).

[224] S. M. Barnett, B. Huttner, and R. Loudon. *Spontaneous emission in absorbing dielectric media*. Phys. Rev. Lett. **68**, 3698 (1992).

[225] H. Khosravi and R. Loudon. *Vacuum field fluctuations and spontaneous emission in a dielectric slab*. Proc. R. Soc. London, Ser. A **436**, 373 (1992).

[226] F. D. Martini, F. Cairo, P. Mataloni, and F. Verzegnassi. *Thresholdless microlaser*. Phys. Rev. A **46**, 4220 (1992).

[227] D. G. Deppe, C. Lei, C. C. Lin, and D. L. Huffaker. *Spontaneous Emission from Planar Microstructures*. J. Mod. Opt. **41**, 325 (1994).

[228] K. Kakasu and Y. Kim. *Quantization of electromagnetic fields in cavities and spontaneous emission*. Phys. Rev. A **50**, 1830 (1994).

[229] N. Koide and K. Ujihara. *Analysis of spontaneous emission from a planar microcavity-dependence on the refractive index of the cavity region and atomic location*. Opt. Commun. **111**, 381 (1994).

[230] W. Zakowicz and A. Bledowski. *Spontaneous emission in the presence of a dielectric slab*. Phys.

Rev. A **52**, 1640 (1995).

[231] S. M. Barnett and R. Loudon. *Sum Rule for Modified Spontaneous Emission Rates*. Phys. Rev. Lett. **77**, 2444 (1996).

[232] S. M. Barnett, B. Huttner, R. Loudon, and R. Matloob. *Decay of excited atoms in absorbing dielectrics*. J. Phys. B **29**, 3763 (1996).

[233] Y. Xu, J. S. Vučković, R. Lee, O. J. Painter, A. Scherer, and A. Yariv. *Finite-difference time-domain calculation of spontaneous emission lifetime in a microcavity*. J. Opt. Soc. Am. B **16**, 465 (1999).

[234] J.-K. Hwang, H.-Y. Ryu, and Y.-H. Lee. *Spontaneous emission rate of an electric dipole in a general microcavity*. Phys. Rev. B **60**, 4688 (1999).

[235] Y. Xu, R. K. Lee, and A. Yariv. *Quantum analysis and the classical analysis of spontaneous emission in a microcavity*. Phys. Rev. A **61**, 033807 (2000).

[236] J. Vučković, O. Painter, Y. Xu, A. Yariv, and A. Scherer. *Quantum analysis and the classical analysis of spontaneous emission in a microcavity*. IEEE J. Quant. Electr. **35**, 1168 (1999).

[237] J. Martorell and N. M. Lawandy. *Observation of inhibited spontaneous emission in a periodic dielectric structure*. Phys. Rev. Lett. **65**, 1877 (1990).

[238] B. Y. Tong, P. K. John, Y. T. Zhu, Y. S. Liu, S. K. Wong, and W. R. Ware. *Fluorescence-lifetime measurements in monodispersed suspensions of polystyrene particles*. J. Opt. Soc. Am. B **10**, 356 (1993).

[239] E. P. Petrov, V. N. Bogomolov, I. I. Kalosha, and S. V. Gaponenko. *Spontaneous Emission of Organic Molecules Embedded in a Photonic Crystal*. Phys. Rev. Lett. **81**, 77 (1998).

[240] M. Megens, J. E. G. J. Wijnhoven, A. Lagendijk, and W. L. Vos. *Fluorescence lifetimes and linewidths of dye in photonic crystals*. Phys. Rev. A **59**, 4727 (1999).

[241] M. Megens, H. P. Schriemer, A. Lagendijk, and W. L. Vos. *Comment on "Spontaneous Emission of Organic Molecules Embedded in a Photonic Crystal"*. Phys. Rev. Lett. **83**, 5401 (1999).

[242] E. P. Petrov, V. N. Bogomolov, I. I. kalosha, and S. V. Gaponenko. *Petrov et al. Reply:*. Phys. Rev. Lett. **83**, 5402 (1999).

[243] Z.-Y. Li and Z.-Q. Zhang. *Weak photonic band gap effect on the fluorescence lifetime in three-dimensional colloidal photonic crystals*. Phys. Rev. B **63**, 125106 (2001).

[244] A. F. Koenderink, L. Bechger, H. P. Schriemer, A. Lagendijk, and W. L. Vos. *Broadband Fivefold Reduction of Vacuum Fluctuations Probed by Dyes in Photonic Crystals*. Phys. Rev. Lett. **88**, 143903 (2002).

[245] S. Ogawa, M. Imada, S. Yoshimoto, M. Okano, and S. Noda. *Control of Light Emission by 3D Photonic Crystals*. Science **305**, 227 (2004).

[246] P. Lodahl, A. F. van Driel, I. S. Nikolaev, A. Irman, K. Overgaag, D. Vanmaekelbergh, and W. L. Vos. *Controlling the dynamics of spontaneous emission from quantum dots by photonic crystals*. Nature **430**, 654 (2004).

[247] M. Fujita, S. Takahashi, Y. Tanaka, T. Asano, and S. Noda. *Simultaneous Inhibition and Redistribution of Spontaneous Light Emission in Photonic Crystals*. Science **308**, 1296 (2005).

[248] A. Badolato, K. Hennessy, M. Atature, J. Dreiser, E. Hu, P. M. Petroff, and A. Imamoglu. *Deterministic Coupling of Single Quantum Dots to Single Nanocavity Modes*. Science **308**, 1158 (2005).

[249] A. Kress, F. Hofbauer, N. Reinelt, M. Kaniber, H. J. Krenner, R. Meyer, G. Bohm, and J. J.

Finley. *Manipulation of the spontaneous emission dynamics of quantum dots in two-dimensional photonic crystals*. Phys. Rev. B **71**, 241304 (2005).

[250] D. Englund, D. Fattal, E. Waks, G. Solomon, B. Zhang, T. Nakaoka, Y. Arakawa, Y. Yamamoto, and J. Vuckovic. *Controlling the Spontaneous Emission Rate of Single Quantum Dots in a Two-Dimensional Photonic Crystal*. Phys. Rev. Lett. **95**, 013904 (2005).

[251] R. Wang, X.-H. Wang, B.-Y. Gu, and G.-Z. Yang. *Local density of states in three-dimensional photonic crystals: Calculation and enhancement effects*. Phys. Rev. B **67**, 155114 (2003).

[252] T. Suzuki and P. K. L. Yu. *Dispersion relation at point L in the photonic band structure of the face-centered-cubic lattice with active or conductive dielectric media*. J. Opt. Soc. Am. B **12**, 570 (1995).

[253] K. Busch and S. John. *Photonic band gap formation in certain self-organizing systems*. Phys. Rev. E **58**, 3896 (1998).

[254] Z. Li, L.-L. Lin, and Z.-Q. Zhang. *Spontaneous Emission from Photonic Crystals: Full Vectorial Calculations*. Phys. Rev. Lett. **84**, 4341 (2000).

[255] Z.-Y. Li and Y. Xia. *Full vectorial model for quantum optics in three-dimensional photonic crystals*. Phys. Rev. A **63**, 043817 (2001).

Publications

- C. Shen, K. Michielsen, H. De Raedt, "*Spontaneous-emission rate in microcavities: Application to two-dimensional photonic crystals*", Physical Review Letters **96**, 120401 (2006).
- C. Shen, K. Michielsen, H. De Raedt, "*Image transfer by cascaded stack of photonic crystal and air layers*", Optics Express **14**, 879 (2006).
- C. Shen, J. M. Greenberg, W. A. Schutte, E. F. van Dishoeck, "*Cosmic ray induced explosive chemical desorption in dense clouds*", Astronomy & Astrophysics **415**, 203 (2004).
- M. Kong, Y. Qiu, C. Shen, J. Deng, B. Zhang, J. Hu, "*New Variable Stars Discovered as By-product of the Beijing Astronomical Observatory Supernova Survey*", Chinese Journal of Astronomy and Astrophysics **2**, 463-473 (2002).
- J. M. Greenberg, C. Shen, "*Cosmic Dust in 21st Century*", Astrophysics and Space Science, **269-270**, 33 (1999).
- C. Shen, J.-Y. Hu, "*The evolutionary status of HD 104237, ϵ Cha and HD 100546*", Acta Astrophys. Sinica **19**, 292 (1999) (in Chinese); Chinese Astronomy and Astrophysics **23**, 493 (1999) (English translation).

Summary

A photonic crystal is a periodic dielectric structure with a lattice constant of the order of the wavelength of the electromagnetic wave that one wants to control. In photonic crystals, the magnetic permeability is equal to one and the electrical permittivity periodically varies in space and is positive. Typical for a photonic crystal is that electromagnetic waves in a certain frequency range and/or with a certain polarization cannot propagate along certain directions in the crystal. This forbidden frequency range is called a stopgap. If the propagation of the electromagnetic wave is forbidden for any crystalline direction and any polarization, for a certain frequency range, then this forbidden frequency range is called a photonic band gap. The photonic band gap in a photonic crystal is similar to the electronic band gap in a semiconductor. In a semiconductor the periodic arrangement of atoms in the crystal lattice causes a range of energies for which the electrons cannot propagate through the material. Analogous to semiconductor technology a photonic crystal could be used to produce integrated optical circuits, which would have a lot of interesting applications.

Photonic crystals show many intriguing optical phenomena such as negative refraction, superprism, ultrarefractive phenomena, focusing of light and the localization of light. This makes that electromagnetic wave propagation in photonic crystals is not always easy to understand. However, the idea of controlling light by means of photonic crystals has led to many proposals for novel devices such as optical switches, microlasers, solar cells, and so on, and has motivated many researchers to investigate a plethora of ideas. In this thesis we study various aspects of the electromagnetic wave propagation in two-dimensional photonic crystals, but we mainly focus on their ability to mimic some aspects of negative-index materials that is materials with simultaneously negative permeability and permittivity and thus a negative refractive index, and their ability to control the spontaneous emission of light.

The propagation of light in a photonic crystal is described by the time-dependent Maxwell equations. These equations can only be solved analytically for very simple cases. For most practical applications they are solved numerically. A method that is often used for this purpose is the finite-difference time-domain (FDTD) method, based on an algorithm due to K. S. Yee in 1966. In the FDTD technique the time-dependent Maxwell equations are solved

by propagating the electromagnetic fields in the time domain and by modeling the interaction of the electromagnetic fields with the dielectric medium. Apart from a discretization in time, the FDTD technique also requires a spatial discretization. The grid spacing must be sufficiently small to resolve both the smallest electromagnetic wavelength and the smallest geometrical feature in the model. Yee's method is fast, flexible and easy to implement but is conditionally stable, meaning that it is numerically stable if the time-step divided by the spatial mesh size is small enough. This puts limitations on the time-intervals that can be studied. Another drawback of the method is that it is not suitable to calculate spectra as the method does not conserve the energy of the electromagnetic field. To overcome both limitations, De Raedt and co-workers developed in 1999 a systematic approach to solve the time-dependent Maxwell equations with unconditionally stable numerical schemes based on the Lie-Trotter-Suzuki product-formulas. In this thesis we use this unconditionally stable numerical scheme to investigate the electromagnetic wave propagation in photonic crystals having translational invariance with respect to the z-direction.

In 1967, Veselago has shown theoretically that a flat plate of thickness D made from a negative-index material with a refractive index equal to -1 and situated in vacuum can focus electromagnetic waves from a point source P positioned at a distance $L < D$ from one side of the plate to a point P' located at a distance $D - L$ from the other side of the plate. Also inside the plate an image is formed. Due to the relation $L + L' = D$, the distance between P and P' is always equal to $2D$. Hence, to increase the distance between P and P' there are two possibilities: Increasing D or applying the principle of image transfer by a cascaded stack. In 2000, Pendry pointed out that these slabs make perfect lenses or superlenses, since both propagating and evanescent waves contribute to the resolution of the image. Because Pendry also demonstrated, by means of simulations, that such a lens with subwavelength resolution and operating at the frequency of visible light can be physically realized in the form of a thin slab of silver, a lot of research has been performed on negative-index materials and superlenses since 2000. In 2000, Notomi has shown theoretically that two-dimensional photonic crystals near the band gap frequency behave as if they have an effective refractive index. For some frequency regions this effective refractive index can be negative. As a result, in these frequency regions photonic crystals can exhibit similar phenomena as observed in negative-index materials, including negative refraction and imaging by a planar surface. Since 2003 various experiments have been performed that confirm this theoretical observation. The first theoretical demonstration of negative refraction and subwavelength imaging in three-dimensional photonic crystals was made in 2002. In 2005 such a three-dimensional photonic crystal was really produced and negative refraction and subwavelength imaging in the microwave regime was experimentally confirmed.

We have studied the possibility to observe negative refraction in triangular and square lattice photonic crystals and to focus light by means of thin slabs of these photonic crystals in great detail. We have shown that for some frequencies a photonic crystal slab consisting of a

dielectric medium with circular holes drilled in a triangular lattice configuration behaves in many respects as a slab made from a homogeneous effective medium with an effective refractive index of approximately -1 and thus operates as a negative-index lens. Since the refractive index slightly deviates from -1 for different angles of incidence, the image of a point source, formed behind the photonic crystal slab, is not circular but elongated in the direction of propagation. Hence, as opposed to the image formation with a flat negative index material lens with a refractive index equal to -1, the image formation is not perfect. The spatial resolution in the direction of propagation is larger than the wavelength λ of the electromagnetic wave, but the spatial resolution of the image in the direction perpendicular to the direction of propagation is smaller than $\lambda/2$. Hence, only in the direction perpendicular to the direction of electromagnetic wave propagation, a subwavelength resolution of the image can be achieved. Another important difference between the flat photonic crystal lens and the flat negative-index lens with a refractive index of -1 is that the photonic crystal lens causes an enormous loss in light intensity. Most of the light is reflected at the photonic crystal lens surface, while for the negative-index lens no reflection occurs. Despite of this, we have shown that image transfer by a cascaded stack consisting of two and three triangular lattice photonic crystal slabs separated by air layers, is feasible. Hence, this provides a method to increase the source-image distance. Namely, taking one photonic crystal slab and increasing its thickness is no option for this purpose, since it leads to worsening spatial resolutions of the image that is formed behind the slab. Although triangular lattice photonic crystals can be created that can be used to construct a flat lens acting in many respects as a flat negative-index lens, this is only for frequency ranges in the upper photonic bands. It has been suggested that for square lattice photonic crystals the same phenomena can be observed for frequencies in the lowest band, but we have shown that these square lattice photonic crystals cannot be used for the purpose of lensing.

In the last chapter of this thesis, we focused on another interesting optical property of photonic crystals, namely their ability to control the spontaneous emission of defects inside the photonic crystal. We discovered a simple, efficient procedure to compute the spontaneous emission rate from short-time FDTD data of the electromagnetic field energy. By using the unconditionally stable method to compute the emitted energy, we are guaranteed that, in the absence of external currents, the algorithm conserves the energy exactly. This ensures that the time-dependence of the emitted energy is due to the presence of the source only. We applied this procedure to two-dimensional photonic crystals, but the method applies to microcavities of arbitrary geometry. For comparison, we also calculated the local radiative density of states employing the unconditionally stable FDTD method that is without solving the eigenvalue problem and integrating over the (first) Brillouin zone. We demonstrated that both methods yield the same predictions about the enhancement or suppression of the spontaneous emission rate by photonic crystals. The spontaneous emission rate strongly depends on the location of the source in the photonic crystal and on the frequency of the emitted light. Emission en-

hancement as well as emission suppression can be observed. Even if the photonic crystal has no photonic band gap, the emission of a point source can be almost completely suppressed.

Samenvatting

Een fotonisch kristal is een composiet materiaal (meestal opgebouwd uit twee componenten, waarbij één van de twee componenten lucht is) met een periodisch variërende brekingsindex. De brekingsindex kan variëren in één, twee of drie kristalrichtingen. We spreken dan respectievelijk van een één-, twee- of driedimensionaal fotonisch kristal. Een fotonisch kristal wordt zo gemaakt dat de roosterafstand in de orde is van de golflengte van de elektromagnetische golf die men ermee wil controleren. Namelijk, typerend voor een fotonisch kristal is dat elektromagnetische golven binnen een bepaald frequentiebereik en/of met een bepaalde polarisatie zich niet kunnen voortplanten in bepaalde kristalrichtingen. Dit verboden frequentiegebied wordt een kloof genoemd. Indien de voortplanting van de elektromagnetische golf verboden is voor alle kristalrichtingen en voor elke polarisatie dan noemen we dit verboden frequentiegebied een fotonische bandkloof. De fotonische bandkloof in een fotonisch kristal vertoont een sterke analogie met de elektronische bandkloof in een halfgeleider. In een halfgeleider zorgt de periodische schikking van atomen in het kristalrooster ervoor dat elektronen met een bepaald energiebereik niet doorheen het materiaal kunnen bewegen. Er wordt verwacht dat, naar analogie met de halfgeleider technologie, fotonische kristallen gebruikt kunnen worden voor het maken van geïntegreerde optische schakelingen, wat vele interessante toepassingen met zich mee zou brengen.

Fotonische kristallen vertonen verschillende intrigerende optische verschijnselen zoals, negatieve breking, een uitzonderlijk grote hoekafhankelijke dispersie (“superprism”), het focusseren en het lokaliseren (opsluiten) van licht. Dit maakt dat de voortplanting van elektromagnetische golven in een fotonisch kristal niet altijd eenvoudig te begrijpen is. Toch heeft het idee dat licht kan gecontroleerd worden door middel van fotonische kristallen geleid tot verschillende voorstellen voor toepassingen zoals optische schakelaars, efficiënte miniatuurlasers, zonnecellen, enz. Bovendien hebben fotonische kristallen vele wetenschappers gemotiveerd om een veelheid aan ideeën te onderzoeken. In deze thesis bestuderen we verschillende aspecten van de voortplanting van elektromagnetische golven in tweedimensionale fotonische kristallen. We vestigen hierbij onze aandacht vooral op het feit dat sommige fotonische kristallen bepaalde eigenschappen van negatieve-index materialen, materialen waarvan de

permeabiliteit en de permittiviteit tegelijkertijd negatief zijn zodat de brekingsindex negatief is, kunnen nabootsen en op het feit dat ze de spontane emissie van licht kunnen controleren.

De voortplanting van licht in een fotonisch kristal wordt beschreven door de tijdsafhankelijke Maxwell vergelijkingen. Deze vergelijkingen kunnen enkel analytisch opgelost worden voor heel eenvoudige gevallen. Voor de meeste praktische toepassingen worden ze numeriek opgelost. Een methode die dikwijls voor dit doel aangewend wordt is de zogenaamde "finite-difference time-domain (FDTD)" methode, die gebaseerd is op een algoritme ontwikkeld door K.S. Yee in 1966. In de FDTD methode worden de tijdsafhankelijke Maxwell vergelijkingen opgelost door de elektromagnetische velden voor te planten in het tijdsdomein en door de interactie van deze velden met het diëlektrisch medium te modelleren. Behalve een discretisatie van de tijd, vereist de FDTD techniek ook een discretisatie van de ruimte. De roosterafstand moet voldoende klein zijn om zowel de kleinste elektromagnetische golflengte als de kleinste geometrische structuur in het model te kunnen onderscheiden. De methode ontwikkeld door Yee is snel, flexibel en gemakkelijk om te programmeren, maar enkel stabiel onder bepaalde voorwaarden. De methode is enkel numeriek stabiel als de tijdstap gedeeld door de roosterafstand voldoende klein is. Dit legt beperkingen op aan de tijdsintervallen die kunnen bestudeerd worden. Een ander nadeel van deze methode is dat ze niet kan gebruikt worden voor het berekenen van spectra, omdat ze de energie van het elektromagnetische veld niet behoudt. Om deze beperkingen te elimineren hebben De Raedt en medewerkers in 1999 een systematische techniek ontwikkeld om de tijdsafhankelijke Maxwell vergelijkingen op te lossen met behulp van onconditioneel stabiele numerieke schema's, gebaseerd op de Lie-Trotter-Suzuki produkt-formules. In deze thesis maken we gebruik van deze onconditioneel stabiele numerieke methode om de voorplanting van elektromagnetische golven te bestuderen in fotonische kristallen die translatie invariant zijn in de z-richting. De keuze voor fotonische kristallen met translatie invariantie in de z-richting herleidt het numerieke probleem van het oplossen van de tijdsafhankelijke Maxwell vergelijkingen tot een zuiver tweedimensionaal probleem. Dit heeft als voordeel dat we een redelijk grote parameterruimte kunnen onderzoeken. Driedimensionale FDTD berekeningen zijn namelijk erg rekenintensief.

In 1967 heeft Veselago theoretisch aangetoond dat een vlakke plaat, gemaakt van een negatief-index materiaal met een brekingsindex gelijk aan -1, met dikte D en geplaatst in vacuüm, een elektromagnetische golf, uitgezonden door een puntbron P geplaatst op een afstand $L < D$ van de linkerkant van de plaat, kan focusseren in een punt P' op een afstand $D - L$ van de rechterkant van de plaat. Ook binnenin de vlakke plaat wordt een beeld van de puntbron gevormd. Vanwege het verband $L + L' = D$, is de afstand tussen de punten P en P' altijd gelijk aan $2D$. Als we dus de afstand tussen de punten P en P', of anders gezegd de afstand tussen object en beeld willen vergroten, dan zijn er twee mogelijkheden: ofwel maken we de vlakke plaat dikker, ofwel maken we gebruik van het principe van beeldoverdracht door middel van een stapel bestaande uit verschillende vlakke platen gemaakt van een negatief-index materiaal afgewisseld met luchtlagen. In 2000 heeft Pendry aangetoond

dat deze vlakke platen perfecte lenzen of zogenaamde superlenzen vormen, omdat zowel de zich voortplantende golven als de 'evanescente' (verdampende) golven bijdragen aan de resolutie van het beeld. Pendry heeft ook, door middel van simulaties, aangetoond dat zo een lens met een resolutie kleiner dan de golflengte van zichtbaar licht kan gemaakt worden van een dunne zilverplaat. Dit heeft sinds 2000 geleid tot een enorme hoeveelheid wetenschappelijke studies aan negatieve index-materialen en superlenzen in het bijzonder. In 2000 heeft Notomi theoretisch aangetoond dat voor frequenties in de nabijheid van de fotonische bandkloof, tweedimensionale fotonische kristallen zich gedragen alsof ze een effectieve brekingsindex zouden hebben. Deze effectieve brekingsindex verschilt van het gewogen gemiddelde van de brekingsindices van de componenten van het composiet materiaal en is sterk frequentieafhankelijk. Deze effectieve brekingsindex kan zelfs negatief zijn voor bepaalde frequenties. Voor deze frequenties kan een tweedimensionaal fotonisch kristal gelijkaardige verschijnselen vertonen als waargenomen in negatieve-index materialen, inclusief negatieve breking en beeldvorming door middel van een vlakke plaat. Sinds 2003 hebben verschillende experimenten deze theoretische voorspelling bevestigd. In 2002 is er theoretisch aangetoond dat negatieve breking en beeldvorming met een resolutie kleiner dan de golflengte van de elektromagnetische golf ook in een driedimensionaal kristal kan gerealiseerd worden. In 2005 is zo een driedimensionaal fotonisch kristal dan ook daadwerkelijk gefabriceerd en is negatieve breking en beeldvorming met een resolutie kleiner dan de golflengte van de elektromagnetische golf experimenteel aangetoond voor microgolven.

We hebben de mogelijkheid onderzocht om in de eerste plaats negatieve breking waar te nemen in een fotonisch kristal met driehoekige en vierkante roosterstructuur en in de tweede plaats om licht te focusseren met behulp van dunne vlakke platen gemaakt van deze fotonische kristallen. We hebben aangetoond dat voor bepaalde frequenties een dunne plaat van een fotonisch kristal, gemaakt van een diëlektrisch materiaal waarin ronde gaten geboord zijn in een driehoekige roosterstructuur, zich in vele opzichten gedraagt zoals een dunne plaat gemaakt van een homogeen effectief medium met een effectieve brekingsindex die ongeveer gelijk is aan -1. Het fotonisch kristal opereert voor deze frequenties als het ware als een negatieve-index lens. Omdat de brekingsindex lichtjes verschilt van -1 voor verschillende invalshoeken, is het beeld van een puntbron dat gevormd wordt achter de fotonische kristalplaat, niet cirkelvormig, maar uitgerekt in de voortplantingsrichting van de elektromagnetische golf. In tegenstelling tot de beeldvorming met behulp van een vlakke negatieve-index lens met een brekingsindex gelijk aan -1, is de beeldvorming dus niet perfect. De ruimtelijke resolutie in de voortplantingsrichting is groter dan de golflengte λ van de elektromagnetische golf, maar de ruimtelijke resolutie van het beeld in de richting loodrecht op de voortplantingsrichting is kleiner dan $\lambda/2$. We kunnen dus enkel een resolutie kleiner dan de golflengte van de elektromagnetische golf bekomen in de richting loodrecht op de voortplantingsrichting van de elektromagnetische golf. Een ander belangrijk verschil tussen de vlakke fotonische kristal lens en de vlakke negatief-index lens met een brekingsindex gelijk aan -1, is dat een fotonisch

kristal een enorm verlies in lichtintensiteit veroorzaakt. Het grootste gedeelte van het licht wordt namelijk gereflecteerd aan het oppervlak van de fotonische kristal lens, terwijl voor de negatieve-index lens geen reflectie optreedt. Ondanks dit intensiteitverlies, hebben we toch kunnen aantonen dat beeldoverdracht door middel van stapels bestaande uit twee en drie vlakke platen gemaakt van een fotonisch kristal, afgewisseld met luchtlagen, verwezenlijkbaar is. Deze stapels leveren dus een mogelijkheid om de afstand tussen de bron en haar beeld te vergroten. Het beschouwen van één fotonische kristalplaat en het stelselmatig vergroten van haar dikte kan niet gebruikt worden voor dit doel, omdat dit leidt tot een slechtere resolutie van het beeld. Hoewel het dus mogelijk is om fotonische kristallen met een driehoekige roosterstructuur te maken die kunnen gebruikt worden voor het ontwerpen van een vlakke lens die zich in vele opzichten gedraagt zoals een negatieve-index lens, kan dit alleen maar voor frequenties in de hogere fotonisiche banden in het fotonisch bandenstructuur diagram. In de literatuur was gesuggereerd dat ook fotonische kristallen met een vierkante roosterstructuur voor dit doeleinde kunnen gebruikt worden, maar dan zelfs voor frequenties in de laagste band van het fotonisch bandenstructuur diagram. We hebben echter aangetoond dat fotonische kristallen met een vierkante roosterstructuur niet geschikt zijn voor het maken van een vlakke lens.

In het laatste hoofdstuk van deze thesis hebben we een andere interessante optische eigenschap van fotonische kristallen bestudeerd, namelijk hun potentie om de spontane emissie van defecten (atomen of moleculen), opgesloten in het kristal, te controleren. Een atoom dat terugvalt van de aangeslagen toestand naar de grondtoestand zendt spontaan licht uit in een willekeurige richting. De frequentie van het uitgezonden licht en de gemiddelde tijd tussen het aanslaan en het spontane verval naar de grondtoestand zijn eigen aan het atoom. Echter, wanneer een atoom binnenin een fotonisch kristal geplaatst wordt, dan kan de spontane emissie versterkt, verzwakt of zelfs helemaal verboden worden. We hebben een eenvoudige en efficiënte procedure ontdekt om het in het fotonisch kristal uitgestraalde vermogen te berekenen aan de hand van FDTD data (voor een klein tijdsinterval) voor de elektromagnetische energie. Het grote voordeel van het gebruik van de onconditioneel stabiele numerieke methode is dat deze, in de afwezigheid van externe elektrische en magnetische stromen, de energie exact bewaart. We zijn er dus van verzekerd dat de tijdsafhankelijkheid van de door de lichtbron uitgezonden energie enkel het gevolg is van de aanwezigheid van de lichtbron zelf. We hebben de methode toegepast op tweedimensionale fotonische kristallen, maar de methode kan toegepast worden voor willekeurige microcaviteiten. Ter vergelijking hebben we ook de lokale fotonische toestandsdichtheid uitgerekend. We hebben aangetoond dat beide methodes dezelfde voorspellingen geven voor het versterken of afzwakken van het uitgestraalde vermogen in het fotonisch kristal. Het uitgestraalde vermogen is sterk afhankelijk van de positie van de lichtbron in het fotonisch kristal en van de uitgezonden frequentie. Zelfs al heeft het fotonisch kristal geen fotonische bandkloof dan kan de straling van een lichtbron binnenin het fotonisch kristal toch bijna volledig onderdrukt worden.

Acknowledgments

In the last four years, many people contributed, either directly or indirectly, to the work resulting in the thesis. I would like to thank all my colleagues, friends and relatives for their invaluable contributions and support. Without these, it would have been impossible to finish the dissertation.

First, I thank my supervisor Hans De Raedt providing me a position to work in the computational physics group. Hans is always ready to give advice, to answer my questions and to help me make good program codes. I learned from him how to look at a problem from a different point of view and to solve a problem in an efficient way. He helped me, not only in my research project, but also in my daily living problems. I am fortunate and proud of having him as my promotor. Second, I would give special acknowledge to my co-promotor Kristel Michielsen who supervised my daily research work. I owe her a lot for her patience in discussing every detail of the research. Whenever I had some questions or some new results, she was always willing to give invaluable advice and insightful analysis. She also helped a lot in the writing of the dissertation.

It is a great pleasure to acknowledge the support from the members of the group. Thilo Figge helped in many means to clarify the research problem, gave advice for giving presentations and in programming, and even wrote some codes to solve specific problems. I thank Sebastiaan Kole for helping me with my codes and figures. I would like to thank Shenjun Yuan, Shuang Zhao, Aard Keimpema for their inspiring discussions and advice both in my research work and in my daily life.

I would like to give special thanks to the reading committee: Prof. De Hosson, Prof. Stavenga and Prof. Vos for their insightful comments and constructive advices to make the dissertation scientifically clearer and linguistically better.

I am grateful to Eliane Flück and Kobus Kuipers for the discussions about the experimental results and implications and advice to my work during FOM meetings. I thank Willem Vos, Ad Lagendijk, Femius Koenderink from the group of Complex Photonic System (COPS) for the discussions about the experiments and photonic crystals in general and the comments and advices on my project during the FOM meetings.

I am thankful to the secretaries of the institute, Ynske Joustra, Iris de Roo-Kwant and Annelies van Leeuwen for their kind help not only in administrative but also in daily issues.

I would like also to thank the stichting FOM for the financial support to accomplish the research project and to attend conferences, meetings and training programs. I also thank the Faculteit der Wiskunde en Natuurwetenschappen and the Materials Science Centre for the financial support to attend meetings and training courses.

Last, but not least, I thank my wife Bin Li for her continuous support and encouragement. Without her, it is not possible to be successful in my research and to have a pleasant life. I would like to thank my two daughters, Tina and Wendy, for bringing me so many memorable events and turning my life into such an enjoyable one. I also own a lot to my parents, mother-in-law and brothers for encouraging me to make progress in my work and offer invaluable support to my life.